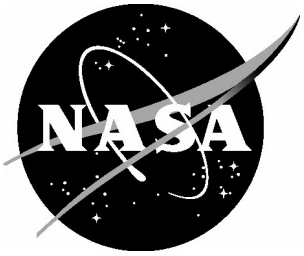
NASA/TP-20240006830



Experimental and Computational Study of Convective Heating on the Aeroshell Back Side and Payload of the LOFTID Vehicle

Brian R. Hollis, Elizabeth F. Rieken, Kyle B. Thompson and Adam J. Wise
Langley Research Center, Hampton, Virginia

Kevin E. Hollingsworth, Sheila A. Wright
Jacobs Technologies, Inc, Hampton, Virginia

November 2024

NASA STI Program Report Series

Since its founding, NASA has been dedicated to the advancement of aeronautics and space science. The NASA scientific and technical information (STI) program plays a key part in helping NASA maintain this important role.

The NASA STI program operates under the auspices of the Agency Chief Information Officer. It collects, organizes, provides for archiving, and disseminates NASA's STI. The NASA STI program provides access to the NTRS Registered and its public interface, the NASA Technical Reports Server, thus providing one of the largest collections of aeronautical and space science STI in the world. Results are published in both non-NASA channels and by NASA in the NASA STI Report Series, which includes the following report types:

- TECHNICAL PUBLICATION. Reports of completed research or a major significant phase of research that present the results of NASA Programs and include extensive data or theoretical analysis. Includes compilations of significant scientific and technical data and information deemed to be of continuing reference value. NASA counterpart of peer-reviewed formal professional papers but has less stringent limitations on manuscript length and extent of graphic presentations.

- TECHNICAL MEMORANDUM. Scientific and technical findings that are preliminary or of specialized interest, e.g., quick release reports, working papers, and bibliographies that contain minimal annotation. Does not contain extensive analysis.

- CONTRACTOR REPORT. Scientific and technical findings by NASA-sponsored contractors and grantees.

- CONFERENCE PUBLICATION. Collected papers from scientific and technical conferences, symposia, seminars, or other meetings sponsored or co-sponsored by NASA.

- SPECIAL PUBLICATION. Scientific, technical, or historical information from NASA programs, projects, and missions, often concerned with subjects having substantial public interest.

- TECHNICAL TRANSLATION. English-language translations of foreign scientific and technical material pertinent to NASA's mission.

Specialized services also include organizing and publishing research results, distributing specialized research announcements and feeds, providing information desk and personal search support, and enabling data exchange services.

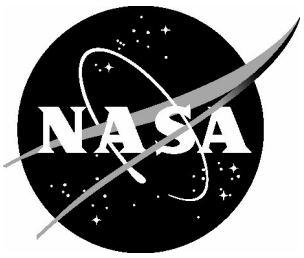
For more information about the NASA STI program, see the following:

- Access the NASA STI program home page at http://www.sti.nasa.gov

- Help desk contact information:

https://www.sti.nasa.gov/sti-contact-form/ and select the "General" help request.

NASA/TP-20240006830



Experimental and Computational Study of Convective Heating on the Aeroshell Back Side and Payload of the LOFTID Vehicle

Brian R. Hollis, Elizabeth F. Rieken, Kyle B. Thompson and Adam J. Wise
Langley Research Center, Hampton, Virginia

Kevin E. Hollingsworth
Jacobs Technologies, Inc, Hampton, Virginia

National Aeronautics and
Space Administration

Langley Research Center
Hampton, Virginia 23681-2199

November 2024

The use of trademarks or names of manufacturers in this report is for accurate reporting and does not constitute an official endorsement, either expressed or implied, of such products or manufacturers by the National Aeronautics and Space Administration.

Available from:

NASA STI Program / Mail Stop 148
NASA Langley Research Center
Hampton, VA 23681-2199
Fax: 757-864-6500

Table of Contents

Table of Contents i
List of Tables ii
Abstract 1
Symbols 2
Subscripts and Superscripts 2
Acronyms 2
Introduction 3
Background 3
Experimental Tools and Methods 4
Test Program Overview 4
Wind Tunnel Model Geometries and Fabrication 5
Wind Tunnel Test Conditions and Facility Details 5
Wind Tunnel Test Conditions 5
NASA LaRC 31-Inch Mach 10 Air Tunnel 6
NASA LaRC 20-Inch Mach 6 Air Tunnel 6
Experimental Data 7
Data Acquisition and Reduction 7
Data Mapping and Presentation 7
Heat Transfer Data Uncertainty 8
Computational Tools and Methods 9
Flow Field Solver 9
Grid Topology 9
Experimental and Computational Analyses 10
Aeroshell Front Side Heating Data 10
Aeroshell Back Side and Payload Heating Data 10
Reynolds Number Effects 11
Angle-of-Attack Effects 11
Flow Field Simulations and Comparisons with Data 12
Summary and Conclusions 13
Acknowledgments 14
References 15
Appendix A. Mach 10 Phosphor Thermography Global Heating Images 84
Appendix B. Mach 6 Phosphor Thermography Global Heating Images 95

List of Tables

Table 1. Averaged Nominal Conditions for 31-Inch Mach 10 Air Tunnel Test 539. 17
Table 2. 31-Inch Mach 10 Air Tunnel Test 539 Run Matrix. 17
Table 3. Averaged Nominal Conditions for 20-Inch Mach 6 Air Tunnel Test 7052. 18
Table 4. 20-Inch Mach 6 Air Tunnel Test 7052 Run Matrix. 18

List of Figures

Figure 1. Infrared image of LOFTID splashdown [Source NASA]. 19
Figure 2. Recovered LOFTID flight vehicle [Source NASA]. 19
Figure 3. LOFTID flight vehicle cross section and dimensions. 19
Figure 4. LOFTID exposed toroid back side geometry (T-1). 20
Figure 5. LOFTID smooth back side geometry (S-1). 21
Figure 6. Smooth and toroid model outer mold lines and dimensions. 22
Figure 7. Support hardware configuration for models T-1 and S-1. 23
Figure 8. Support hardware: blade details. 24
Figure 9. Support hardware: sting details. 25
Figure 10. Smooth model S-1 rear view photographs (source NASA). 26
Figure 11. Toroid model T-1 rear view photographs (source NASA). 26
Figure 12. Front view photographs of model A-0-S (source NASA). 26
Figure 13. Setup for model front view (not to scale). 27
Figure 14. Setup for model back view (not to scale). 27
Figure 15. Schematic of Langley Research Center 31-Inch Mach 10 Air Tunnel. 28
Figure 16. Schematic of Langley Research Center 20-Inch Mach 6 Air Tunnel. 28
Figure 17. Sample phosphor thermography 2-D image data. 29
Figure 18. Sample 3-D mapping of phosphor thermography data. 29
Figure 19. Averaging regions for $\alpha = 0$ deg, $\phi = 0$ deg side view in 31-Inch Mach 10 Air Tunnel. 30
Figure 20. Averaging regions for $\alpha = 0$ deg, $\phi = 90$ deg side view in 31-Inch Mach 10 Air Tunnel. 30
Figure 21. Averaging regions for $\alpha = \pm 5$ deg , $\phi = 0$ deg side view in 31-Inch Mach 10 Air Tunnel. 30
Figure 22. Averaging regions for $\alpha = 0$ deg , $\phi = 0$ deg top view in 20-Inch Mach 6 Air Tunnel. 31
Figure 23. Illustration of locations for extraction of data rays. 32
Figure 24. Stacked-block grid topology block types. 33
Figure 25. Stacked-block grid topology for LOFTID at wind tunnel conditions. 33
Figure 26. Aeroshell model A-0-S heating images at Mach 10, $\alpha = 0$-deg. 34
Figure 27. Aeroshell model A-0-S heating line plot at Mach 10, $\alpha = 0$-deg. 34
Figure 28. Aeroshell model A-0-S heating images at Mach 6, $\alpha = 0$-deg. 35
Figure 29. Aeroshell model A-0-S heating line plot at Mach 6, $\alpha = 0$-deg. 35
Figure 30. Smooth model S-1 back side images at Mach 10, $\alpha = -5$ deg , $\phi = 0$ deg. 36
Figure 31. Smooth model S-1 back side plots at Mach 10, $\alpha = -5$ deg , $\phi = 0$ deg. 37
Figure 32. Smooth model S-1 back side images at Mach 10, $\alpha = 0$ deg , $\phi = 0$ deg. 38
Figure 33. Smooth model S-1 back side plots at Mach 10, $\alpha = 0$ deg , $\phi = 0$ deg. 39
Figure 34. Smooth model S-1 back side images at Mach 10, $\alpha = 0$ deg , $\phi = 90$ deg. 40
Figure 35. Smooth model S-1 back side plots at Mach 10, $\alpha = 0$ deg , $\phi = 90$ deg. 41
Figure 36. Smooth model S-1 back side images at Mach 10, $\alpha = +5$ deg , $\phi = 0$ deg. 42
Figure 37. Smooth model S-1 back side plots at Mach 10, $\alpha = 5$ deg , $\phi = 0$ deg. 43
Figure 38. Toroid model T-1 back side images at Mach 10, $\alpha = -5$ deg , $\phi = 0$ deg. 44
Figure 39. Toroid model T-1 back side plots at Mach 10, $\alpha = 5$ deg , $\phi = 0$ deg. 45
Figure 40. Toroid model T-1 back side images at Mach 10, $\alpha = 0$ deg , $\phi = 0$ deg. 46
Figure 41. Toroid model T-1 back side plots at Mach 10, $\alpha = 0$ deg , $\phi = 0$ deg. 47
Figure 42. Toroid model T-1 back side images at Mach 10, $\alpha = 0$ deg , $\phi = 90$ deg. 48
Figure 43. Toroid mode T-1 back side plots at Mach 10, $\alpha = 0$ deg , $\phi = 90$ deg. 49
Figure 44. Toroid model T-1 back side images at Mach 10, $\alpha = +5$ deg , $\phi = 0$ deg. 50
Figure 45. Toroid model T-1 back side plots at Mach 10, $\alpha = +5$ deg , $\phi = 0$ deg. 51
Figure 46. Smooth model S-1 back side images at Mach 6, $\alpha = 0$ deg , $\phi = 0$ deg. 52
Figure 47. Smooth model S-1 back side plots at Mach 6, $\alpha = 0$ deg , $\phi = 0$ deg. 53
Figure 48. Smooth model S-1: Reynolds number effects at Mach 10, $\alpha = -5$ deg, $\phi = 0$ deg. 54

Figure 49. Smooth model S-1: Re_∞ effects at Mach 10, α = 0 deg, ϕ = 0 deg. 55
Figure 50. Smooth model S-1: Re_∞ effects at Mach 10, α = 0 deg, ϕ = 0 deg. 56
Figure 51. Smooth model S-1: Re_∞ effects at Mach 10, α = +5 deg, ϕ = 0 deg. 57
Figure 52. Toroid model T-1: Re_∞ effects at Mach 10, α = -5 deg, ϕ = 0 deg. 58
Figure 53. Toroid model T-1: Re_∞ effects at Mach 10, α = 0 deg, ϕ = 0 deg. 59
Figure 54. Toroid model T-1: Re_∞ effects at Mach 10, α = 0 deg, ϕ = 90 deg. 60
Figure 55. Toroid model T-1: Re_∞ effects at Mach 10, α = +5 deg, ϕ = 0 deg. 61
Figure 56. Smooth model S-1: Re_∞ effects at Mach 6, α = 0 deg, ϕ = 0 deg. 62
Figure 57. Smooth model S-1: α sweep at Mach 10, $Re_\infty = 0.5\times10^6$/ft, ϕ = 0 deg. 63
Figure 58. Smooth model S-1: α sweep at Mach 10, $Re_\infty = 1.0\times10^6$/ft, ϕ = 0 deg. 64
Figure 59. Smooth model S-1: α sweep at Mach 10, $Re_\infty = 1.9\times10^6$/ft, ϕ = 0 deg. 65
Figure 60. Toroid model T-1: α sweep at Mach 10, $Re_\infty = 0.5\times10^6$/ft, ϕ = 0 deg. 66
Figure 61. Toroid model T-1: α sweep at Mach 10, $Re_\infty = 1.0\times10^6$/ft, ϕ = 0 deg. 67
Figure 62. Toroid model T-1: α sweep at Mach 10, $Re_\infty = 1.9\times10^6$/ft, ϕ = 0 deg. 68
Figure 63. Predicted flow field properties: total energy at Mach 10. 69
Figure 64. Predicted flow field properties: pressure at Mach 10. 70
Figure 65. Predicted flow field properties: temperature at Mach 10. 71
Figure 66. Predicted flow field properties: *x*-component of velocity at Mach 10. 72
Figure 67. Predicted flow field properties: total velocity at Mach 10. 73
Figure 68. Predicted flow field properties: total energy at Mach 6. 74
Figure 69. Predicted flow field properties: pressure at Mach 6. 75
Figure 70. Predicted flow field properties: temperature at Mach 6. 76
Figure 71. Predicted flow field properties: *x*-component of velocity at Mach 6. 77
Figure 72. Predicted flow field properties: total velocity at Mach 6. 78
Figure 73. Aeroshell front heating comparison, LAURA vs. Mach 10 data. 79
Figure 74. Aeroshell front heating comparison, LAURA vs. Mach 6 data. 79
Figure 75. Smooth model back side and payload comparisons with LAURA vs. Mach 10 data. 80
Figure 76. Toroid model back side and payload comparisons with LAURA vs. Mach 10 data. 81
Figure 77. Smooth model back side and payload comparisons with LAURA vs. Mach 6 data. 82
Figure 78. Smooth model backside and payload comparisons with LAURA vs. Mach 6 data. 83
Figure 79. Test 539, Run 04, $Re_\infty = 0.5\times10^6$/ft, α = 0 deg, ϕ = 0 deg. 85
Figure 80. Test 539, Run 02, $Re_\infty = 1.0\times10^6$/ft, α = 0 deg, ϕ = 0 deg. 85
Figure 81. Test 539, Run 05, $Re_\infty = 1.9\times10^6$/ft, α = 0 deg, ϕ = 0 deg. 85
Figure 82. Test 539, Run 07, $Re_\infty = 0.5\times10^6$/ft, α = 0 deg, ϕ = 30 deg. 86
Figure 83. Test 539, Run 08, $Re_\infty = 1.0\times10^6$/ft, α = 0 deg, ϕ = 30 deg. 86
Figure 84. Test 539, Run 10, $Re_\infty = 1.9\times10^6$/ft, α = 0 deg, ϕ = 30 deg. 86
Figure 85. Test 539, Run 15, $Re_\infty = 0.5\times10^6$/ft, α = -5 deg, ϕ = 0 deg. 87
Figure 86. Test 539, Run 16, $Re_\infty = 1.0\times10^6$/ft, α = -5 deg, ϕ = 0 deg. 87
Figure 87. Test 539, Run 18, $Re_\infty = 1.9\times10^6$/ft, α = -5 deg, ϕ = 0 deg. 87
Figure 88. Test 539, Run 13, $Re_\infty = 0.5\times10^6$/ft, α = 0 deg, ϕ = 0 deg. 88
Figure 89. Test 539, Run 12, $Re_\infty = 1.0\times10^6$/ft, α = 0 deg, ϕ = 0 deg. 88
Figure 90. Test 539, Run 14, $Re_\infty = 1.9\times10^6$/ft, α = 0 deg, ϕ = 0 deg. 88
Figure 91. Test 539, Run 33, $Re_\infty = 1.0\times10^6$/ft, α = 0 deg, ϕ = 90 deg. 89
Figure 92. Test 539, Run 34, $Re_\infty = 1.9\times10^6$/ft, α = 0 deg, ϕ = 90 deg. 89
Figure 93. Test 539, Run 20, $Re_\infty = 0.5\times10^6$/ft, α = +5 deg, ϕ = 0 deg. 90
Figure 94. Test 539, Run 21, $Re_\infty = 1.0\times10^6$/ft, α = +5 deg, ϕ = 0 deg. 90
Figure 95. Test 539, Run 19, $Re_\infty = 1.9\times10^6$/ft, α = +5 deg, ϕ = 0 deg. 90
Figure 96. Test 539, Run 31, $Re_\infty = 0.5\times10^6$/ft, α = -5 deg, ϕ = 0 deg. 91
Figure 97. Test 539, Run 32, $Re_\infty = 1.0\times10^6$/ft, α = -5 deg, ϕ = 0 deg. 91
Figure 98. Test 539, Run 30, $Re_\infty = 1.9\times10^6$/ft, α = -5 deg, ϕ = 0 deg. 91
Figure 99. Test 539, Run 25, $Re_\infty = 0.5\times10^6$/ft, α = 0 deg, ϕ = 0 deg. 92

Figure 100. Test 539, Run 26, $Re_\infty = 1.0\times10^6$/ft, $\alpha = 0$ deg, $\phi = 0$ deg. 92
Figure 101. Test 539, Run 24, $Re_\infty = 1.9\times10^6$/ft, $\alpha = 0$ deg, $\phi = 0$ deg. 92
Figure 102. Test 539, Run 36, $Re_\infty = 0.5\times10^6$/ft, $\alpha = 0$ deg, $\phi = 90$ deg. 93
Figure 103. Test 539, Run 35, $Re_\infty = 1.0\times10^6$/ft, $\alpha = 0$ deg, $\phi = 90$ deg. 93
Figure 104. Test 539, Run 37, $Re_\infty = 1.9\times10^6$/ft, $\alpha = 0$ deg, $\phi = 90$ deg. 93
Figure 105. Test 539, Run 27, $Re_\infty = 0.5\times10^6$/ft, $\alpha = +5$ deg, $\phi = 0$ deg. 94
Figure 106. Test 539, Run 28, $Re_\infty = 1.0\times10^6$/ft, $\alpha = +5$ deg, $\phi = 0$ deg. 94
Figure 107. Test 539, Run 29, $Re_\infty = 1.9\times10^6$/ft, $\alpha = +5$ deg, $\phi = 0$ deg. 94
Figure 108. Test 7052, Run 105, $Re_\infty = 1.1\times10^6$/ft, $\alpha = 0$ deg, $\phi = 0$ deg. 96
Figure 109. Test 7052, Run 106, $Re_\infty = 2.1\times10^6$/ft, $\alpha = 0$ deg, $\phi = 0$ deg. 96
Figure 110. Test 7052, Run 107, $Re_\infty = 3.0\times10^6$/ft, $\alpha = 0$ deg, $\phi = 0$ deg. 96
Figure 111. Test 7052, Run 100, $Re_\infty = 1.1\times10^6$/ft, $\alpha = 0$ deg, $\phi = 0$ deg. 97
Figure 112. Test 7052, Run 98, $Re_\infty = 2.0\times10^6$/ft, $\alpha = 0$ deg, $\phi = 0$ deg. 97
Figure 113. Test 7052, Run 97, $Re_\infty = 3.0\times10^6$/ft, $\alpha = 0$ deg, $\phi = 0$ deg. 97
Figure 114. Test 7052, Run 101, $Re_\infty = 3.0\times10^6$/ft, $\alpha = 0$ deg, $\phi = 0$ deg. 98
Figure 115. Test 7052, Run 99, $Re_\infty = 4.0\times10^6$/ft, $\alpha = 0$ deg, $\phi = 0$ deg. 98
Figure 116. Test 7052, Run 102, $Re_\infty = 4.0\times10^6$/ft, $\alpha = 0$ deg, $\phi = 0$ deg. 98
Figure 117. Test 7052, Run 103, $Re_\infty = 3.0\times10^6$/ft, $\alpha = 0$ deg, $\phi = 0$ deg. 99
Figure 118. Test 7052, Run 104, $Re_\infty = 4.0\times10^6$/ft, $\alpha = 0$ deg, $\phi = 0$ deg. 99

Abstract

A wind tunnel test program was conducted to obtain experimental convective heating data on models of the the Low Earth Orbital Flight Test of an Inflatable Decelerator (LOFTID) vehicle in support of the flight test program. Wind tunnel testing was conducted at Mach 6 and Mach 10 at unit Reynolds numbers from 0.5×10^6/ft to 4.0×10^6/ft on 6.0 inch diameter aeroshell models. Global heating data were obtained through phosphor thermography measurements on the front and back of the aeroshell and on the payload. For all test conditions, attached, laminar flow was definitively produced on the front of the aeroshell, while in the wake the flow was separated, unsteady and possibly transitional or turbulent. A complementary computational study was performed to assess the accuracy of heating predictions for LOFTID wake flow environments. A new grid topology was developed for the study to allow the use of structured grid solvers for complex, open-backed geometries such as that of LOFTID. Close agreement between measurements and predictions was obtained on the front of the aeroshell. Comparisons were more challenging in the wake because of both the extremely low heating rates and the accompanying high uncertainties and the unsteady nature of the separated wake flow simulations. While the differences between heating predictions and measurements for the wake flow were higher than for the forebody flow, these differences were used to assist in the definition of conservative uncertainty margins for predictions of the flight environments for the successful flight test of the LOFTID vehicle in November 2022.

Symbols

E	total flow field energy
H_0	wind tunnel total (reservoir) enthalpy
H_{AW}	adiabatic wall enthalpy
H_W	wall enthalpy
H_{300K}	wall enthalpy at 300 K
h	measured heat-transfer film coefficient
h_{FR}	Fay-Riddell theory heat-transfer film coefficient
i, j, k	computational domain indices
M_∞	free stream Mach number
p	pressure
q	heat transfer rate
Re_θ	boundary-layer momentum thickness Reynolds number
Re_∞	free stream unit Reynolds number
T_∞	free stream temperature
u, v, w	velocity vector components
U_{total}	flow field total velocity
U_∞	free stream total velocity
x, y, z	Cartesian coordinates
α	angle of attack
ϕ	roll angle
ρ_∞	free stream density
σ	standard deviation
θ	boundary-layer momentum thickness

Subscripts and Superscripts

∞	wind tunnel free stream condition
0	wind tunnel stagnation condition
AW	adiabatic condition
TOT	wind tunnel reservoir condition
W	model wall condition

Acronyms

FTPS	Flexible Thermal Protection System
HIAD	Hypersonic Inflatable Aerodynamic Decelerator
IHEAT	Imaging for Hypersonic Experimental Aeroheating Testing
IRVE	Inflatable Reentry Vehicle Experiment
LAL	Langley Aerothermodynamics Laboratory
LaRC	Langley Research Center
LAURA	Langley Aerothermodynamic Upwind Relaxation Algorithm
LOFTID	Low-earth Orbit Flight Test of an Inflatable Decelerator
THOR	Terrestrial HIAD Orbital Reentry

Introduction

This report documents a hypersonic wind tunnel test program conducted to obtain aeroheating data on the back side of the Low-earth Orbit Flight Test of an Inflatable Decelerator (LOFTID) vehicle aeroshell and on its centerbody payload using global phosphor thermography. Although aeroheating rates in the wake (i.e., on the payload and the back of the aeroshell) of a blunt body geometry such as LOFTID are typically an order-of-magnitude less than that of the forebody, these low levels are still important to the design of an inflatable decelerator because its back side has no thermal protection, leaving the structural toroids exposed directly to the wake flow.

Supporting computational fluid dynamics flow field simulations were performed at the wind tunnel test conditions. Comparisons of the data from the wind tunnel tests were made with surface heating distributions from the flow field simulations to assess the accuracy of the computational methods.

These wind tunnel tests and computational simulations supported the definition of aeroheating environments and vehicle structure thermal response for the flight test of the LOFTID vehicle [1-2]. This technology demonstration mission was conducted in November of 2022 and successfully met all performance requirements. The vehicle splashed down in the Pacific Ocean (Figure 1), was recovered intact, re-inflated and put on display (Figure 2) at the Langley Research Center.

Background

The LOFTID vehicle is a member of the class of entry systems known as Hypersonic Inflatable Aerodynamic Decelerators, or HIADs. A HIAD consists of multiple heavy-duty, inflatable toroids that are held together by tension tie straps and covered with flexible thermal protection system (FTPS) material. The un-inflated HIAD is packaged in a small payload module for launch. Before atmospheric entry, the HIAD is deployed and inflated to form a large blunt-body aeroshell geometry. The LOFTID system (Figure 3) was comprised of six large toroids and one small toroid that were packaged in a 1.3 m diameter cylindrical payload canister. When deployed and inflated, the toroids and FTPS formed a 6 m diameter, 70-deg sphere-cone geometry.

Hypersonic Inflatable Aerodynamic Decelerator (HIAD) technology [3] offers an effective, mass-saving alternative to the conventional aerodynamic decelerators used in previous entry, descent, and landing systems such as the Orion crew capsule or the Mars Science Laboratory / Mars 2020 aeroshells. A HIAD has a lower mass and a smaller volume when packaged and stowed relative to a rigid aeroshell. But when deployed and inflated, it provides a large surface area for drag production, resulting in a lower ballistic coefficient than a rigid aeroshell of equivalent surface area would. The lower ballistic coefficient of the HIAD results in a less stressful trajectory with lower heat fluxes and integrated heat loads, thus reducing the performance demands on the aeroshell flexible thermal protection system (FTPS). For these reasons, HIAD systems are leading candidates for crew and cargo missions to Mars [4–6] that will require the delivery of landed masses up to a factor of 10 greater than has been possible using the rigid aeroshell technology of previous missions. HIAD systems are also under consideration for the return of payloads from Low Earth Orbit (LEO) or for the recovery and reuse of launch vehicle components [7]. NASA has committed to a program of development and demonstration flights to mature and validate HIAD technology for eventual use in operations missions.

The first phase of this development program was the Inflatable Reentry Vehicle Experiment (IRVE) series of flight tests launched on sounding rockets from the NASA Wallops Flight Facility. The first IRVE mission [8–10] suffered a launch system failure that was not related to the HIAD payload. A duplicate of

the IRVE vehicle was built and in 2009 the IRVE-II [11–13] flight demonstrated exoatmospheric inflation of the aeroshell and aerodynamic stability at hypersonic conditions. Because the IRVE-II vehicle was launched from a small, two-stage Black Brant IX sounding rocket, the aerothermal environment was quite benign: the maximum flight Mach number was 6.2, which produced peak heating rates of only ~2 W/cm^2. Nevertheless, the success of the IRVE-II mission provided the foundation for the next step in HIAD technology development, the IRVE-3 mission.

The IRVE-3 flight test [14–15] was a direct follow-on to IRVE-II, with the overall goal of demonstrating HIAD performance and gathering flight data in a operational-mission relevant environment. The primary mission objective for IRVE-3 was to demonstrate FTPS survivability during the hypersonic segment of the flight at heating levels an order-of-magnitude higher than IRVE-II. A secondary mission goal was to demonstrate the performance of an active center-of-gravity system during the subsonic portion of the trajectory. Key upgrades for the IRVE-3 mission included: launch aboard a three-stage sounding rocket to reach a peak Mach number of ~10 (as compared to Mach ~ 6 for IRVE-II); a larger entry vehicle mass (2 × greater than IRVE-II); a flight-relevant FTPS design; an attitude control system to maintain vehicle orientation; and an extensive instrumentation suite, including heat-flux and pressure gauges on the solid nose and in-depth thermocouples at multiple locations on the inflatable aeroshell. The IRVE-3 mission flew successfully in 2012, reaching a peak Mach number of 10 and demonstrating FTPS performance and survivability at a heating rate of ~ 20 W/cm^2.

After the successful IRVE series of suborbital, sounding rocket demonstration flights, the next step in NASA development of HIAD technology was a mission-scale demonstration launched from a heavy-lift vehicle to reach orbital velocity, the Low-earth Orbit Flight Test of an Inflatable Decelerator (LOFTID). In November of 2022, the LOFTID vehicle [16-18] was carried aboard an Atlas V rocket as a secondary payload on the Joint Polar Satellite System-2 (JPSS-2) mission. After deployment from the rocket, the heat shield inflated and LOFTID reentered the atmosphere at a velocity of ~8 km/sec, reaching peak heating levels of ~40 W/cm^2 at Mach 25. The mission successfully demonstrated the aerodynamic, aeroheating, thermal, and structural performance of a large HIAD at conditions relevant to a heavy down-mass operational mission at Earth or Mars.

Experimental Tools and Methods

Test Program Overview

A wind tunnel test program was performed to obtain aeroheating data on the LOFTID vehicle. These data were used to help define aeroshell back side and payload heating levels as well as for comparisons with wake flow simulations to assess the uncertainty of the computational tools and methods. Also, additional data (to be reported separately) were obtained on the effects of FTPS deformation under aerodynamic loading on aeroshell boundary-layer transition and turbulent heating augmentation. Two wind tunnel tests were conducted in the facilities of the Langley Aerothermodynamics Laboratory (LAL) to obtain these data: Test 539 in the NASA LaRC 31-Inch Mach 10 Air Tunnel and Test 7052 in the LaRC 20-Inch Mach 6 Air Tunnel. These tunnels are described in brief below and more detailed information can be found in [19].

The focus of Test 539 was on gathering aeroheating data on the aeroshell back side and payload. The higher stagnation enthalpy of the 31-Inch Mach 10 Air Tunnel produces greater (relative to 20-Inch Mach 6 Air Tunnel conditions) surface temperature rise on the wind tunnel models and more favorable signal-to-noise ratios for measurement of the low heating levels produced in the wake of a blunt body. The methodology and results from this test were similar to those from a previous test [20] of a similar HIAD

for the proposed Terrestrial HIAD Orbital Reentry (THOR) program, which was cancelled due to schedule and cost issues with the launch vehicle.

The focus of Test 7052 was on boundary-layer transition measurements on the front of the aeroshell, for which the wider Reynolds number operating range of the 20-Inch Mach 6 Air Tunnel (relative to that of the 31-Inch Mach 10 Air Tunnel) was more beneficial. During that test, a small number of runs were also conducted to obtain aeroshell back side and payload data, which are reported herein.

Wind Tunnel Model Geometries and Fabrication

Two geometries were employed in this test program: a scaled reproduction of the LOFTID geometry (denoted as T-1); and a simplified version of LOFTID with the exposed backs of the toroids covered with a flat surface (denoted as S-1). CAD renderings of these geometries are shown in Figure 4 and Figure 5 and cross sections of the outer mold lines with wind tunnel model scale dimensions are shown in Figure 6. While the exposed toroid geometry is directly relevant to the flight configuration, its complex topology presents numerical grid generation challenges, and the surface peaks-and-valleys defined by the toroids creates a complicated flow field for computational simulations. Thus, the simpler, smooth-backface model was included to provide a more amenable geometry for computational validation exercises.

Cast ceramic wind tunnel models of these two geometries were fabricated and a phosphor coating was applied for use in global optical thermography measurements of surface heating distributions. The fabrication process for a ceramic model is fully documented in [21] and summarized here. The first step in fabrication of models was the production of rapid prototype patterns of the geometries using a three-dimensional wax printer. The patterns were then hand-worked (where necessary) to remove any printing artifacts and leave a smooth surface finish. Multiple-piece injection molds were then built around the wax patterns and silica ceramic shell models were slip-cast in the molds. Then, the ceramic models were removed from the molds, dried, sintered, backfilled and mounted on support stings. Finally, the models were coated with a mixture of phosphors that luminesce under ultraviolet lighting to enable global phosphor thermography measurements.

For installation in the wind tunnel, the T-1 and S-1 models were mounted on the offset-blade sting configuration shown in Figure 7 to minimize the support hardware effects on the flow field. Dimensions of this support hardware are shown in Figure 8 and Figure 9. The long offset-blade sting allowed these models to be positioned toward the forward edge of the test section so that the model region of interest – the back of the aeroshell – was within the camera field of view. Photographs of these two models installed in the LaRC 31-Inch Mach10 Air Tunnel are shown in Figure 10 and Figure 11. An additional flat back model, denoted as A-0-S, was mounted on short cylindrical sting to permit viewing of the front of the aeroshell. Photographs of this model are shown in Figure 12. Illustrations of the relative differences in model and camera positioning to obtain front and back views of the aeroshell are provided in Figure 13 and Figure 14.

Wind Tunnel Test Conditions and Facility Details

Wind Tunnel Test Conditions

Data were obtained in Test 539 in the 31-Inch Mach 10 Air Tunnel at three unit-Reynolds numbers from $Re_\infty = 0.5\times10^6$/ft to 1.9×10^6/ft. Both back side geometries T-1 and S-1 were tested at $\alpha = 0$ deg for all Reynolds numbers, while a limited set of $\alpha = \pm5$ deg runs were performed at selected Reynolds numbers. Roll angles of $\phi = 0$ deg and 90 deg were set in the Mach 10 test to provide views with the mounting blade

blocking the line of sight to different portions of the back of the aeroshell. Due to schedule and resource limitations, it was not possible to obtain data at all angles of attack for every unit Reynolds number condition. Nominal, run-averaged conditions for Test 539 are listed in Table 1 and the full run matrix is detailed in Table 2. Entries in Table 2 are sorted first by model geometry, then by angle of attack, then by Reynolds number.

Data also were obtained in Test 7052 in the 20-Inch Mach 6 Air Tunnel at four unit-Reynolds numbers from $Re_\infty = 1.1\times10^6$/ft to 4.0×10^6/ft. Both back side geometries T-1 and S-1 were tested at $\alpha = 0$ deg, but not all Reynolds numbers were covered due to schedule limitations. Nominal, run-averaged conditions for Test 7052 are listed in Table 3 and the full run matrix is detailed in Table 4. Entries in Table 4 are sorted first by model geometry and then by Reynolds number.

A caveat to the inclusion of this Mach 6 data is required. The purpose of Test 7052 was to obtain data on the effects of flexible thermal protection system deflections on forebody aeroheating environments that are to be documented in a subsequent report. Approximately 100 runs were performed to generate that database using a different set of wind tunnel models. At the end of that activity, a few hours of facility time were still available and so the models used in the Test 539 entry in the 31-Inch Mach 10 Air Tunnel were run in the 20-Inch Mach 6 Air Tunnel to collect a limited heating data set on the back of the aeroshell and payload at Mach 6. However, the phosphor coating on these models had been visibly degraded by prior testing and lengthy storage. As such, the phosphor response was questionable and the resulting Mach 6 data set should be considered as qualitative, rather than quantitative.

In all these tables, free stream velocity (U_∞), density (ρ_∞), temperature (T_∞), unit Reynolds number (Re_∞), and Mach number (M_∞) are provided. Additionally, the enthalpy difference (ΔH_{tot}), and reference heat transfer film-coefficient value (h_{FR}) are given. The enthalpy term is defined as the difference $H_0 - H_{300K}$ between the free stream total enthalpy and the wall enthalpy at cold wall (300 K) conditions. The film coefficient is the value from the Fay-Riddell theory [22] at cold wall conditions, where the radius is the nose radius of the model geometry. Note that the nominal conditions listed in Table 1and Table 3 are based on averages of all runs at a given condition. As the run-to-run variations in test conditions were very slight (~1%), all supporting analyses (including computational simulations detailed below) were performed using these nominal values.

NASA LaRC 31-Inch Mach 10 Air Tunnel

The NASA LaRC 31-Inch Mach 10 Air Tunnel (Figure 15) is a perfect-gas, blow-down facility in which dried, filtered air is used as the working fluid. The tunnel has been calibrated for reservoir conditions varying from 150 psi to 1450 psi at an operating temperature of 1850°R, which produces free stream unit Reynolds numbers from 0.25×10^6/ft to 2.2×10^6/ft. The nozzle is water-cooled, has a three-dimensional contour, and ends with a 1.07×1.07 in. square throat. The 31×31 in. square test section features optical access through side, top, and bottom windows for visual imaging techniques and has a side-mounted injection system with a ±45 deg pitch range and ±5 deg yaw range. The test core varies from approximately 12×12 in. at the lowest unit Reynolds number to 14×14 in. at the highest unit Reynolds number. This tunnel has the highest Mach number of the LAL facilities and is mainly employed in aerodynamic and fluid-mechanics studies. The high stagnation temperature of the facility also makes it more suitable for aftbody/wake heating studies where the temperature rise is much lower than on the forebody.

NASA LaRC 20-Inch Mach 6 Air Tunnel

The NASA LaRC 20-Inch Mach 6 Air Tunnel (Figure 16) is a blow-down facility in which heated,

dried, and filtered air is used as the test gas. The tunnel has a two-dimensional contoured nozzle that opens into a 20.5 in. × 20.0 in. test section. The tunnel is equipped with a bottom-mounted injection system with a -5-deg to +55-deg pitch range and ±5-deg yaw range that can transfer a model from a sheltered model box to the tunnel centerline in less than 0.5 sec. Run times of up to 15 minutes are possible in this facility, although for aeroheating studies, run times of only a few seconds are typically required. The nominal reservoir conditions of this facility produce perfect-gas free stream flows with Mach numbers between 5.8 and 6.1 and unit Reynolds numbers of 0.5×10^6/ft to 8.3×10^6/ft. With its wide Reynolds number operating range capable of producing laminar, transitional, or turbulent flow on most geometries, this tunnel is primarily used for heat-transfer and boundary-layer transition studies.

Experimental Data

Data Acquisition and Reduction

Aeroheating data were obtained using the two-color, relative-intensity, global phosphor thermography method [23-24] and reduced using the Imaging for Hypersonic Experimental Aeroheating Testing (IHEAT) code [25]. In this method, a model is illuminated by ultraviolet light sources that induce temperature-dependent fluorescence of the phosphor coating during a run. Fluorescent intensity images of a model are taken in the tunnel before and during a run using a three-color, charge-coupled device camera. The intensity data are then converted to temperatures using pretest calibrations of the data acquisition system. Finally, heat-transfer film coefficients are determined by assuming a step function form for the convective film coefficient change from the prerun temperature to the run temperature, which corresponds to a parabolic temperature-time history. The heating data are typically reported in terms of the ratio h/h_{FR} where the heat-transfer film coefficient, h, is defined in terms of enthalpy via Eq. (1) as:

$$\boldsymbol{h = q/\Delta H_{TOT} = q/(H_{AW} - H_w) \cong q/(H_0 - H_w)} \tag{1}$$

In the calculation of the heat-transfer film coefficient, it is assumed that for a blunt-body, the adiabatic wall enthalpy H_{AW} is equal to the free stream total enthalpy of the tunnel, H_0. This heat transfer coefficient definition provides a theoretically near-constant value over the course of a run since the decrease in time of the heat transfer rate in the numerator as the model surface becomes hotter is balanced by the decrease of the enthalpy-difference term in the denominator. Additionally, the ratio h/h_{FR} is invariant with Reynolds number for laminar, perfect-gas flow such as produced in the LAL wind tunnels.

Data Mapping and Presentation

The two-dimensional (2-D) image data output from IHEAT (see example in Figure 17) were transformed to account for optical perspective effects and mapped to a three-dimensional (3-D) CAD representation of the wind tunnel model (see example in Figure 18). To accomplish this mapping, perspective, translational, and rotational transformations are first performed on the 3-D CAD surface until its 2-D projection matches that of the 2-D image data. The image data are then assigned transformed (x, y, z) coordinates based on interpolation between the image and surface geometry. Finally, the transformation is inverted to obtain an orthographic, 3-D heating distribution map of the experimental data. The 3-D mapped data from all runs are presented as large, high-resolution images in Appendix A for the Test 539 Mach 10 data and in Appendix B for the Test 7052 Mach 6 data. Smaller images also will be shown in the body of this report.

In many of the runs, portions of the model back side are blocked by the mounting blade and/or the sting and these regions are shown as white in the images. Reflections from the metallic surface of the blade also

washed-out or otherwise corrupted the data in regions near the blade. Because of the low signal-to-noise ratio of the thermographic phosphor at the low temperatures produced in the wake, surface heating data were spatially averaged where possible to reduce scatter. For $\alpha = 0$ deg. angle-of-attack runs, the data were averaged circumferentially over the portions of the back of the aeroshell that were A) not blocked by the mounting blade, sting, and/or centerbody payload and B) were not corrupted due to poor lighting and/or reflections of the incident UV lights. For the non-zero angle-of-attack runs, the data were circumferentially averaged over a small arc-sector of ±10 degrees from the symmetry plane. The regions over which data were averaged for different model inclinations and camera positions are identified in Figure 19 through Figure 22 by green shading. In the analysis sections to follow, 3-D mapped image data will be shown along with the original intensity images in which these field-of-view blocking and poor lighting effects can be more clearly seen. An example of the ray locations extracted for a back view run is shown in Figure 23 along with the original intensity image.

Heat Transfer Data Uncertainty

As the parameters of this LOFTID test program were similar to those of the THOR test program previously cited [20] other than changes to the HIAD geometry, the methodology for estimating measurement uncertainty developed for the THOR program was applied to the LOFTID data.

The experimental uncertainty in heating data from the front and the back of the aeroshell were characterized separately due to the large differences in flow field characteristics between the two regions. The flow field over the front of the aeroshell was steady and, for these test conditions, laminar. Additionally, the temperature rise over the duration of each run was large (25–75 K at Mach 6 conditions and 50–100 K at Mach 10 conditions) thus providing a very high signal-to-noise ratio for the measurement. These conditions on the front of the aeroshell were well within the standard range of application of the phosphor thermography system (see [24]) for which the uncertainty has been characterized in previous studies. The only limitation with these data is that for the highest unit Reynolds number condition in the Mach 10 tunnel ($Re_\infty = 1.9\times10^6$/ft), temperature levels on the nose exceeded the calibration range of the phosphor thermography system, and thus no usable data were obtained there.

For the measurements on the front of the aeroshell, the experimental uncertainty for heating was estimated from a root-sum-square calculation of the component uncertainties due to the data acquisition method (±10%), the flow quality and test-condition repeatability (±5%), and the accuracy of the 3-D mapping process (±10%), which resulted in an overall value of ±15%. Experience with this technique indicates that these values are usually conservative and, as will be shown later, the predicted and measured heating distributions on the front of the aeroshell are in closer agreement than the uncertainty estimate.

Because of the complexity of blunt body wake flow fields, the determination of heating rates on the back side of a vehicle through either measurement or simulation is very challenging. Wake flow fields typically are characterized by large regions of separated flow that are likely to be both unsteady and turbulent. Thus, the invariance with Reynolds number of normalized heating rates for attached, steady forebody flows is not expected to hold for wake flows.

Additionally, heating rates on the back side of blunt bodies are typically less than 10% of those on the front of the vehicle, which results in a very low temperature rise (less than 10 K for the current study) and thus low signal-to-noise ratios. For such low temperatures, the optical signal intensity from the phosphor emission is very low, leading to a much higher uncertainty than for forebody flows. In the plots of estimated uncertainty vs. surface temperature given in [24], the curves are nearly asymptotic for the temperature range on the back side of the aeroshell in this study and thus cannot be used as a basis for uncertainty estimates.

Although the aeroshell back side heating measurement uncertainty was expected to be very high, analysis of the data showed reasonably consistent results for the effects of Reynolds number and angle of attack. Therefore, in lieu of a theoretical basis for uncertainty estimates, the uncertainty was based on a statistical analysis of the scatter of the data, as follows: for each of the $\alpha = 0$ deg angle-of-attack, back-view runs in the Mach 6 and Mach 10 tunnels, data were extracted along radial lines at $\phi = 10$ deg increments around the circumference of the model, limited as per the earlier discussion on field-of-view blockage and poor lighting regions. Standard deviations (σ) were then computed each radial location, samplings of which are shown in line-plots to follow. Generally, the σ values were on the order of 20% to 30% of the data, depending on position, angle-of-attack, and Reynolds number.

Computational Tools and Methods

Flow Field Solver

Flow field solutions were generated using the Langley Aerothermodynamic Upwind Relaxation Algorithm (LAURA) code. These computations were performed to provide insight into the structure of the wake flow field and to obtain surface heating predictions for comparison with the wind tunnel data. Predicted flow field parameters are also available for comparisons with future wake-flow visualization experiments.

LAURA [26–27] is a three-dimensional, structured-grid, finite-volume solver that includes perfect-gas and nonequilibrium chemistry options, a variety of turbulence models, and ablation and radiative transport capabilities. For this study, laminar, perfect-gas solutions were generated at the nominal test conditions listed in Table 1 for the Mach 10 data set and Table 3 for the Mach 6 data set, with a wall temperature boundary condition of constant 300 K. Because of the unsteady nature of separated, blunt body wake flows, solutions for comparisons with the aeroshell wake heating data were computed using the first-order time marching option and averaged over several hundred thousand iterations to define the aeroshell back side heating levels. Other simpler, forebody-only solutions for comparison with data from the front of the aeroshell were generated using the steady-state option.

Grid Topology

For hypersonic continuum simulations using LAURA, the flow field is usually defined by a structured, hexahedral, multi-block grid topology. While such topologies provide highly accurate simulations over smooth surfaces with slowly-varying curvature, such as the front of an aeroshell, it can be extremely challenging to develop a structured-grid topology to accurately resolve complicated geometries with regions of large curvature and concave surface features, such as the wake flow over the exposed toroids on the back side of LOFTID. Furthermore, even a well-resolved initial wake flow grid is prone to becoming highly-skewed by the shock and boundary-layer grid adaption process, producing artificial numerical dissipation, and hindering the solution convergence process.

For these reasons, a new "stacked-block" structured grid topology and boundary conditions and a new algorithm to adapt and smooth these grids were implemented [28] in the LAURA code to permit more accurate resolution of complicated flow fields. The stacked-block grid topology removes the limitation of defining a grid with continuous *k*-index grid lines from the surface through the shock layer and into the free stream. Instead, the flow domain is decomposed into feature-resolving blocks with arbitrary (*i, j, k*) face-to-face orientation. As illustrated in Figure 24, three new stacked-block topology grid block types were added to the original continuous *k*-line block type, which are defined as:

Type-1: Boundary-layer block with solid-surface *k*-min boundary condition interfacing with a Type-2 block or a Type-4 block at the *k*-max boundary. Type-1 blocks are adapted to cluster points closer to the wall at the *k*-min boundary, but their outer *k*-max boundary point spacing remains fixed.

Type-2: Outer-boundary block with a free stream *k*-max boundary interfacing with a Type-1 block or a Type-4 block at the *k*-min boundary. Type-2 blocks are adapted to expand/contract the *k*-max boundary to encompass the shock, but their inner *k*-min boundary andpoint spacing remains fixed.

Type-3: Standard continuous *k*-line block which can be adapted to cluster cells near the wall and at the shock and to extend/contract the outer boundary to fully encompass the bow shock.

Type-4: Inner block that is bounded on all faces by other Type-1, -2 or -4 blocks. The *i*-*j*-*k* orientation of these blocks with respect to their neighbors is arbitrary. Type-4 blocks cannot be adapted, and their physical *x*-*y*-*z* coordinates remain fixed.

An example of the stacked-block grid topology implementation for a LOFTID wind tunnel case is shown in Figure 25. This stacked-block grid topology allows for much greater flexibility in grid design and results in greater fidelity than the standard topology for configurations such as LOFTID that has a concave shape of the aeroshell back side, exposed toroids and recessed centerbody. However, it should be noted that the grids developed for this study did not include the mounting blade and support sting of the wind tunnel models.

Experimental and Computational Analyses

Aeroshell Front Side Heating Data

NASA LaRC 31-Inch Mach 10 Air Tunnel data from Test 539 on the front of the aeroshell (model A-0-S) are shown in Figure 26 (global images) and Figure 27 (centerline plots). For the Mach 10 tunnel Reynolds number range, the boundary-layer remained laminar at all conditions and the data demonstrated the expected laminar invariance of the normalized film coefficient h/h_{FR}. Because of the high stagnation temperature of the 31-Inch Mach 10 Air Tunnel, surface temperatures at the nose of the model exceeded the phosphor calibration limit for the highest Reynolds number conditions and no data from that region are reported for those cases.

NASA LaRC 20-Inch Mach 6 Air Tunnel data from Test 7052 on the front of the aeroshell (model A-0-S) are shown in Figure 28 (global images) and Figure 29 (centerline plots). For the Mach 6 tunnel Reynolds number range shown here, the boundary layer remained laminar at all conditions and the data demonstrated the expected laminar invariance of the normalized film coefficient h/h_{FR}. At higher Reynolds numbers tested in the Mach 6 tunnel (not shown here) the data did exhibit transitional behavior toward the outer radius of the model.

Aeroshell Back Side and Payload Heating Data

Heating distributions for each Reynolds number condition on the back side and payload of the smooth model S-1 at Mach 10 are shown in Figure 30 through Figure 37 for angles of attack of -5, 0, and +5 deg and for the exposed toroid back side model T-1 in Figure 38 through Figure 45. The limited back side and payload heating data set from Mach 6 are shown in Figure 46 and Figure 47. For each Reynolds number / angle-of-attack / roll angle case, one figure with the 3-D mapped global heating images and the 2-D intensity images is presented and another figure with the circumferentially-averaged line cuts on the back of the

aeroshell and payload are plotted.

On the line plots, data from each of the multiple slices is shown with symbols and the average of all the slices are shown by a solid line. The average temperature rise from the initial conditions along each slice is also shown in these plots. Generally, the temperature rise was less than 5 K for the $Re_\infty = 0.5\times10^6$/ft condition; less than 10 K for the $Re_\infty = 1.0\times10^6$/ft condition; and less than 15 K for the $Re_\infty = 1.9\times10^6$/ft condition. The low temperatures generated on the back of the model were the primary contributor to the higher uncertainty as compared to that for the front of the model.

Considerable scatter can be seen in the image data, due mostly to the low temperatures on the back of the model, but also due to both shadowing and reflections on the back from the support blade as well as from the centerbody. Nevertheless, the circumferentially-averaged data demonstrated consistent trends. On the smooth back side S-1 model, the heating levels were lowest near the centerbody and increased approximately linearly with radial distance from the center of the back side to the shoulder. On the toroid back side model T-1, localized minimums and maximums in the heating levels were produced on each toroid, although the overall magnitude of the heating did not show a significant radial variation. The difference in radial dependency of the heating between the smooth and toroid models was likely due to the toroids' influence on the wake flow field - the concavities between each toroid may have acted as "speed-bumps" that prevented the formation of larger flow structures with higher velocities.

Reynolds Number Effects

The influence of Reynolds number on the aeroshell back side and payload heating is shown for each Mach 10 angle-of-attack / roll-angle case in Figure 48 through Figure 51 for the smooth back side model S-1 and in Figure 52 through Figure 55 for the toroid back side model T-1. The limited Mach 6 data set is presented in Figure 56. For each of the figures, the 3-D mapped heating image is shown for each of the Reynolds numbers along with a line-plot of the circumferentially-averaged heating distributions.

A small increase in the normalized (h/h_{FR}) heating levels with Reynolds number can be seen for each case in these figures. For an attached flow on the forebody of an aeroshell, this behavior would be indicative of turbulent boundary-layer flow. However, given the low Reynolds numbers and low densities produced in the separated wake flow for these cases, turbulent flow may not have been produced or have been sustainable on the back of the aeroshell. Heating (and pressure) is also a function of the shape and volume of the separated wake flow field behind a blunt-body, which is dependent on the pressure in the wake. To conclusively determine the cause of this heating increase, flow-field measurements of the shear-layer state and wake vortex structures would be required to supplement the surface measurements. A separate test program to mature such wake flow field diagnostics techniques for the 31-Inch Mach 10 Air Tunnel was completed [29- 30] after this test program was completed and more detailed measurements are planned.

Angle-of-Attack Effects

Mach 10 run data are organized to show angle-of-attack effects in Figure 57 through Figure 59 for the smooth back side model S-1 and for the toroid back side model T-1 in Figure 60 through Figure 62. There were no angle-of-attack parameters for the Mach 6 test. Only a slight influence on the heating distributions was observed over the small range of angle of attack that was tested (±5 deg). The heating on the back shoulder at the top (+z direction) of the model, which was the only side visible due to the presence of the blade mount, became higher at positive angle of attack when the stagnation point on the forebody was on the opposite side (with reference to the z-axis). Conversely, heating on the +z shoulder became lower at negative angle-of-attack when the stagnation point was on the same side.

Flow Field Simulations and Comparisons with Data

Flow field properties were extracted from the LAURA simulations to provide insight into the structure of the LOFTID wake flow field. These properties are shown for the Mach 10 conditions in Figure 63 (total energy), Figure 64 (pressure), Figure 65 (temperature), Figure 66 (x-velocity component), and Figure 67 (total velocity), and for the Mach 6 conditions in Figure 68 (total energy), Figure 69 (pressure), Figure 70 (temperature), Figure 71 (x-velocity component), and Figure 72 (total velocity). Each of these figures represents a single, instantaneous slice through the vertical symmetry plane and thus does not truly capture the transient nature of the flow within the recirculation region behind the model. Nevertheless, these values are representative of the range of conditions in these flow fields.

The character of the wake flow field predictions is the same for each case, although the levels of the properties vary with Reynolds number. Boundary-layer separation occurs immediately behind the shoulder (the maximum radius point of the aeroshell) of the vehicle, resulting in a separated shear-layer that converges ("necks down") to create a recompression shock approximately one-to-two body diameters downstream of the vehicle. This separated shear layer bounds a low energy, unsteady, recirculating flow region immediately behind the aeroshell.

Notable observations can be made from these figures, including the large difference in total energy levels inside the wake recirculation region behind the aeroshell in comparison to the external flow and the large differences in pressure and temperature between forebody and wake flow regions. With reference to velocity, these figures also illustrate both the chaotic, recirculating nature of the separated vortices immediately behind the aeroshell and the overall lower velocity magnitude with the recirculation region in comparison to the external wake flow.

Ideally, comparisons of predicted and measured flow field properties would be made to evaluate the accuracy of the numerical method. As noted previously, experimental flow field data were obtained in a subsequent test program [29-30]; however, those data were not available for use before this report was completed. While no flow-field comparisons are available yet, comparisons between the experimental and computational surface heating distributions were performed for both the front and back of the LOFTID wind tunnel models.

Comparisons of predicted and measured aeroshell front heating distributions for the Mach 10 and Mach 6 conditions are provided in Figure 73 and Figure 74, respectively. Agreement to within less than 10% was observed for all cases except for a small region on the outer flank of the model at the lowest Reynolds number case at Mach 10, which is within the range expected for comparisons for attached, laminar flow at perfect-gas wind tunnel conditions. These plots also show predicted distributions of the momentum-thickness Reynolds number, Re_θ, for each Reynolds number. For all conditions, values are well below the expected smooth-wall transition onset criterion of $Re_\theta > 200$, indicating that the boundary-layer remained laminar on the front of the aeroshell.

Comparisons of predicted and measured aeroshell back side and payload heating distributions are shown in Figure 75 and Figure 76 for Mach 10 conditions and in Figure 77 and Figure 78 for Mach 6 conditions. These figures also include estimates for the experimental uncertainty as both line plots and error-bars. These uncertainties were very large owing to the low model surface temperature rise.

Predictions for the separated, unsteady wake flow regions were much more challenging than for the forebody flow field. As discussed in the Computational Tools and Methods Section, a new gridding topology was required for these geometries, and the simulations were run in unsteady-mode and time-

averaged over hundreds of thousands of iterations. The wake-flow measurements were also more difficult due to the extremely low surface temperature rise on the models - resulting in low signal-to-noise ratios - as well as the illumination and viewing angle challenges on the back of the model.

Heating comparisons on the payload were acceptable – which is to say they were generally bounded by the experimental uncertainty - for all cases except the Mach 6 toroid case for which only minimal payload data were obtained. Unlike the laminar aeroshell front side data, the back side data were not constant with Reynolds number, which was indicative of either non-laminar flow or variations in the separated region volume and enclosed vortex structure with dynamic pressure at the different Reynolds number conditions.

Heating comparisons on the back of the aeroshell were not consistent between the model geometries and test Mach numbers. For the smooth back side Mach 6 and Mach 10 cases, the predicted heating distributions showed a large peak between r/R = 0.4 to 0.5 that was not evident in the experimental data. Good agreement between predictions and measurements for the toroid back side was observed for the Mach 10 conditions but not for the Mach 6 conditions. As noted in the earlier discussion of the experimental program, the phosphor coatings on the wind tunnel models had been noticeably degraded prior to the Mach 6 test entry. Thus, the Mach 6 dataset was only considered to be qualitative and was not suitable for comparisons with predictions.

The differences in the character of the smooth and toroid back side geometry comparisons at Mach 10 warrant further exploration. One possible reason for the better comparison for the Mach 10 toroid back side than for the Mach 10 smooth back side was the quality of the computational grids. The smooth back side grid was the first prototype of the stacked-block topology developed for wake flow simulations, while the toroid back side grid was developed after running the smooth backface simulations. That experience aided in the development of a toroid wake topology that better captured the features of the flow field. Schedule limitations precluded developing a better smooth wake grid and re-running the simulations.

Although these comparisons did show significant differences between predictions and measurements on the back of the aeroshell and on the payload for many cases, the data set was still valuable to the LOFTID flight test program. The stacked-block gridding topology and time-stepping simulation methodology discussed herein was employed to generate the flight database, to which conservatively large uncertainty factors were added that were based in part on these comparisons.

Summary and Conclusions

An experimental wind tunnel test program was conducted to obtain convective heating data on the payload and back side of the aeroshell of LOFTID vehicle. Data were obtained at Mach 10 and Mach 6 conditions on both smooth and toroid back side representations of the LOFTID geometry that provided insight into the nature of the wake flow heating environments. In parallel to the test program, a computational study was performed to generate predictions for the flow environments and surface heating distributions. The computational study demonstrated the viability of the “stacked-block” topology for the generation of structure numerical grids for complex topologies. The comparisons between measurements and predictions provided a basis for conservative margins on the aeroheating database for the LOFTID vehicle, which flew successfully in November of 2022.

It is recommended that a more thorough, follow-up test program be conducted to obtain additional aeroheating data. Such tests were defined in the LOFTID project plan but enforced teleworking at NASA during the height of the COVID pandemic in 2020-2021 resulted in the cancellation of additional planned wind tunnel tests.

In particular, the existing, qualitative Mach 6 data set should be replaced with higher quality data. Additional Mach 10 testing is also warranted with considerations for improving the fidelity of the aeroshell back side heating data by using other measurement techniques such as discrete heat-transfer sensors or infrared thermography. A calibration of the phosphor thermography system biased towards a low-temperature environment rather than a wide range of temperature also should be considered to increase the accuracy of aeroshell back side measurements.

Finally, the computational flow field solutions can be used as a starting point for comparisons with wake flow visualization tests on the LOFTID geometry that were conducted after this test program. A more thorough computational study is warranted, with further development of the structured, stacked-block grid topology as well as evaluation of the use of unstructured grid flow-solvers.

Acknowledgments

This work was supported by the NASA Space Technology Mission Directorate through the LOFTID Project of the Technology Demonstration Program and the Entry Systems Modeling Project of the Game Changing Development Program.

References

1. Hollis, B. R., Wise, A. J., Liechty, D. S, Korzun, A. M., Thompson, K. B., Rodrigues, N. S., and Rieken, E. F., "Aerothermodynamic Analyses for the LOFTID Technology Demonstration Mission," AIAA Paper 2024-1498, AIAA SciTech Forum, Orlando, FL, January 8-12, 2024.
2. Tobin, S. A., Brune, A. J., and Bowes, A. L., "Probabilistic Aeroshell Thermal Response Uncertainty Analysis for the LOFTID Technology Demonstration Mission," AIAA Paper 2024-1499, AIAA SciTech Forum, Orlando, FL, January 8-12, 2024.
3. Hughes, S. J., Cheatwood, F. M., Dillman, R. A., Wright, H. S., DelCorso, J. A. and Calomino, A. M., "Hypersonic Inflatable Aerodynamic Decelerator (HIAD) Technology Development Overview," AIAA Paper 2011-2525, 21st AIAA Aerodynamic Decelerator Systems Technology Conference and Seminar, Dublin, Ireland, May 23–26, 2011.
4. Dwyer Cianciolo, A. M., Davis, J. K., Komar, D. R., Munk, M. M., et al.," Entry, Descent and Landing Systems Analysis Study: Phase 1 Report," NASA TM-2010-216720, July 2010.
5. Dwyer Cianciolo, A. M., Davis, J. L., Engelund, W. C., Komar, D. R, et al., "Entry, Descent and Landing Systems Analysis Study: Phase 2 Report on Exploration Forward Systems," NASA TM-2011-217055, February 2011.
6. Dwyer Cianciolo, A. M., Dillman, R. A., Brune, A. J., Lugo, R. A., et al., "Human Mars Entry, Descent and Landing Architecture Study: Deployable Decelerators," AIAA Paper 2018-5191, AIAA Space Forum, Orlando, FL, September 17-19, 2018.
7. Gillette, J. E., Larson, C. and Reed, J. G.," Vulcan Centaur Reuse: The Next Step to Accessible and Affordable Space," AIAA Paper 2022-4253, AIAA Ascend 2022, October 24-26, 2022.
8. Hughes, S. J., Dillman, R. A., Starr, B. R., et al., "Inflatable Re-entry Vehicle Experiment (IRVE) Design Overview," AIAA Paper 2005-1636, 18th AIAA Aerodynamic Decelerator Systems Technology Conference and Seminar, Munich, Germany, May 23-26, 2005.
9. Moss, J. N., Glass, C. E., and Hollis, B. R., "Low-Density Aerodynamics of the Inflatable Re-entry Vehicle Experiment (IRVE)," AIAA Paper 2006-1189, 44th AIAA Aerospace Sciences Meeting and Exhibit, Reno, NV, January 9-12, 2006.
10. Lindell, M .C., Hughes, S. J., Dixon, M. and Willey, C. E., "Structural Analysis and Testing of the Inflatable Re-entry Vehicle Experiment (IRVE)," AIAA Paper 2006-1699, 47th AIAA/ASME/ASCE/AHS/ASC Structures, Structural Dynamics, and Materials Conference, Newport, RI, May 1-4, 2006.
11. Dillman, R. A., Hughes, S. J., Bodkin, R. J., et al., "Flight Performance of the Inflatable Reentry Vehicle Experiment II," International Planetary Probe Workshop (IPPW-7), Barcelona, Spain, June 14-18, 2010.
12. O'Keefe, S. A. and Bose, D. M., "IRVE-II Post-Flight Trajectory Reconstruction," AIAA Paper 2010-7515, AIAA Atmospheric Flight Mechanics Conference, Toronto, Canada, August 2-5, 2010.
13. Bose, D. M., Toniolo, M. D., Cheatwood, F. M., et al., "Impact of Vehicle Flexibility on IRVE-II Flight Dynamics," AIAA Paper 2011-2571, 21st AIAA Aerodynamic Decelerator Systems Technology Conference and Seminar, Dublin, Ireland, May 23-26, 2011.
14. Lichodziejewski, L., Kelley, C., Tutt, B. et al., "Design and Testing of the Inflatable Aeroshell for the IRVE-3 Flight Experiment," AIAA Paper 2012-1515, 53rd AIAA/ASME/ASCE/AHS/ASC Structures, Structural Dynamics and Materials Conference, Honolulu, HI, April 23-26, 2012.
15. Olds, A. D., Beck, R. E., Bose, D. M., et al., "IRVE-3 Post-Flight Reconstruction", AIAA Paper 2013-1390, AIAA Aerodynamics Decelerator Systems Conference, Daytona Beach, FL, March 25-28, 2013.

16. DiNonno, J. M. and Cheatwood, F. M., "Low-Earth Orbit Flight Test of an Inflatable Decelerator (LOFTID) Mission Overview and Science Return," AIAA Paper 2024-1309, AIAA SciTech Forum, Orlando, FL, January 8-12, 2024.

17. Bodkin, R. J., Akamine, R. L. Blakeley, H. S., et al., "The Design of the Low-Earth Orbit Flight Test of an Inflatable Decelerator (LOFTID) Reentry Vehicle (RV)," AIAA Paper 2024-1310, AIAA SciTech Forum, Orlando, FL, January 8-12, 2024.

18. Hughes, S. J., Cheatwood, F. M, DiNonno, J. M, and Swanson, G. T., "Low-Earth Orbit Flight Test of an Inflatable Decelerator (LOFTID) Aeroshell Performance," AIAA Paper 2024-1314, AIAA SciTech Forum, Orlando, FL, January 8-12, 2024.

19. Berger, K., Rufer, S., Hollingsworth, K. and Wright, S., "NASA Langley Aerothermodynamic Laboratory: Hypersonic Testing Capabilities," AIAA Paper 2015-1337, 53rd AIAA Aerospace Sciences Meeting, Kissimmee, FL, January 5-9, 2015.

20. Hollis, B. R., Berry, S. A., Hollingsworth, K. E., and Wright, S. A., "Experimental Study of Convective Heating on the Backface and Payload of a Hypersonic Inflatable Aerodynamic Decelerator (HIAD) Aeroshell," NASA-TP-2017-219581, March 2017.

21. Buck, G. M., "Rapid Model Fabrication and Testing for Aerospace Vehicles," AIAA Paper 2000-0826, 38th AIAA Aerospace Sciences Meeting and Exhibit, Reno, NV, January 10-13, 2000.

22. Fay, J. A., and Riddell, F. R., "Theory of Stagnation Point Heat Transfer in Dissociated Air," *Journal of Aeronautical Sciences*, Vol. 25, No. 2., February 1958, pp. 73-85.

23. Buck, G. M., "Surface Temperature/Heat Transfer Measurement Using a Quantitative Phosphor Thermography System," AIAA Paper 91-0064, 29th Aerospace Sciences Meeting, Reno, NV, January 7-10, 1991.

24. Merski, N. R., "Global Aeroheating Wind-Tunnel Measurements Using Improved Two-Color Phosphor Thermography Methods," *Journal of Spacecraft and Rockets*, Vol. 36, No. 2, March-April 1999, pp. 160-170.

25. Mason, M. L. and Rufer, S. J., "Imaging for Hypersonic Experimental Aeroheating Testing (IHEAT) version 4.0: User Manual," NASA/TM-2018-220113, November 2018.

26. Gnoffo, P. A., "An Upwind-Biased, Point-Implicit Algorithm for Viscous, Compressible Perfect-Gas Flows," NASA TP-2953, February 1990.

27. Thompson, K. B. Hollis, B. R., Johnston, C. O., Kleb, B. L, Lessard, V. R. and Mazaheri, A., "LAURA User's Manual: 5.6," NASA TM-2020-220566, February 2020.

28. Thompson, K. B., Wise, A. J., Hollis, B. R., and Hinkle, A. D., "Improvements to the LAURA Mesh Adaptation Algorithm," AIAA Paper 2023-4332, AIAA Aviation Forum, San Diego, CA, June 12-16, 2023.

29. Rodrigues, N. S., Tyrrell, O. K., Rieken, E. F., Hollis, B. R., and Danehy, P. M, "FLEET and PLIF Velocimetry Within a Mach 10 Hypersonic Air Flow," AIAA Paper 2024-2323, AIAA SciTech Forum, Orlando, FL, January 8-12, 2024.

30. Rodrigues, N. S., Tyrrell, O. K., Danehy, P. M., Rieken, E. F., Hollis, B. R., Robbins, A. W., Reynolds, T. and Wright, S. A., "Application of PLIF to Investigate the Hypersonic Wake of a LOFTID-Relevant Model at Mach 10", NASA/TM-20240000817, April 2024.

Table 1. Averaged Nominal Conditions for 31-Inch Mach 10 Air Tunnel Test 539.

Re_∞ (1/ft)	Re_∞ (1/m)	M_∞	T_∞ (K)	ρ_∞ (kg/m^3)	U_∞ (m/s)	ΔH_{TOT} (J/kg)	h_{FR} (kg/m^2-s)
5.301E+05	1.739E+06	9.68	51.86	4.607E-03	1397.5	7.277E+05	1.424E-01
1.048E+06	3.440E+06	9.81	50.99	8.920E-03	1403.2	7.348E+05	1.991E-01
1.862E+06	6.109E+06	9.94	49.66	1.546E-02	1400.4	7.294E+05	2.615E-01

Table 2. 31-Inch Mach 10 Air Tunnel Test 539 Run Matrix.

Run	Configuration	α_∞ (deg)	ϕ_∞ (deg)	Re_∞ (1/ft)	M_∞	T_∞ (K)	ρ_∞ (kg/m^3)	U_∞ (m/s)	ΔH_{TOT} (J/kg)	h_{FR} (kg/m^2-s)
4	A-0-S	0	0	5.308E+05	9.68	51.78	4.610E-03	1396.6	7.262E+05	1.422E-01
7	A-0-S	0	30	5.270E+05	9.68	52.06	4.589E-03	1400.1	7.314E+05	1.423E-01
2	A-0-S	0	0	1.051E+06	9.81	50.93	8.934E-03	1402.5	7.337E+05	1.989E-01
8	A-0-S	0	30	1.040E+06	9.81	51.30	8.876E-03	1407.3	7.409E+05	1.991E-01
5	A-0-S	0	0	1.854E+06	9.94	49.85	1.542E-02	1403.1	7.334E+05	2.614E-01
10	A-0-S	0	30	1.864E+06	9.94	49.70	1.548E-02	1401.0	7.303E+05	2.615E-01
15	S-1	-5	0	5.303E+05	9.68	51.87	4.609E-03	1397.8	7.281E+05	1.423E-01
16	S-1	-5	0	1.035E+06	9.81	51.37	8.843E-03	1408.2	7.423E+05	1.989E-01
18	S-1	-5	0	1.877E+06	9.94	49.46	1.555E-02	1397.8	7.255E+05	2.614E-01
13	S-1	0	0	5.277E+05	9.68	51.99	4.592E-03	1399.2	7.302E+05	1.422E-01
12	S-1	0	0	1.037E+06	9.81	51.33	8.855E-03	1407.8	7.416E+05	1.989E-01
33	S-1	0	90	1.067E+06	9.82	50.42	9.024E-03	1395.8	7.239E+05	1.988E-01
14	S-1	0	0	1.856E+06	9.94	49.79	1.542E-02	1402.1	7.320E+05	2.613E-01
34	S-1	0	90	1.881E+06	9.94	49.40	1.557E-02	1396.9	7.243E+05	2.613E-01
20	S-1	5	0	5.328E+05	9.68	51.71	4.623E-03	1395.7	7.249E+05	1.423E-01
21	S-1	5	0	1.044E+06	9.81	51.11	8.892E-03	1404.8	7.371E+05	1.988E-01
19	S-1	5	0	1.856E+06	9.94	49.82	1.543E-02	1402.7	7.327E+05	2.614E-01
31	T-1	-5	0	5.295E+05	9.68	51.91	4.604E-03	1398.2	7.287E+05	1.423E-01
32	T-1	-5	0	1.044E+06	9.81	51.09	8.891E-03	1404.5	7.367E+05	1.988E-01
30	T-1	-5	0	1.858E+06	9.94	49.60	1.542E-02	1399.4	7.280E+05	2.606E-01
25	T-1	0	0	5.287E+05	9.68	51.92	4.597E-03	1398.3	7.288E+05	1.422E-01
36	T-1	0	90	5.298E+05	9.68	51.86	4.604E-03	1397.6	7.278E+05	1.422E-01
26	T-1	0	0	1.057E+06	9.81	50.73	8.973E-03	1399.8	7.298E+05	1.989E-01
35	T-1	0	90	1.051E+06	9.81	50.94	8.934E-03	1402.6	7.339E+05	1.989E-01
24	T-1	0	0	1.867E+06	9.94	49.61	1.550E-02	1399.8	7.285E+05	2.613E-01
37	T-1	0	90	1.867E+06	9.94	49.64	1.550E-02	1400.2	7.291E+05	2.614E-01
27	T-1	5	0	5.285E+05	9.68	51.96	4.598E-03	1398.8	7.296E+05	1.423E-01
28	T-1	5	0	1.054E+06	9.81	50.84	8.952E-03	1401.3	7.319E+05	1.989E-01
29	T-1	5	0	1.841E+06	9.94	50.04	1.535E-02	1405.6	7.372E+05	2.614E-01

Table 3. Averaged Nominal Conditions for 20-Inch Mach 6 Air Tunnel Test 7052.

Re_∞ (1/ft)	Re_∞ (1/m)	M_∞	T_∞ (K)	ρ_∞ (kg/m^3)	U_∞ (m/s)	ΔH_{TOT} (J/kg)	h_{FR} (kg/m^2-s)
1.050E+06	3.446E+06	5.89	62.24	1.651E-02	931.9	1.958E+05	1.664E-01
2.103E+06	6.900E+06	5.97	62.79	3.281E-02	947.4	2.109E+05	2.394E-01
3.012E+06	9.883E+06	6.00	63.03	4.689E-02	953.3	2.168E+05	2.879E-01
4.028E+06	1.322E+07	6.01	62.22	6.219E-02	948.5	2.113E+05	3.295E-01

Table 4. 20-Inch Mach 6 Air Tunnel Test 7052 Run Matrix.

Run	Configuration	α_∞ (deg)	ϕ_∞ (deg)	Re_∞ (1/ft)	M_∞	T_∞ (K)	ρ_∞ (kg/m^3)	U_∞ (m/s)	ΔH_{TOT} (J/kg)	h_{FR} (kg/m^2-s)
105	A-0-S	0	0	1.08E+06	5.89	62.3	1.694E-02	932.38	1.963E+05	1.685E-01
106	A-0-S	0	0	2.03E+06	5.96	62.7	3.171E-02	946.33	2.098E+05	2.347E-01
107	A-0-S	0	0	3.02E+06	6.00	62.9	4.705E-02	952.29	2.157E+05	2.881E-01
100	S-1	0	0	1.04E+06	5.89	62.3	1.645E-02	931.67	1.957E+05	1.659E-01
98	S-1	0	0	2.04E+06	5.97	62.7	3.181E-02	946.56	2.101E+05	2.351E-01
101	S-1	0	0	3.01E+06	6.00	63.0	4.684E-02	953.06	2.165E+05	2.877E-01
97	S-1	0	0	3.05E+06	6.00	62.9	4.742E-02	952.24	2.156E+05	2.892E-01
99	S-1	0	0	4.02E+06	6.01	62.1	6.211E-02	948.15	2.110E+05	3.292E-01
102	S-1	0	0	4.04E+06	6.01	62.2	6.233E-02	948.64	2.115E+05	3.300E-01
103	T-1	0	0	3.01E+06	6.00	63.1	4.689E-02	954.30	2.179E+05	2.883E-01
104	T-1	0	0	4.02E+06	6.01	62.2	6.213E-02	948.58	2.114E+05	3.294E-01

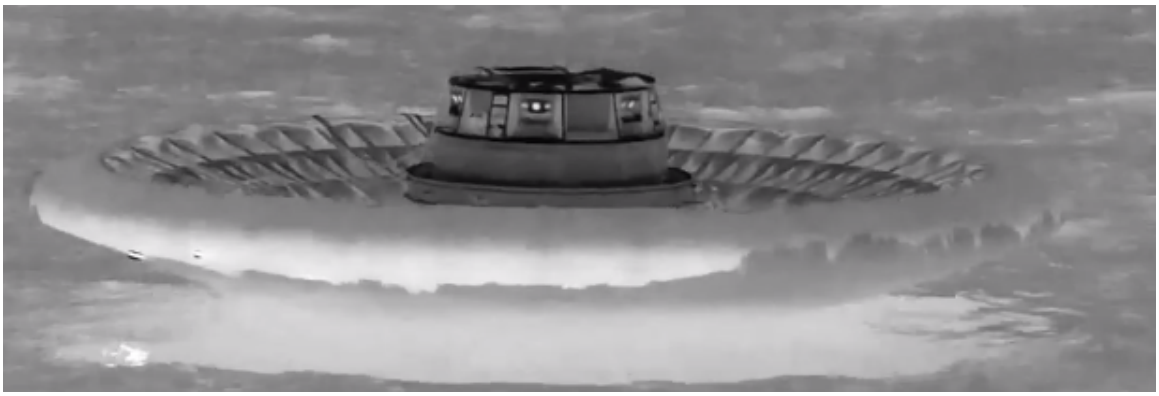


Figure 1. Infrared image of LOFTID splashdown [Source NASA].



Figure 2. Recovered LOFTID flight vehicle [Source NASA].

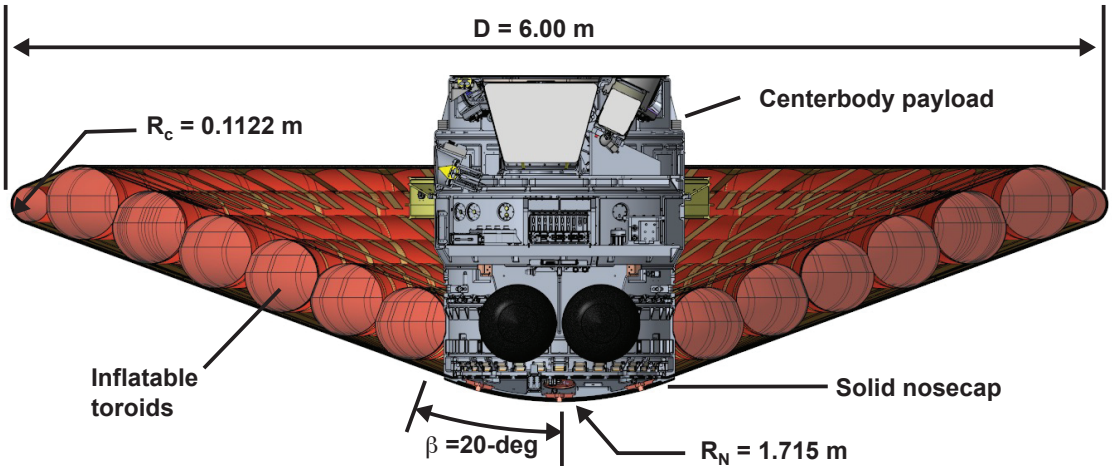
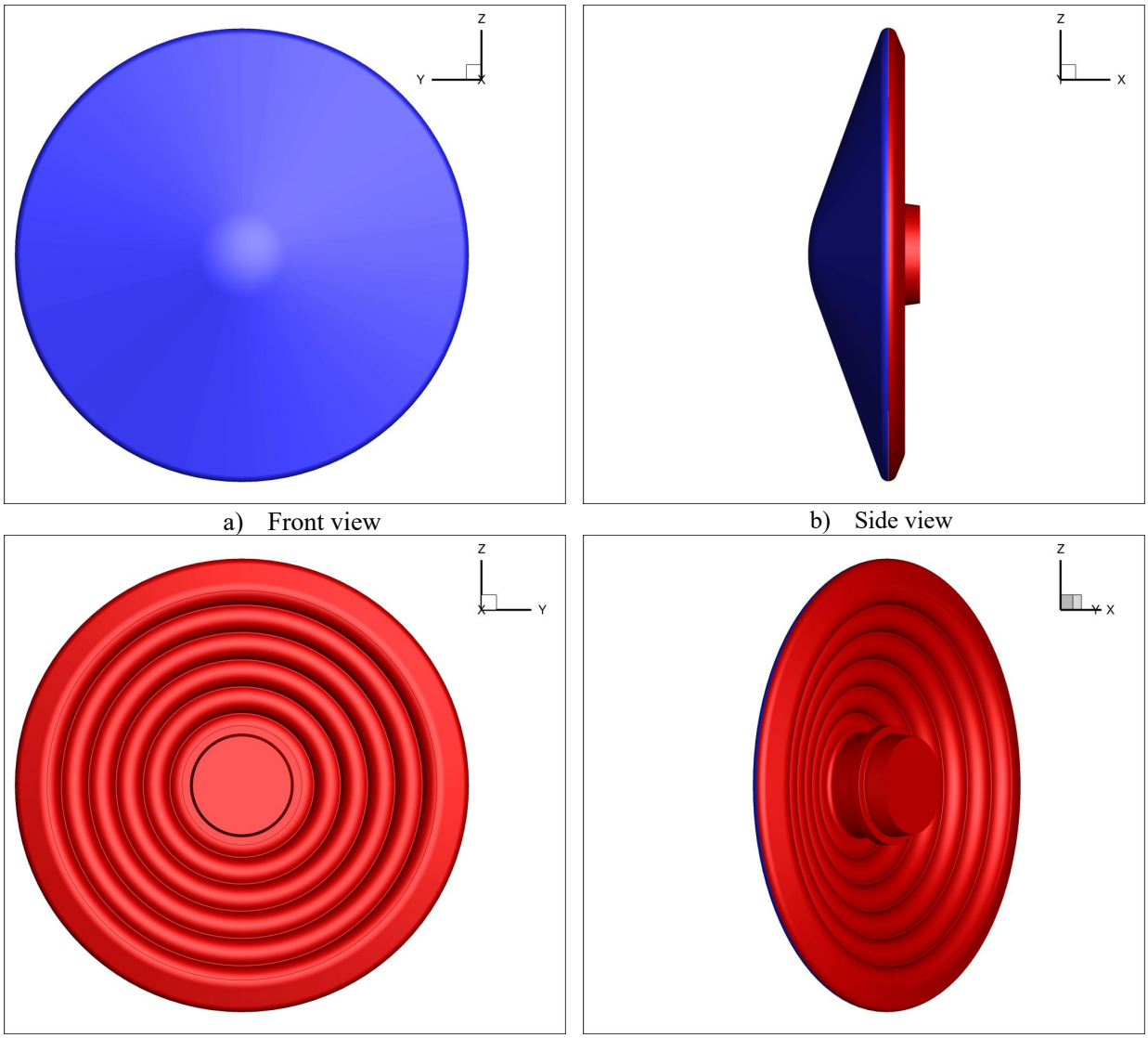


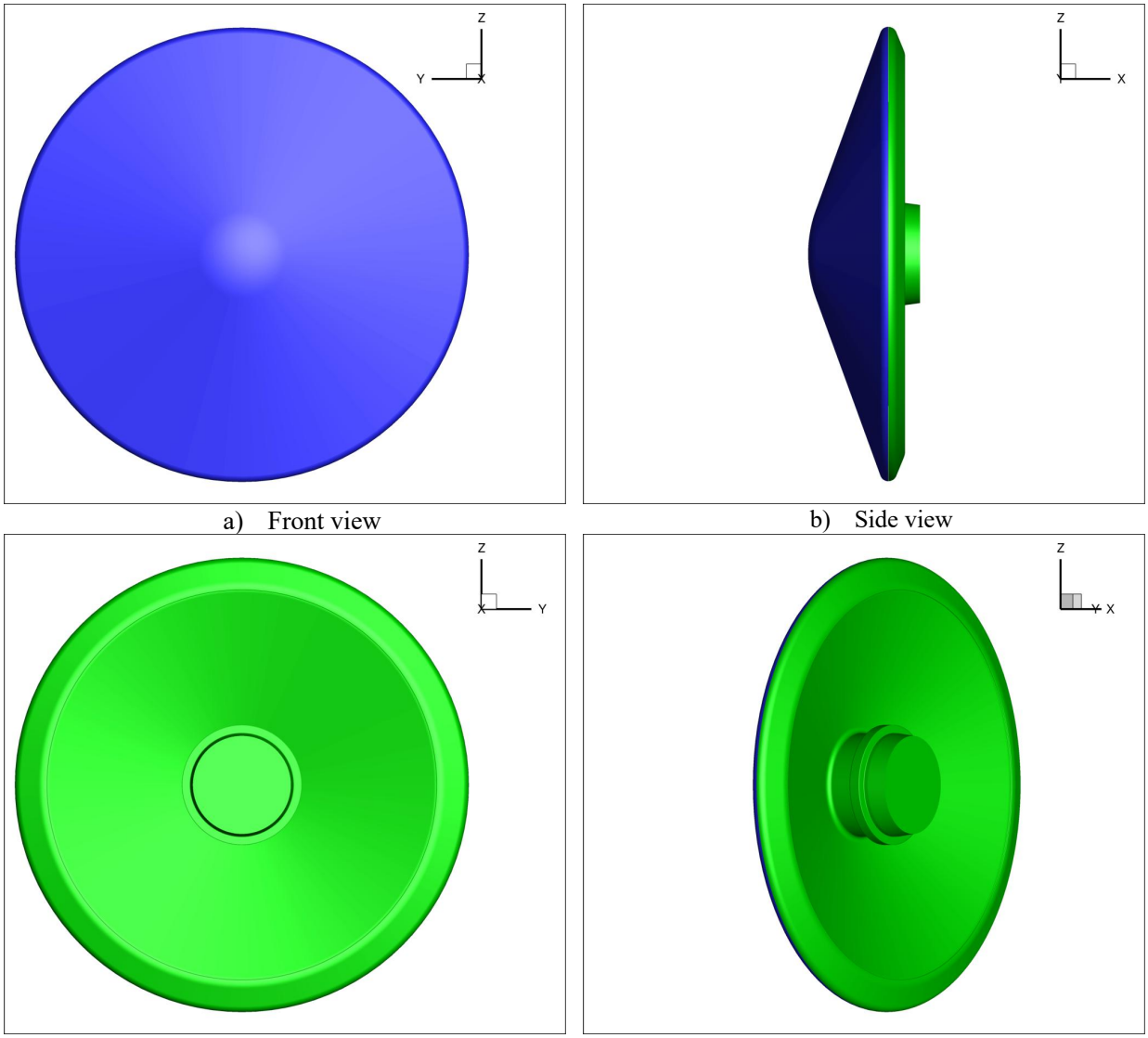
Figure 3. LOFTID flight vehicle cross section and dimensions.



a) Front view b) Side view

c) Rear view d) Oblique view

Figure 4. LOFTID exposed toroid back side geometry (T-1).



a) Front view b) Side view

c) Rear view d) Oblique view

Figure 5. LOFTID smooth back side geometry (S-1).

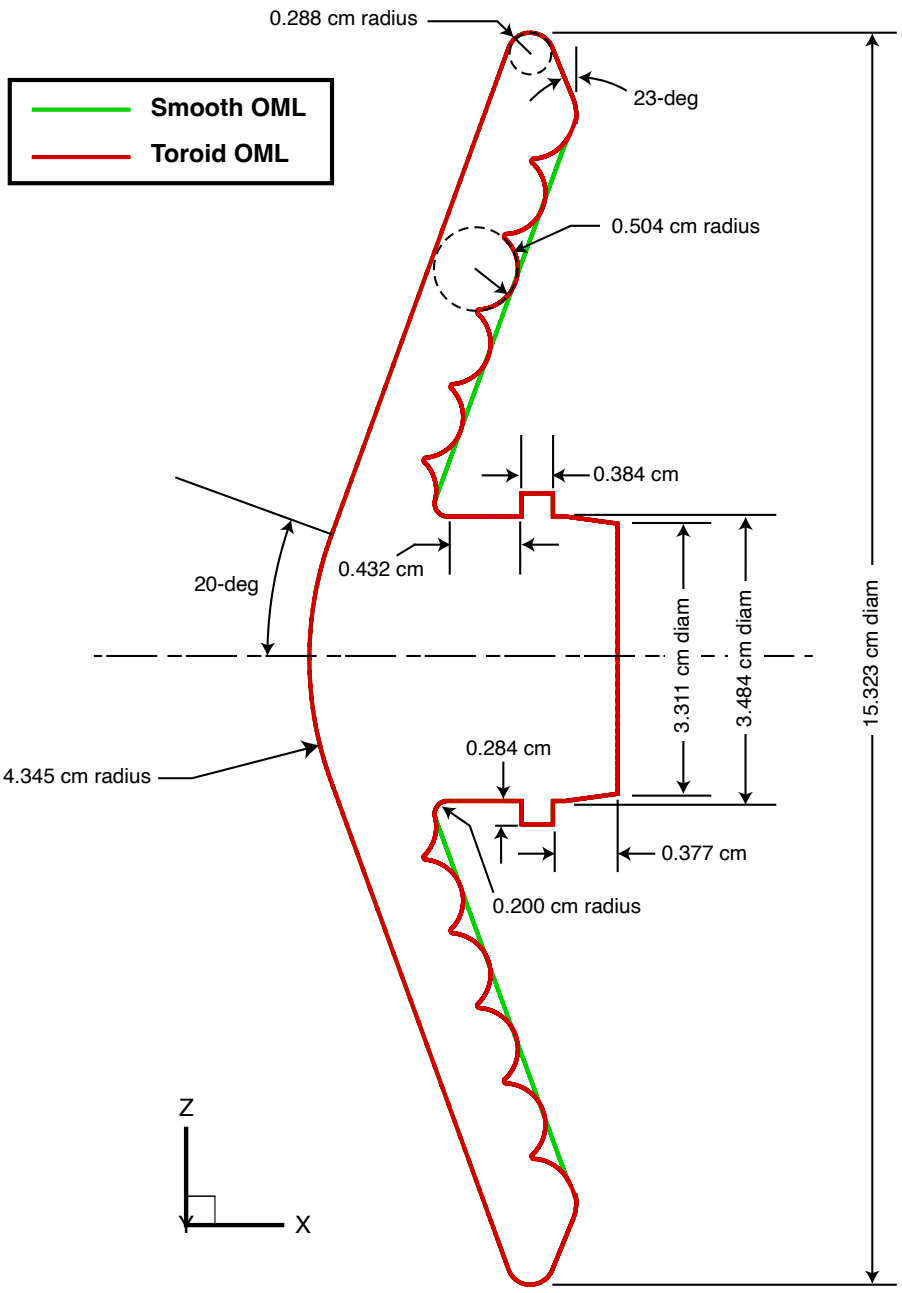


Figure 6. Smooth and toroid model outer mold lines and dimensions.

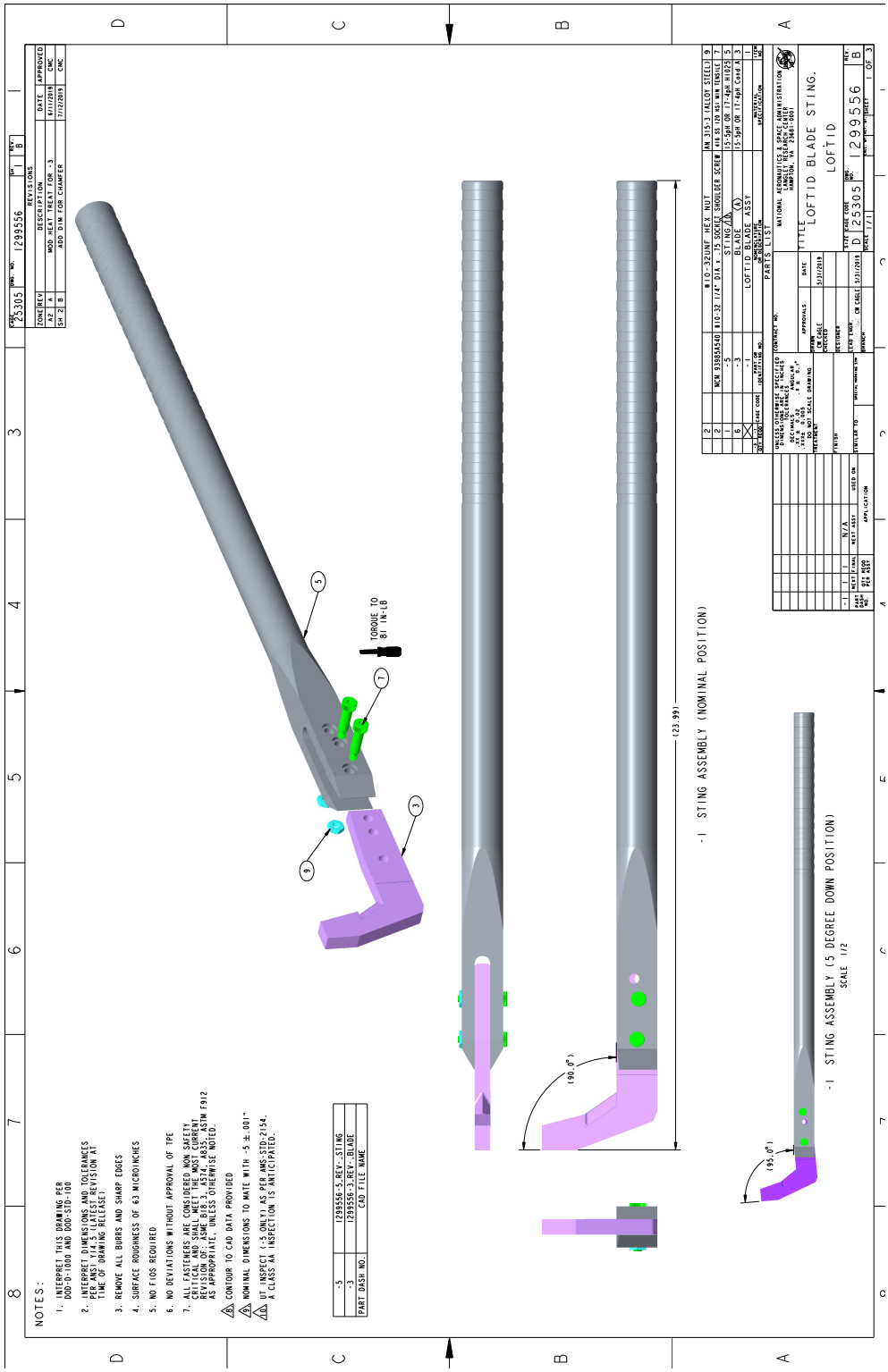


Figure 7. Support hardware configuration for models T-1 and S-1.

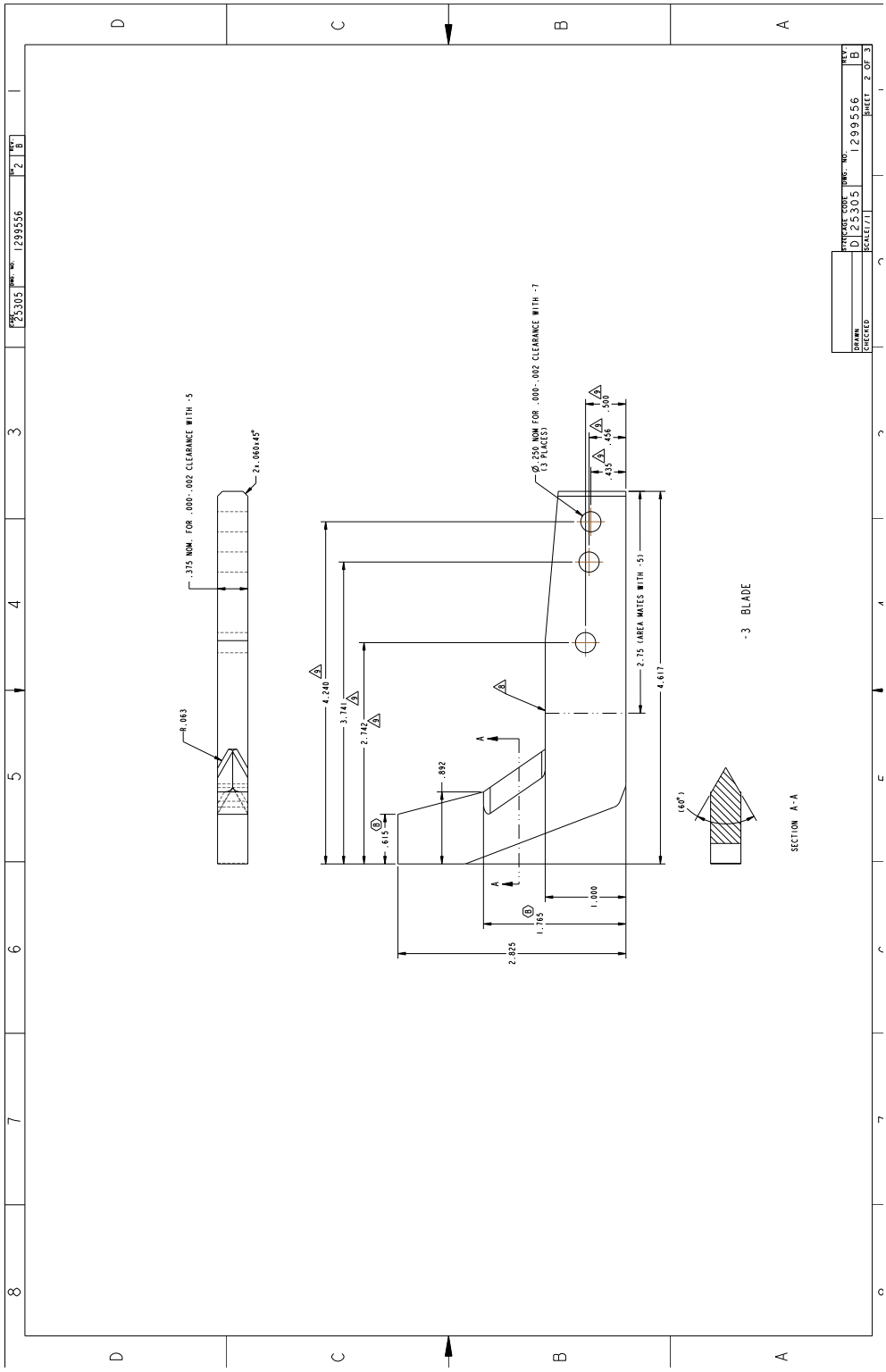


Figure 8. Support hardware: blade details.

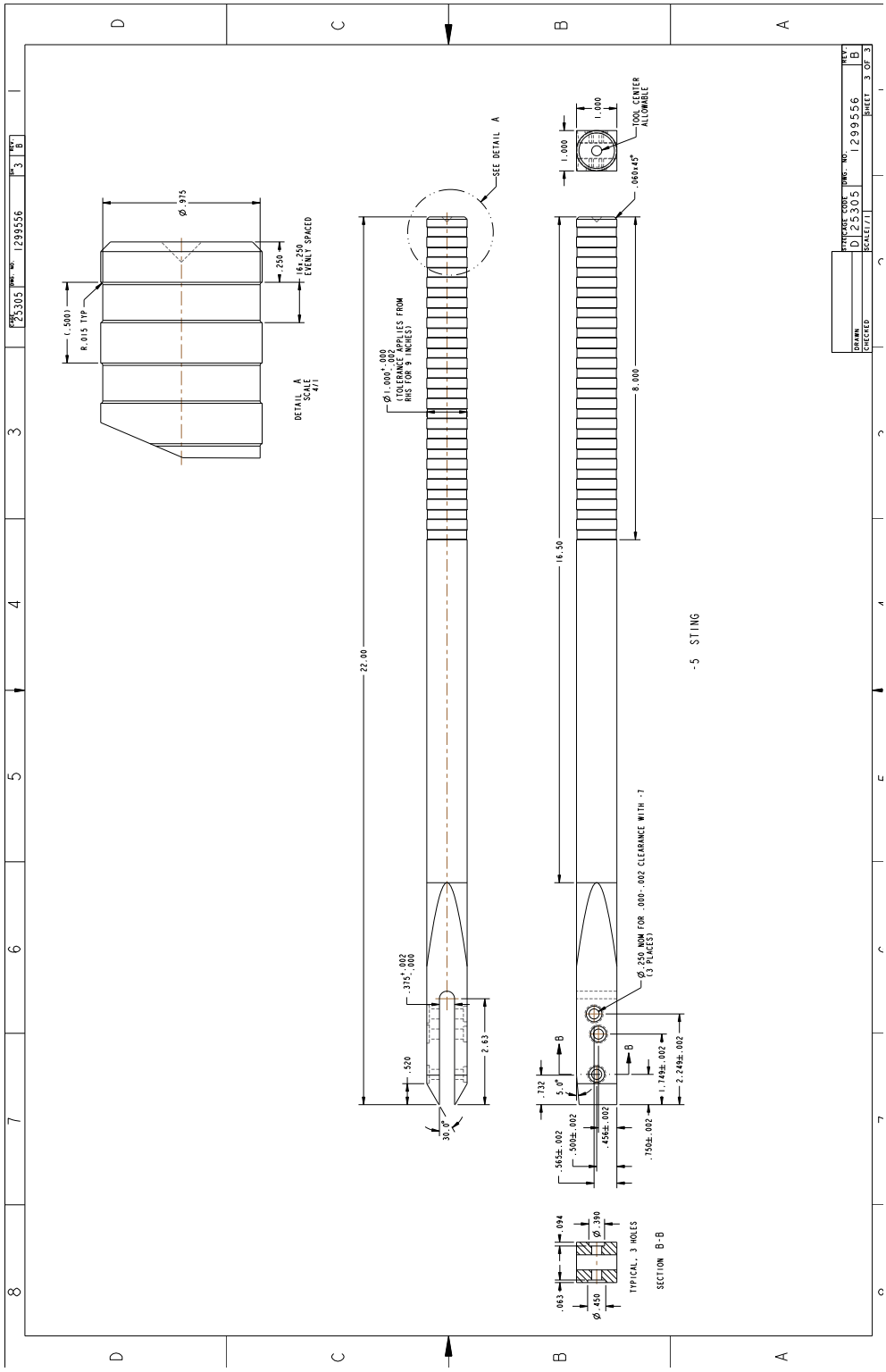
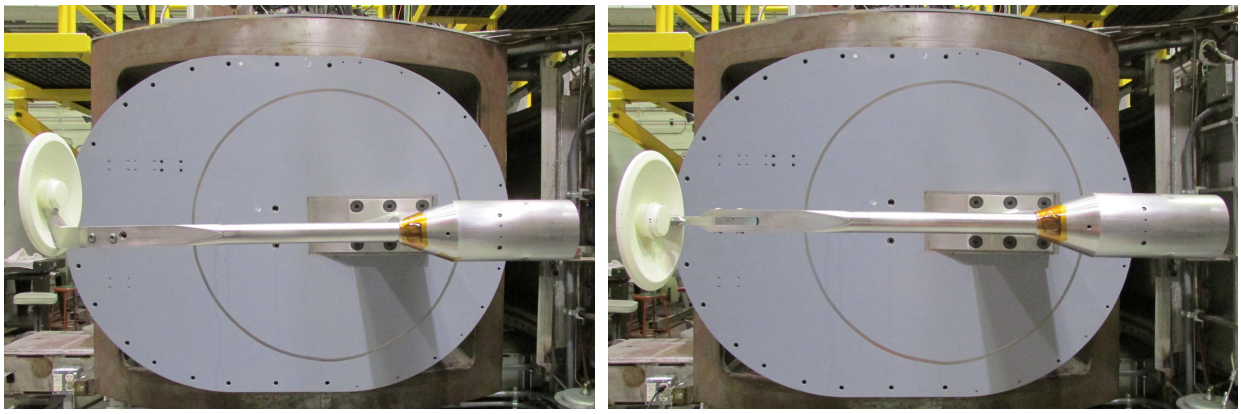
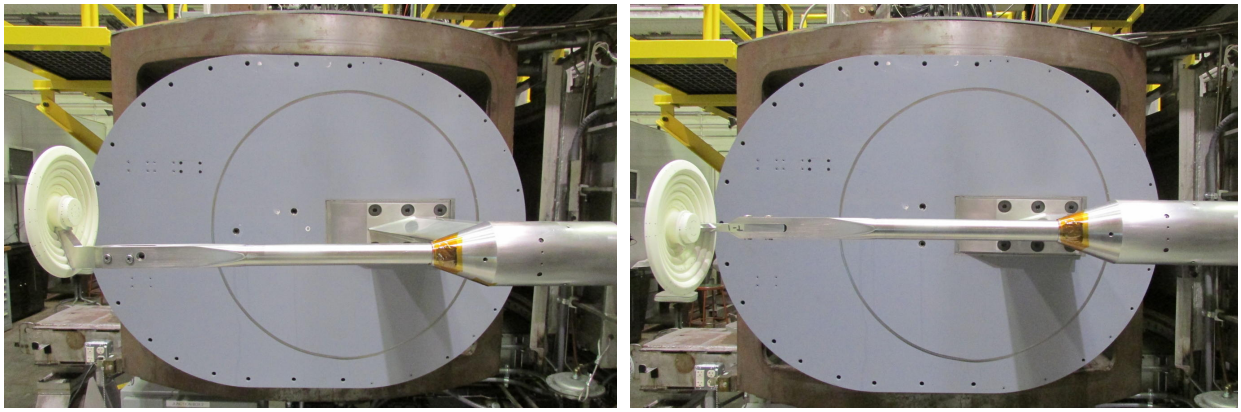


Figure 9. Support hardware: sting details.



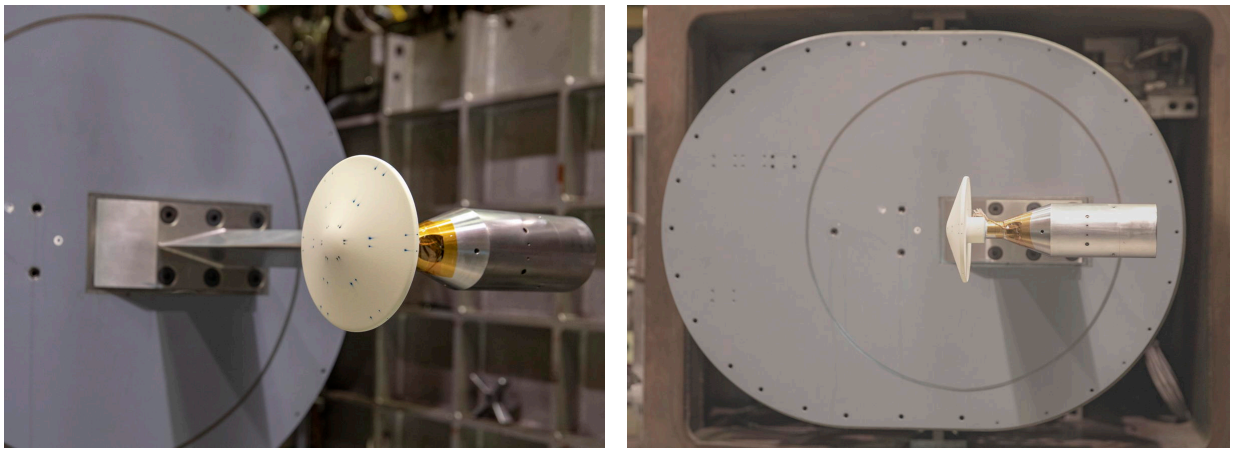
a) ϕ = 0 deg. orientation b) ϕ = 90 deg. orientation.

Figure 10. Smooth model S-1 rear view photographs (source NASA).



a) ϕ = 0 deg. orientation. b) ϕ = 90 deg. orientation.

Figure 11. Toroid model T-1 rear view photographs (source NASA).



a) Front view. b) Side view.

Figure 12. Front view photographs of model A-0-S (source NASA).

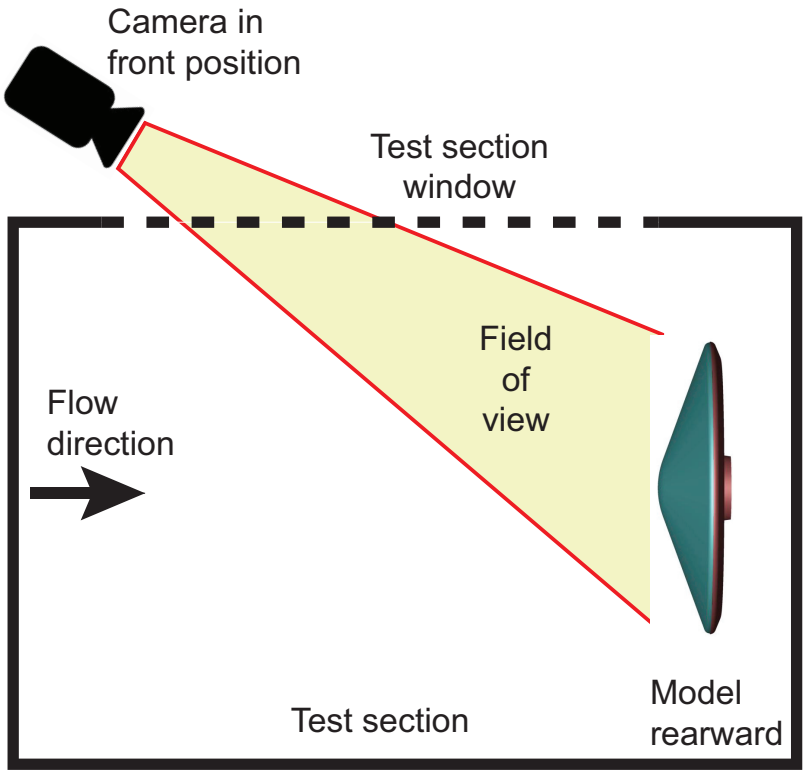


Figure 13. Setup for model front view (not to scale).

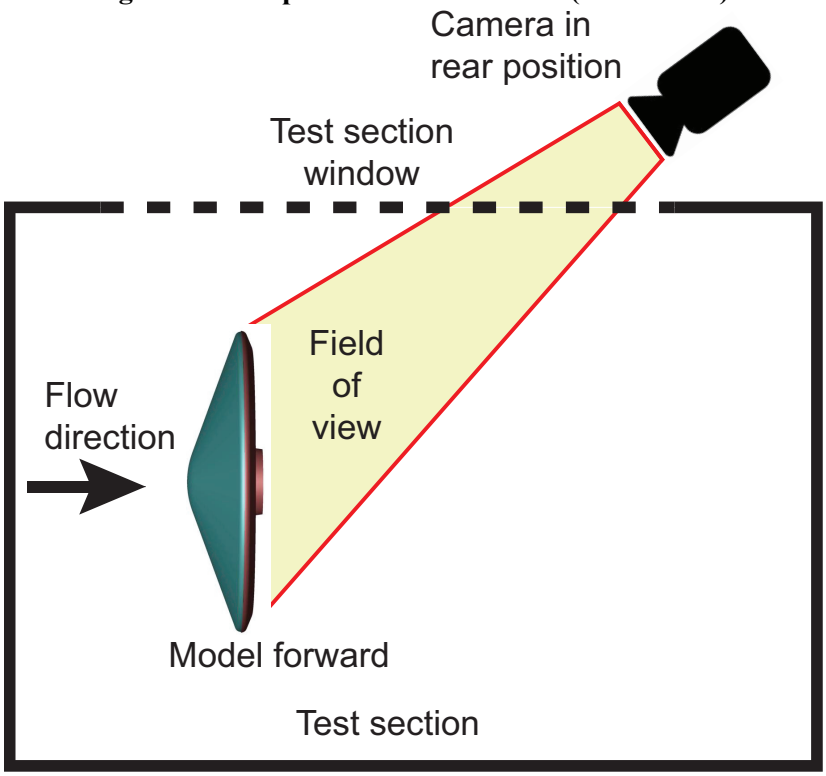


Figure 14. Setup for model back view (not to scale).

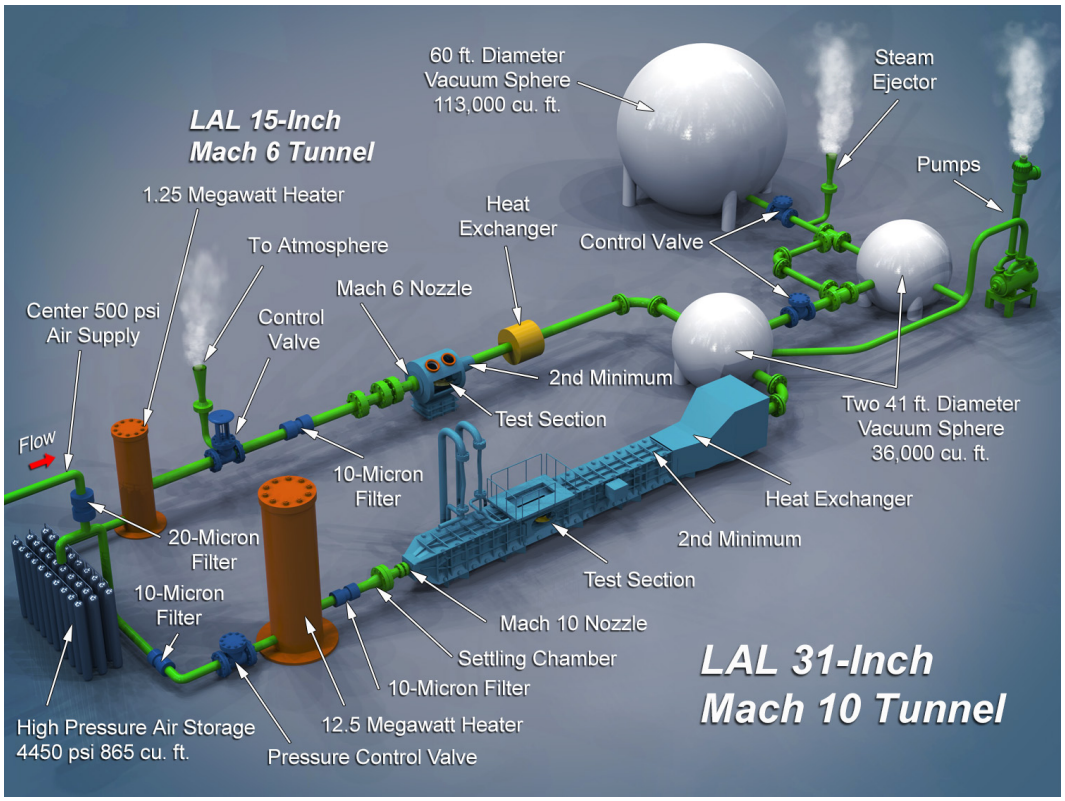


Figure 15. Schematic of Langley Research Center 31-Inch Mach 10 Air Tunnel.

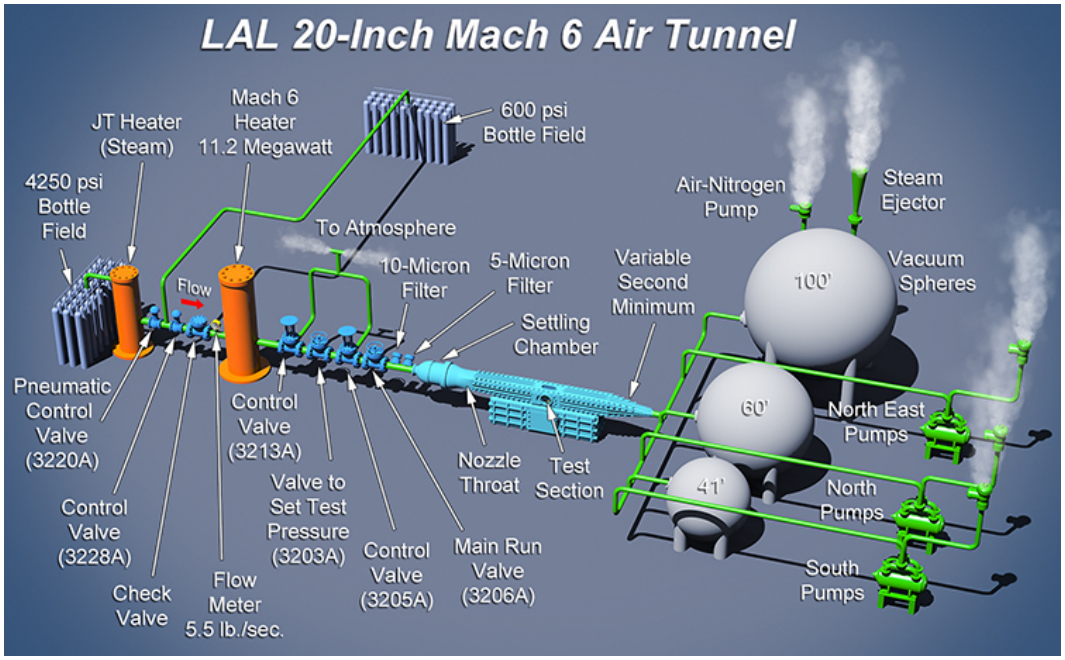
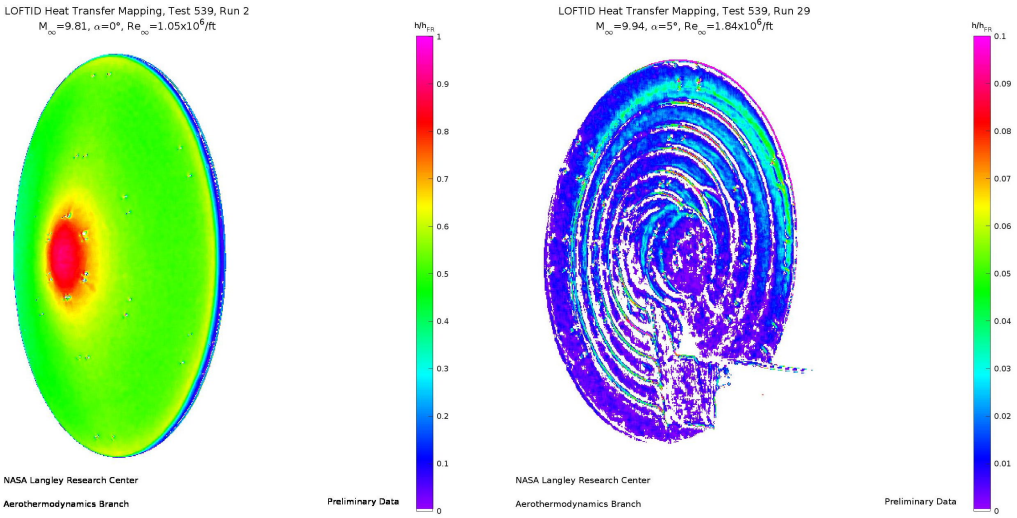
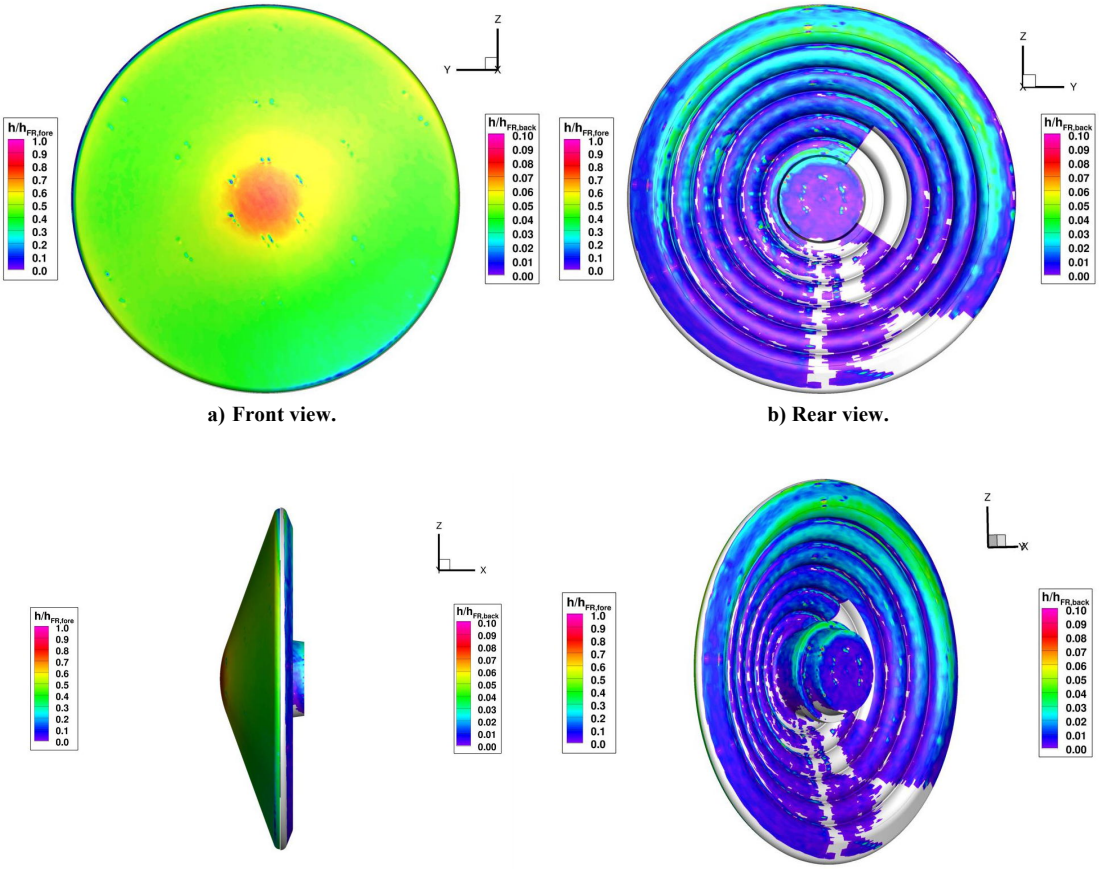


Figure 16. Schematic of Langley Research Center 20-Inch Mach 6 Air Tunnel.



a) Front view (Run 02). b) Rear view (Run 29).

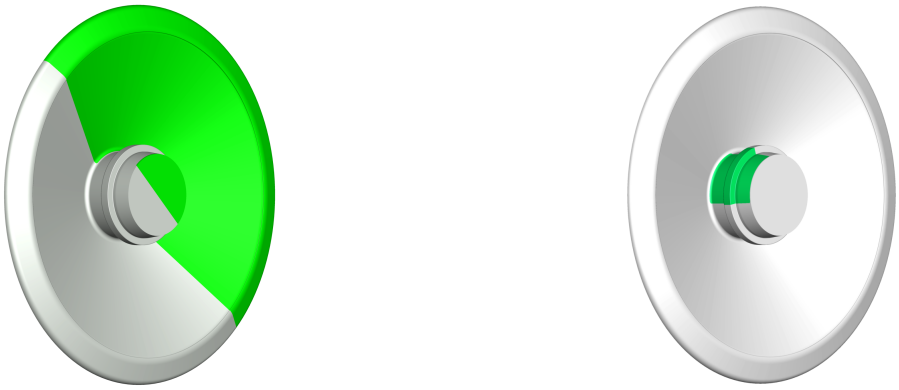
Figure 17. Sample phosphor thermography 2-D image data.



a) Front view. b) Rear view.

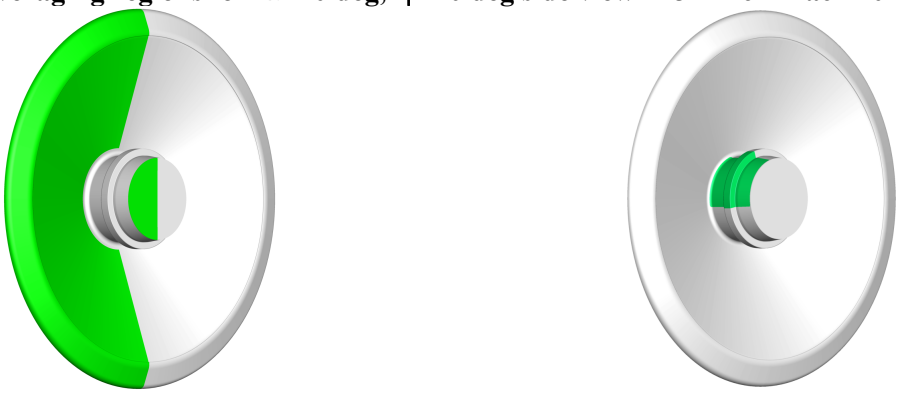
c) Side view. d) View in wind tunnel.

Figure 18. Sample 3-D mapping of phosphor thermography data.



a) Back side: θ = -45 deg to 135 deg. b) Payload: θ = -110 deg to 0 deg.

Figure 19. Averaging regions for α = 0 deg, ϕ = 0 deg side view in 31-Inch Mach 10 Air Tunnel.



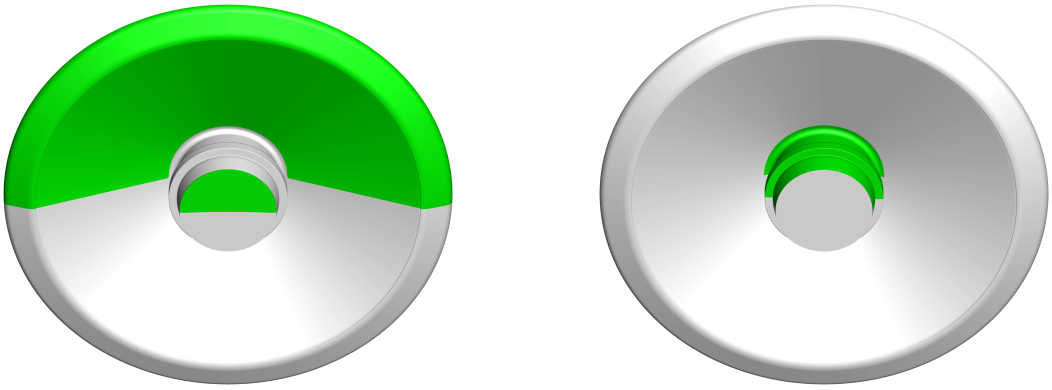
a) Back side: θ = 90 deg to 270 deg. b) Payload: θ = -110 deg to 0 deg.

Figure 20. Averaging regions for α = 0 deg, ϕ = 90 deg side view in 31-Inch Mach 10 Air Tunnel.



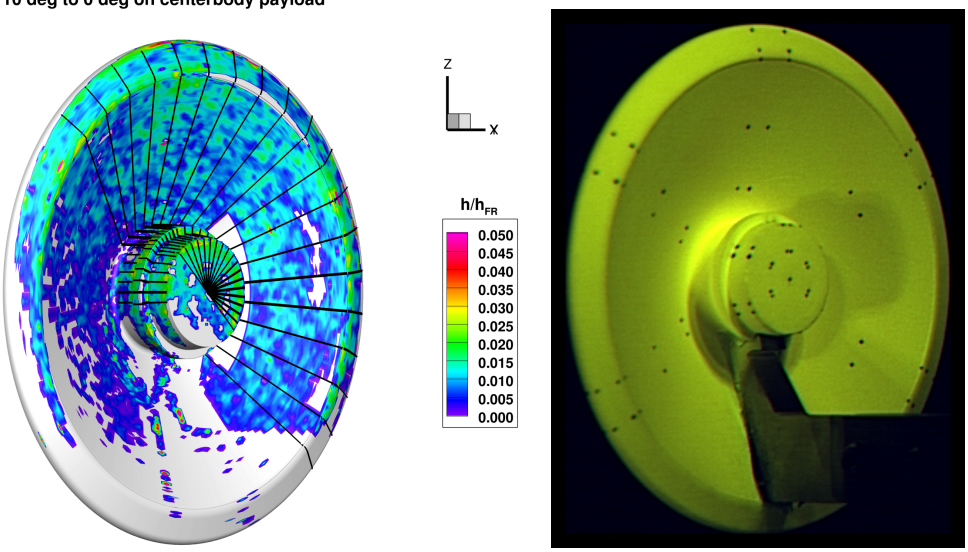
a) Back side: θ = 80 deg to 100 deg. b) Payload: (N/A)

Figure 21. Averaging regions for α =±5 deg , ϕ = 0 deg side view in 31-Inch Mach 10 Air Tunnel.



a) Back side: θ = 0 deg to 180 deg. b) Payload: θ = 0 deg to 180 deg.

Figure 22. Averaging regions for α =0 deg , ϕ = 0 deg top view in 20-Inch Mach 6 Air Tunnel.



a) Reduced and mapped heating data.

b) Intensity image.

Figure 23. Illustration of locations for extraction of data rays.

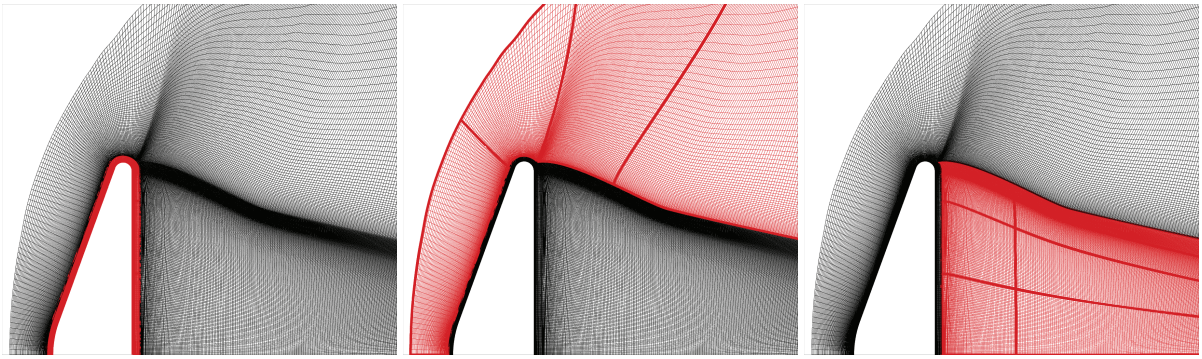


Figure 24. Stacked-block grid topology block types.

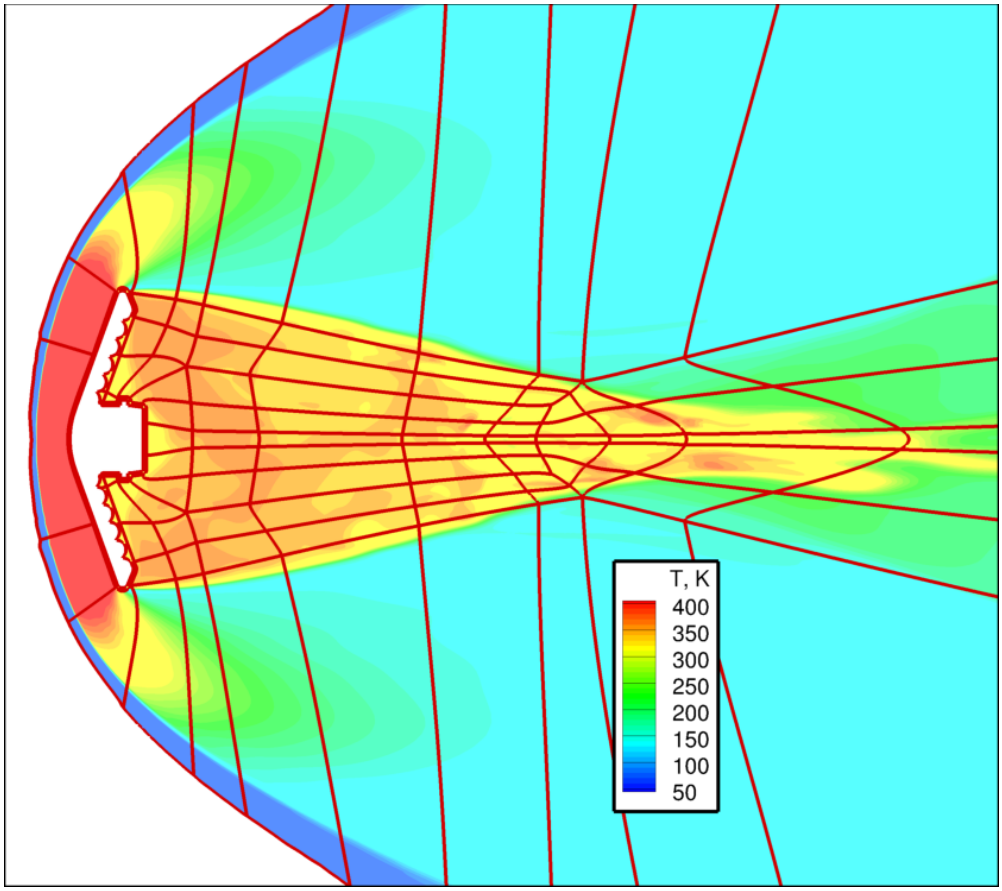
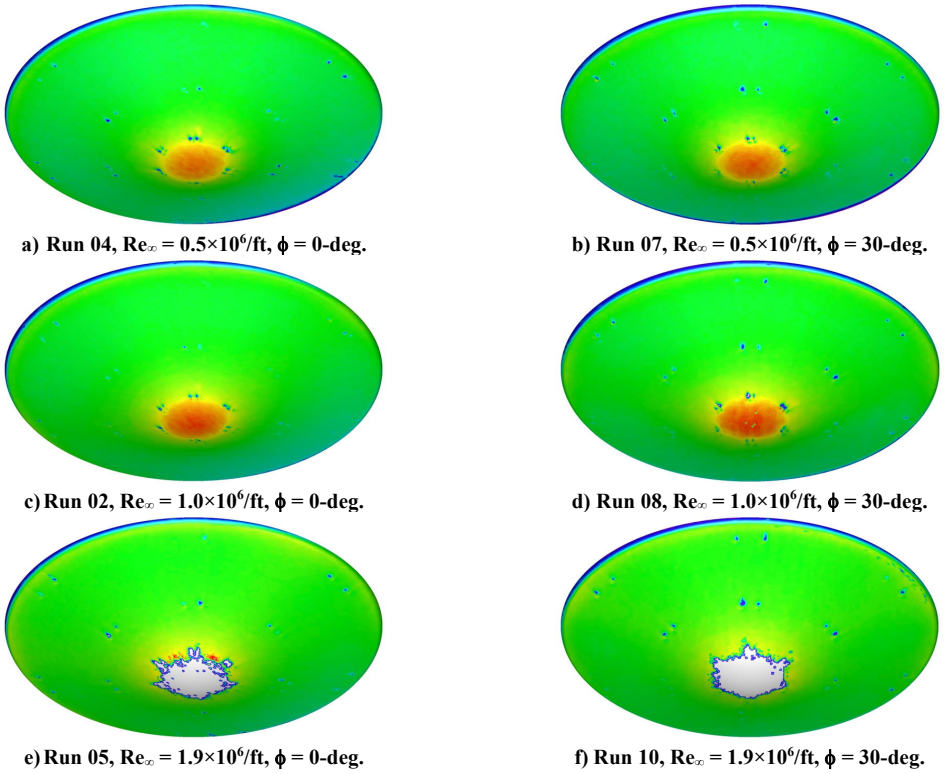


Figure 25. Stacked-block grid topology for LOFTID at wind tunnel conditions.



a) Run 04, $Re_\infty = 0.5\times10^6$/ft, ϕ = 0-deg.

b) Run 07, $Re_\infty = 0.5\times10^6$/ft, ϕ = 30-deg.

c) Run 02, $Re_\infty = 1.0\times10^6$/ft, ϕ = 0-deg.

d) Run 08, $Re_\infty = 1.0\times10^6$/ft, ϕ = 30-deg.

e) Run 05, $Re_\infty = 1.9\times10^6$/ft, ϕ = 0-deg.

f) Run 10, $Re_\infty = 1.9\times10^6$/ft, ϕ = 30-deg.

Figure 26. Aeroshell model A-0-S heating images at Mach 10, α = 0-deg.

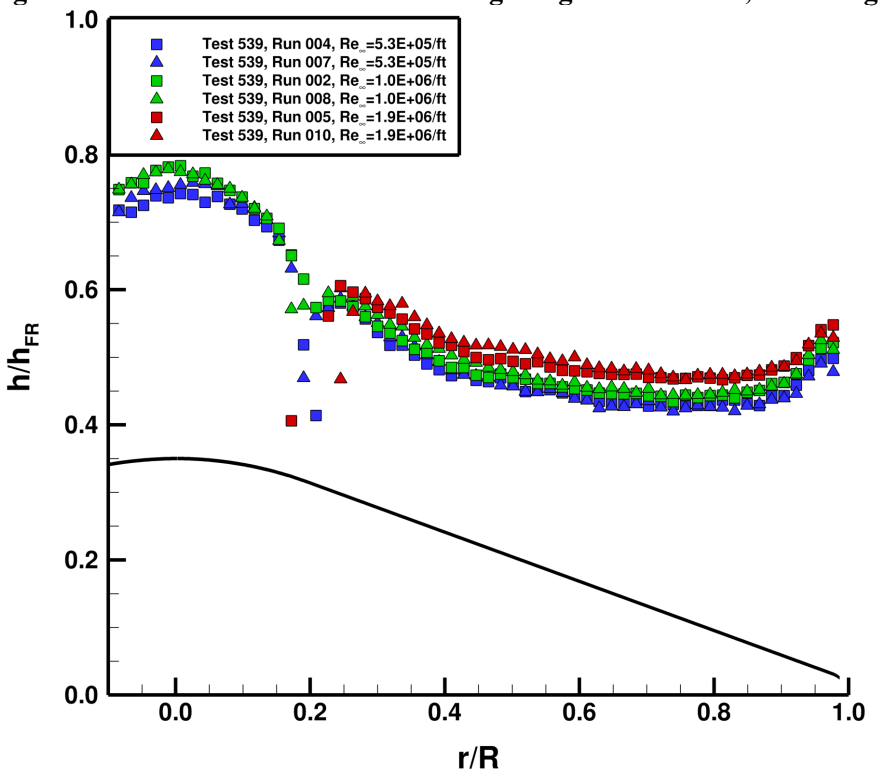
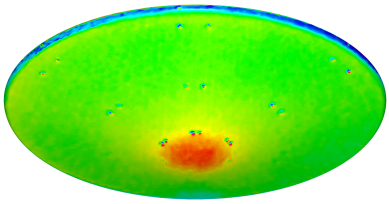
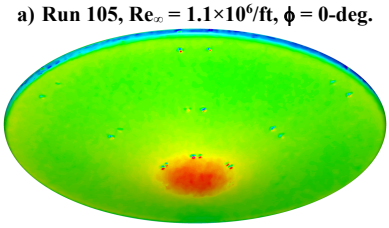


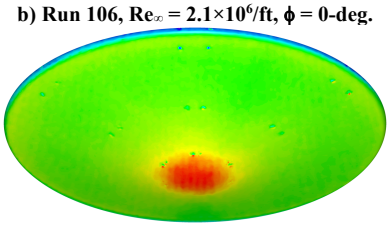
Figure 27. Aeroshell model A-0-S heating line plot at Mach 10, α = 0-deg.



a) Run 105, $Re_\infty = 1.1\times10^6$/ft, ϕ = 0-deg.



b) Run 106, $Re_\infty = 2.1\times10^6$/ft, ϕ = 0-deg.



c) Run 107, $Re_\infty = 3.0\times10^6$/ft, ϕ = 0-deg.

Figure 28. Aeroshell model A-0-S heating images at Mach 6, α = 0-deg.

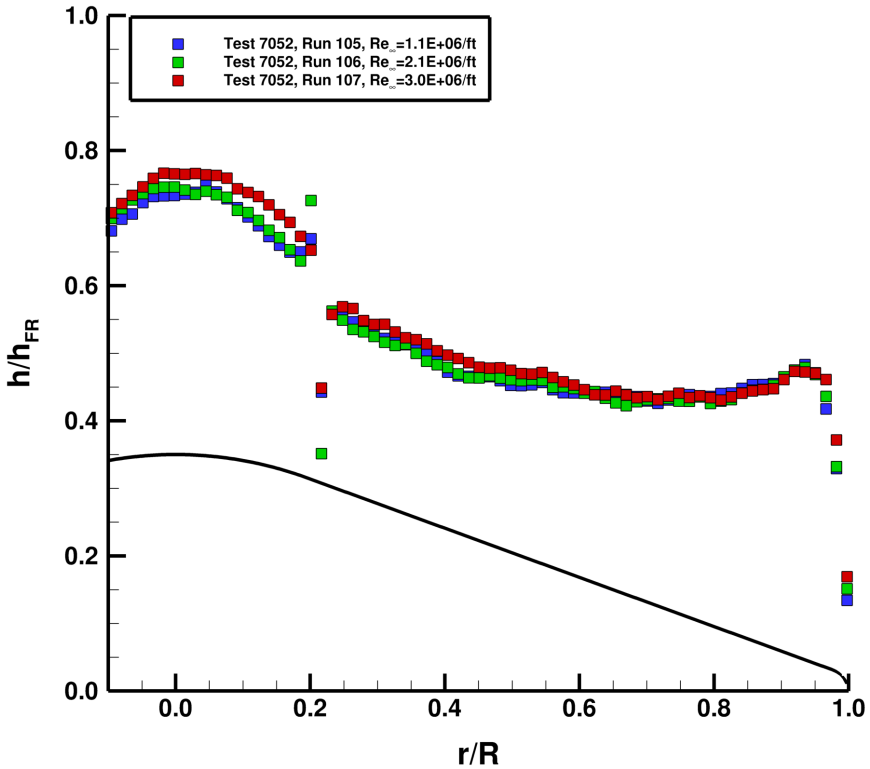
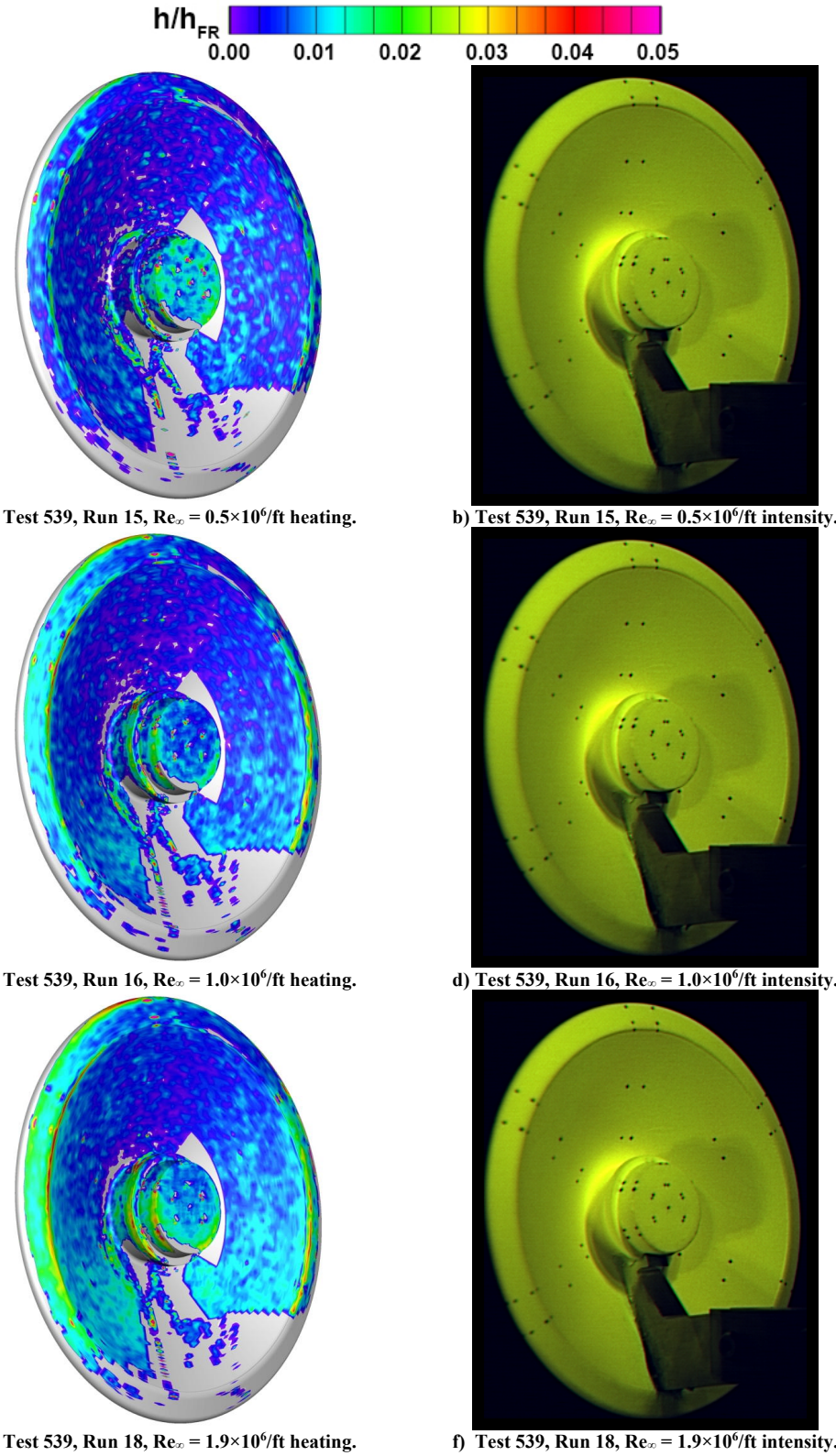


Figure 29. Aeroshell model A-0-S heating line plot at Mach 6, α = 0-deg.



a) Test 539, Run 15, $Re_\infty = 0.5\times10^6$/ft heating.

b) Test 539, Run 15, $Re_\infty = 0.5\times10^6$/ft intensity.

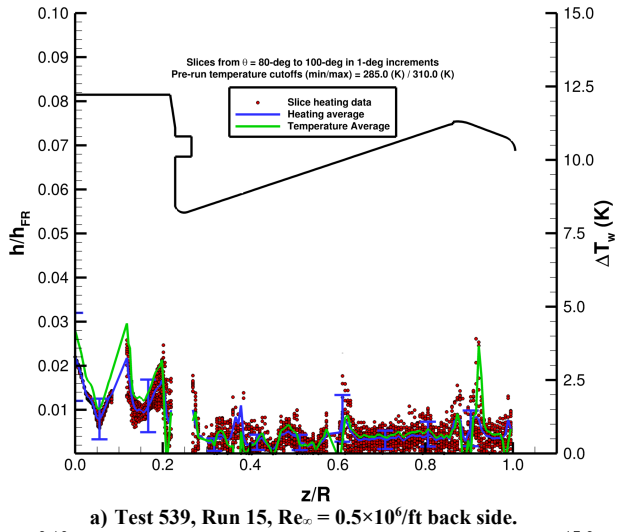
c) Test 539, Run 16, $Re_\infty = 1.0\times10^6$/ft heating.

d) Test 539, Run 16, $Re_\infty = 1.0\times10^6$/ft intensity.

e) Test 539, Run 18, $Re_\infty = 1.9\times10^6$/ft heating.

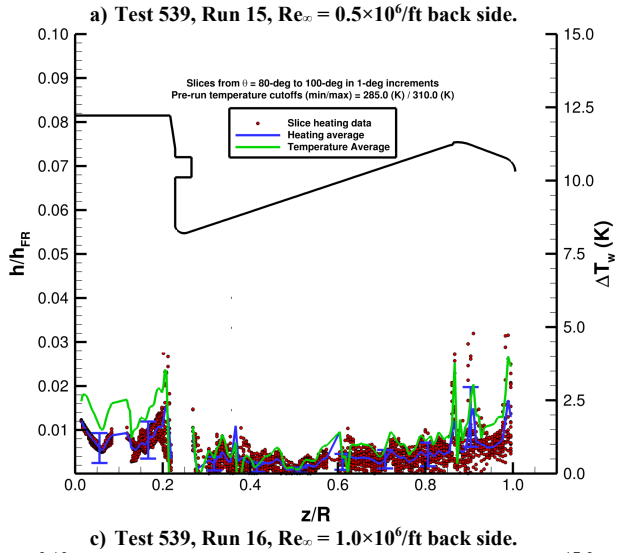
f) Test 539, Run 18, $Re_\infty = 1.9\times10^6$/ft intensity.

Figure 30. Smooth model S-1 back side images at Mach 10, α = -5 deg , ϕ = 0 deg.



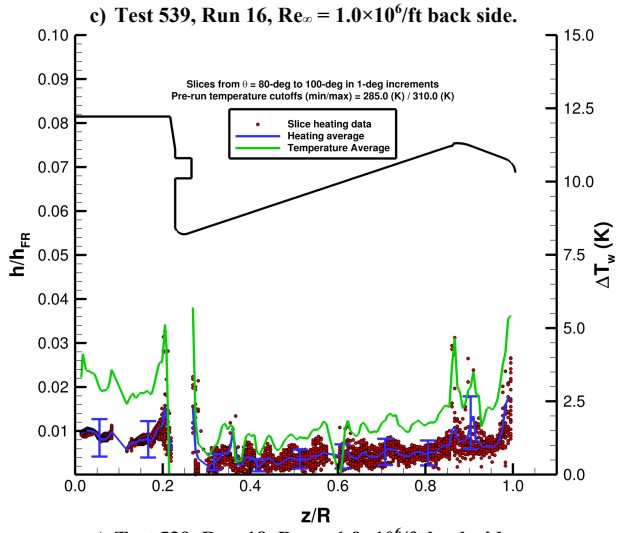
a) Test 539, Run 15, $Re_\infty = 0.5\times10^6$/ft back side.

b) Test 539, Run 15, $Re_\infty = 0.5\times10^6$/ft payload (view N/A).



c) Test 539, Run 16, $Re_\infty = 1.0\times10^6$/ft back side.

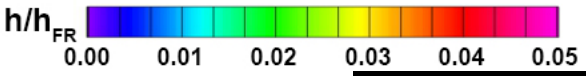
d) Test 539, Run 16, $Re_\infty = 1.0\times10^6$/ft payload (view N/A).

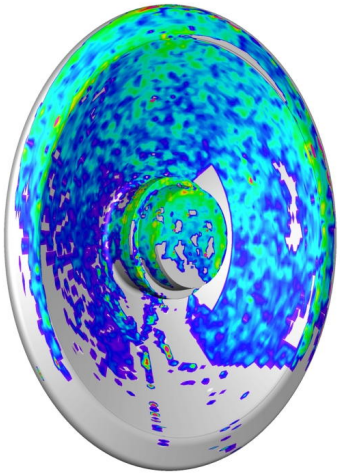


e) Test 539, Run 18, $Re_\infty = 1.9\times10^6$/ft back side.

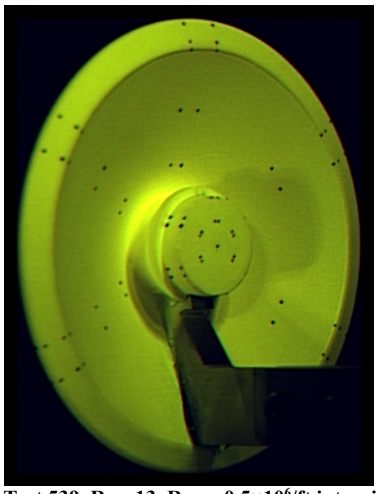
f) Test 539, Run 18, $Re_\infty = 1.9\times10^6$/ft payload (view N/A).

Figure 31. Smooth model S-1 back side plots at Mach 10, α = - 5 deg , ϕ = 0 deg.

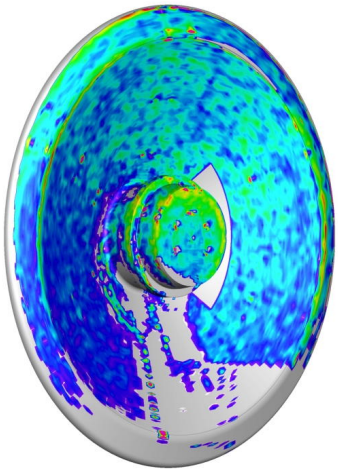




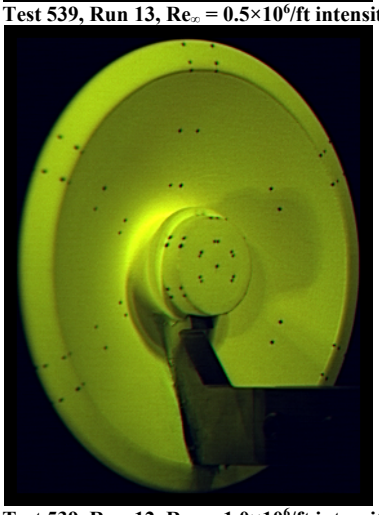
a) Test 539, Run 13, $Re_\infty = 0.5\times10^6$/ft heating.



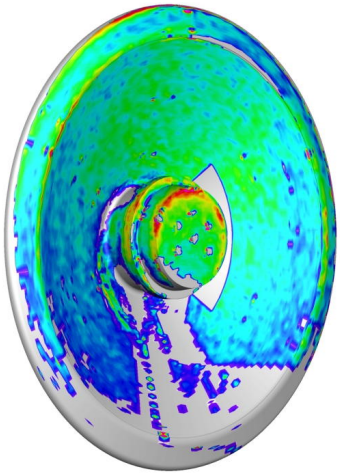
b) Test 539, Run 13, $Re_\infty = 0.5\times10^6$/ft intensity.



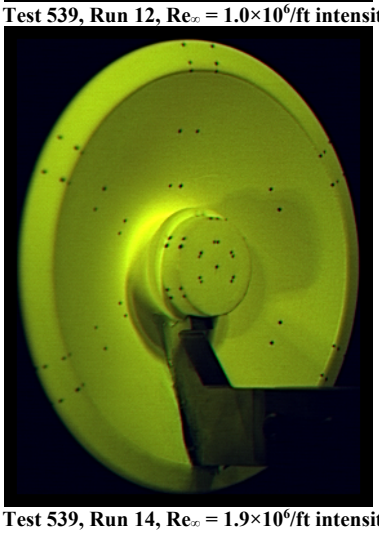
c) Test 539, Run 12, $Re_\infty = 1.0\times10^6$/ft heating.



d) Test 539, Run 12, $Re_\infty = 1.0\times10^6$/ft intensity.

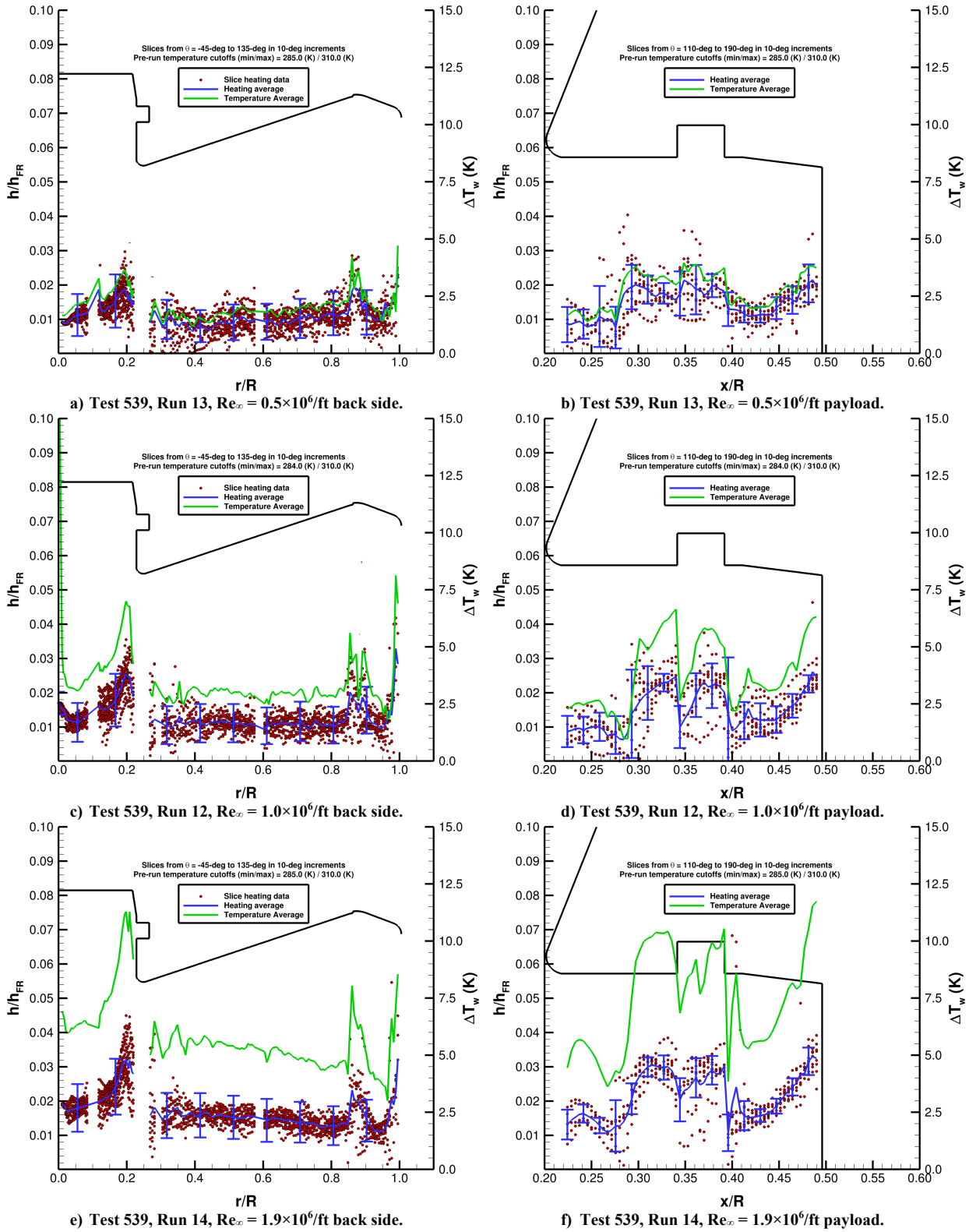


e) Test 539, Run 14, $Re_\infty = 1.9\times10^6$/ft heating.



f) Test 539, Run 14, $Re_\infty = 1.9\times10^6$/ft intensity.

Figure 32. Smooth model S-1 back side images at Mach 10, $\alpha = 0$ deg , $\phi = 0$ deg.



a) Test 539, Run 13, $Re_\infty = 0.5\times10^6$/ft back side.

b) Test 539, Run 13, $Re_\infty = 0.5\times10^6$/ft payload.

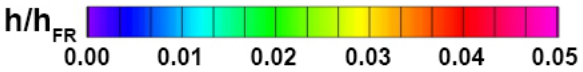
c) Test 539, Run 12, $Re_\infty = 1.0\times10^6$/ft back side.

d) Test 539, Run 12, $Re_\infty = 1.0\times10^6$/ft payload.

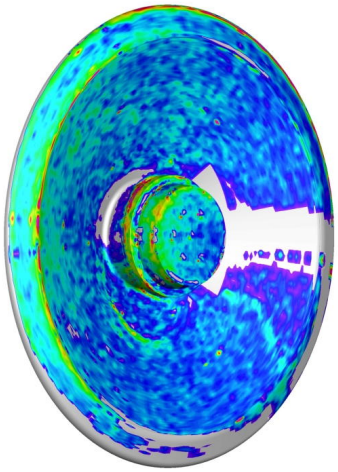
e) Test 539, Run 14, $Re_\infty = 1.9\times10^6$/ft back side.

f) Test 539, Run 14, $Re_\infty = 1.9\times10^6$/ft payload.

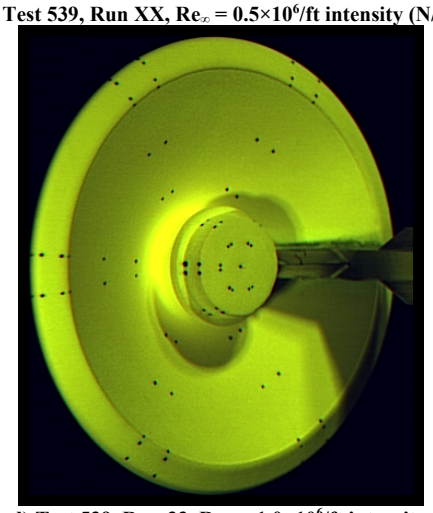
Figure 33. Smooth model S-1 back side plots at Mach 10, $\alpha = 0$ deg , $\phi = 0$ deg.



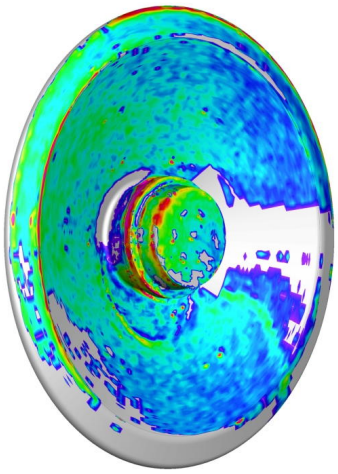
a) Test 539, Run XX, $Re_\infty = 0.5\times10^6$/ft heating (N/A).



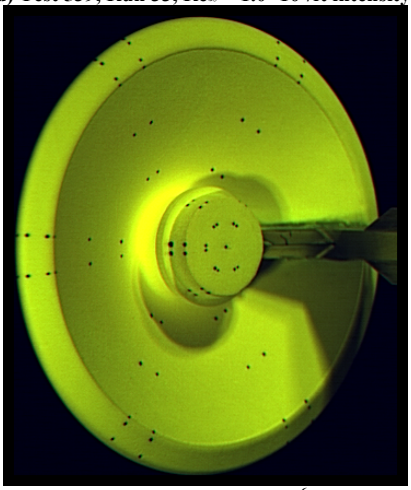
b) Test 539, Run XX, $Re_\infty = 0.5\times10^6$/ft intensity (N/A).



c) Test 539, Run 33, $Re_\infty = 1.0\times10^6$/ft heating.



d) Test 539, Run 33, $Re_\infty = 1.0\times10^6$/ft intensity.

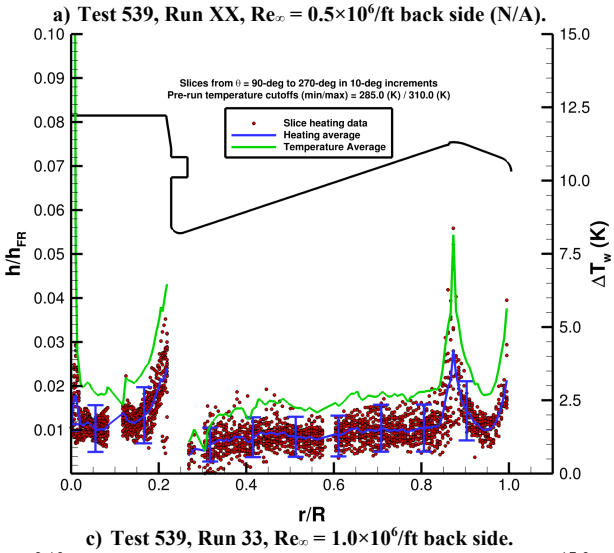


e) Test 539, Run 34, $Re_\infty = 1.9\times10^6$/ft heating.

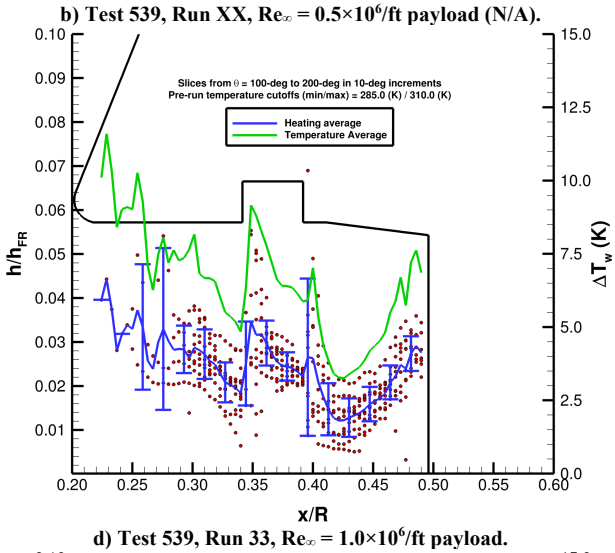
f) Test 539, Run 34, $Re_\infty = 1.9\times10^6$/ft intensity.

Figure 34. Smooth model S-1 back side images at Mach 10, $\alpha = 0$ deg , $\phi = 90$ deg.

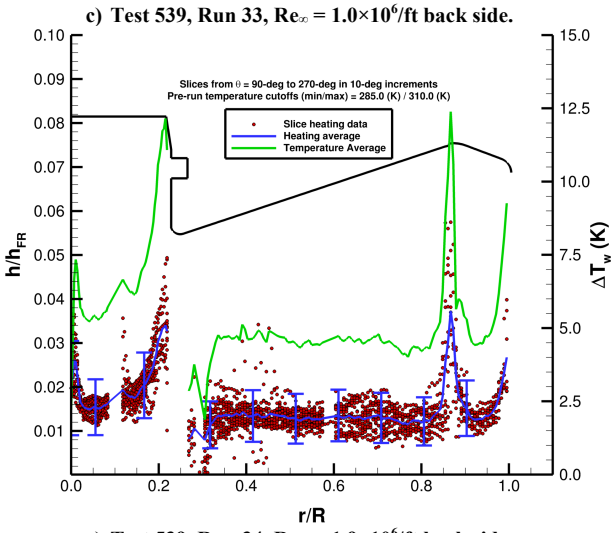
a) Test 539, Run XX, $Re_\infty = 0.5\times10^6$/ft back side (N/A).



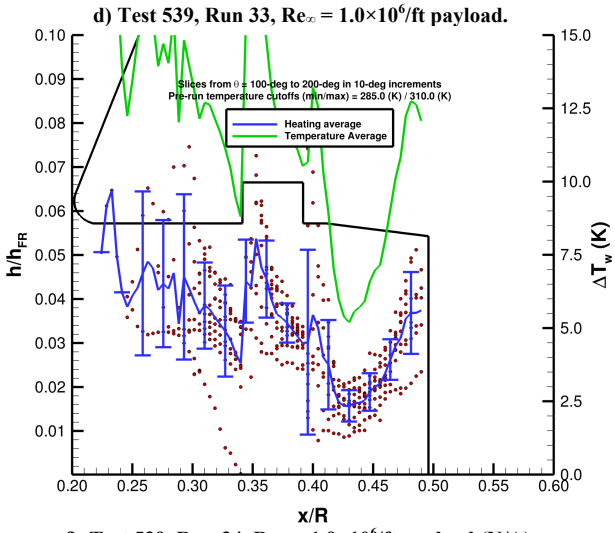
b) Test 539, Run XX, $Re_\infty = 0.5\times10^6$/ft payload (N/A).



c) Test 539, Run 33, $Re_\infty = 1.0\times10^6$/ft back side.



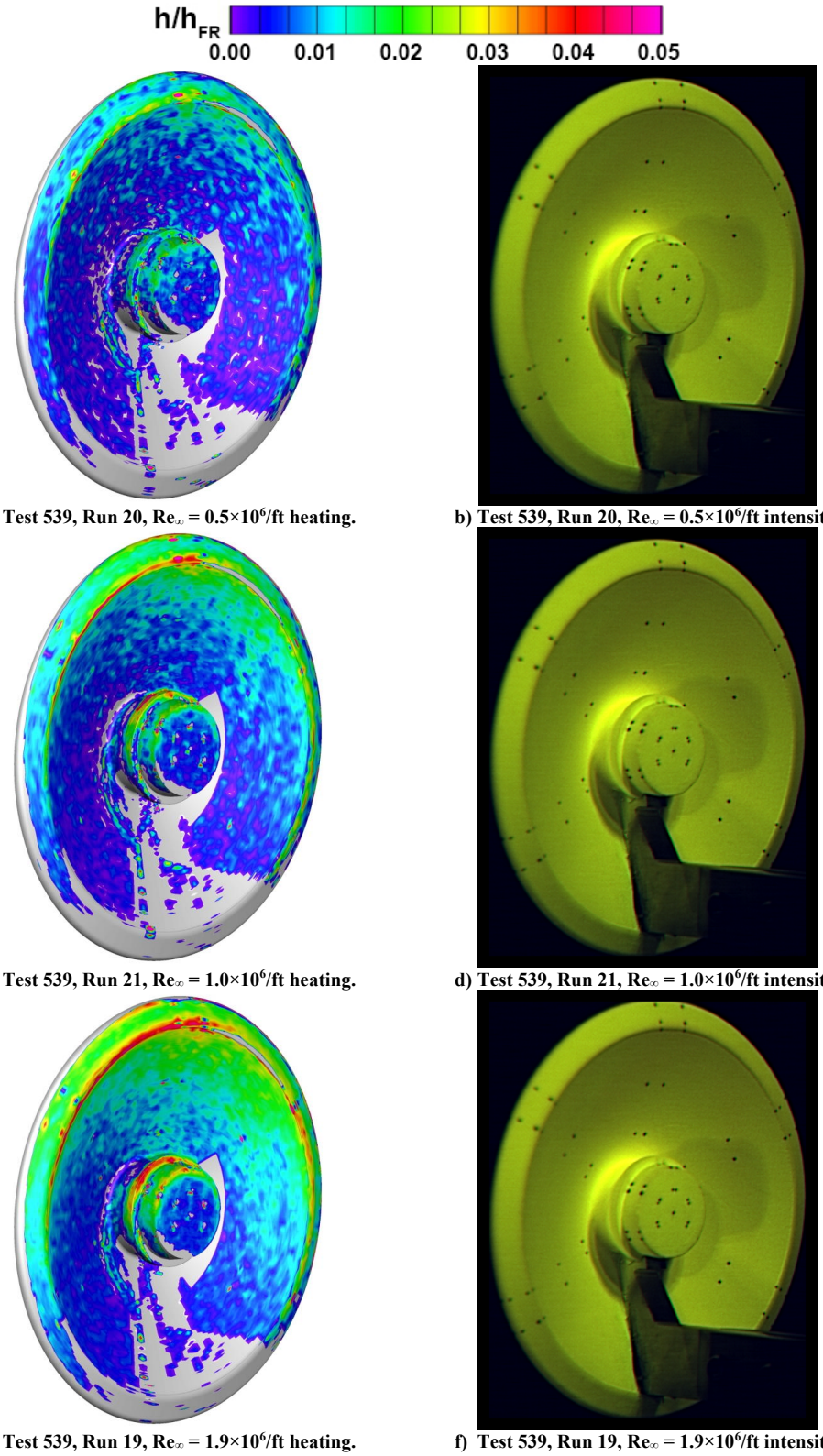
d) Test 539, Run 33, $Re_\infty = 1.0\times10^6$/ft payload.



e) Test 539, Run 34, $Re_\infty = 1.9\times10^6$/ft back side.

f) Test 539, Run 34, $Re_\infty = 1.9\times10^6$/ft payload (N/A).

Figure 35. Smooth model S-1 back side plots at Mach 10, $\alpha = 0$ deg , $\phi = 90$ deg.



a) Test 539, Run 20, $Re_\infty = 0.5\times10^6$/ft heating.

b) Test 539, Run 20, $Re_\infty = 0.5\times10^6$/ft intensity.

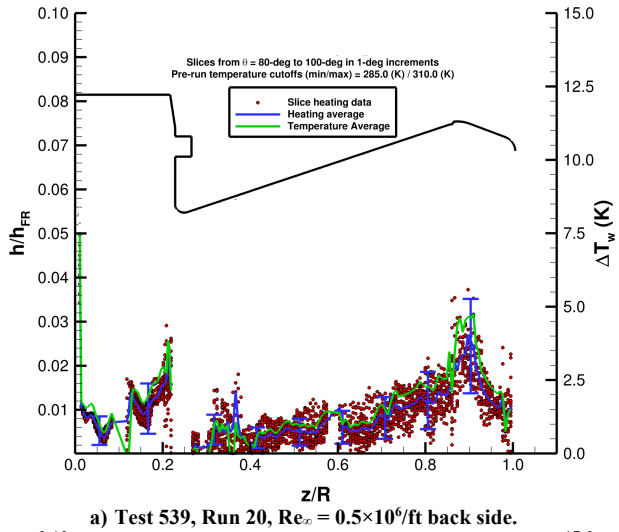
c) Test 539, Run 21, $Re_\infty = 1.0\times10^6$/ft heating.

d) Test 539, Run 21, $Re_\infty = 1.0\times10^6$/ft intensity.

e) Test 539, Run 19, $Re_\infty = 1.9\times10^6$/ft heating.

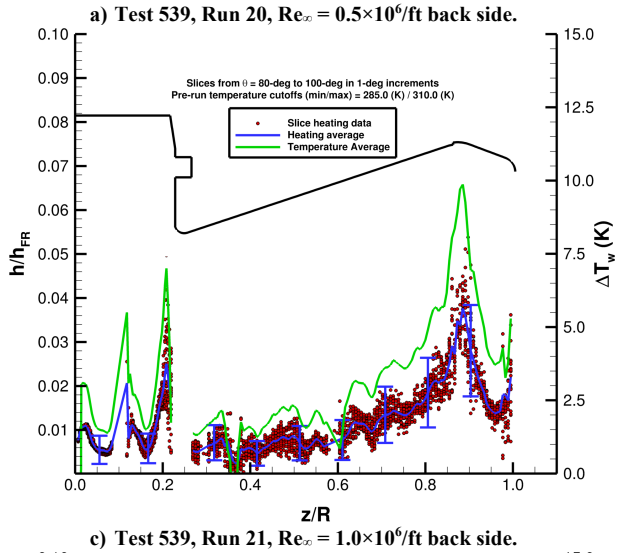
f) Test 539, Run 19, $Re_\infty = 1.9\times10^6$/ft intensity.

Figure 36. Smooth model S-1 back side images at Mach 10, α = +5 deg , ϕ = 0 deg.



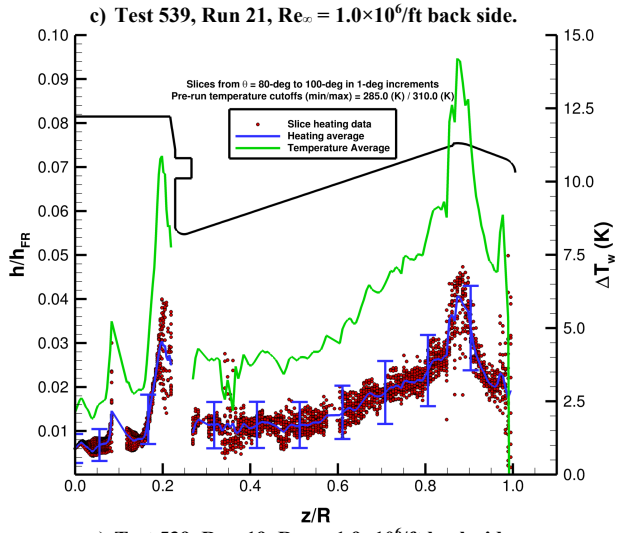
a) Test 539, Run 20, $Re_\infty = 0.5\times10^6$/ft back side.

b) Test 539, Run 20, $Re_\infty = 0.5\times10^6$/ft payload (view N/A).



c) Test 539, Run 21, $Re_\infty = 1.0\times10^6$/ft back side.

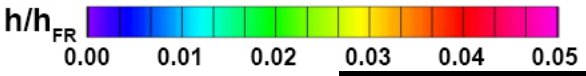
d) Test 539, Run 21, $Re_\infty = 1.0\times10^6$/ft payload (view N/A).

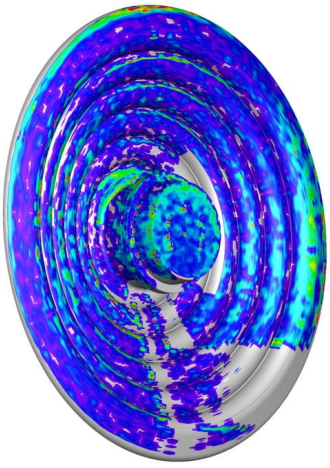


e) Test 539, Run 19, $Re_\infty = 1.9\times10^6$/ft back side.

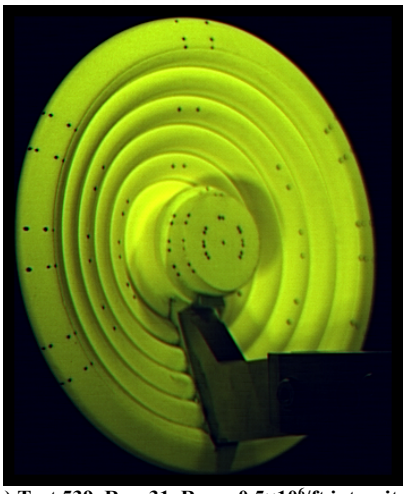
f) Test 539, Run 19, $Re_\infty = 1.9\times10^6$/ft payload (view N/A).

Figure 37. Smooth model S-1 back side plots at Mach 10, α = 5 deg , ϕ = 0 deg.

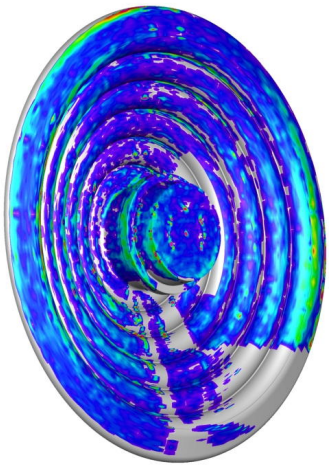




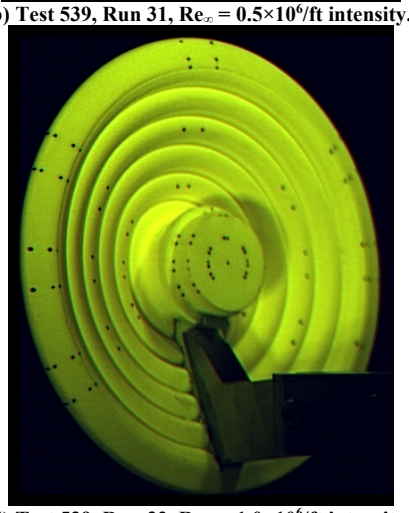
a) Test 539, Run 31, $Re_\infty = 0.5\times10^6$/ft heating.



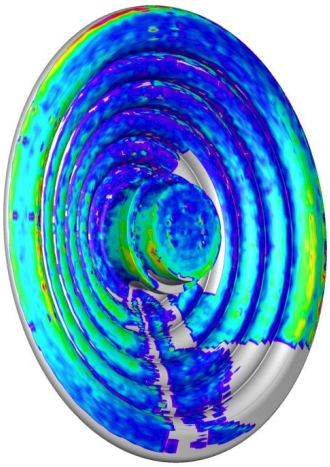
b) Test 539, Run 31, $Re_\infty = 0.5\times10^6$/ft intensity.



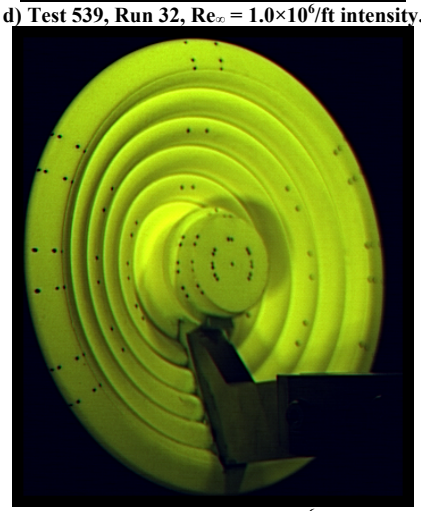
c) Test 539, Run 32, $Re_\infty = 1.0\times10^6$/ft heating.



d) Test 539, Run 32, $Re_\infty = 1.0\times10^6$/ft intensity.

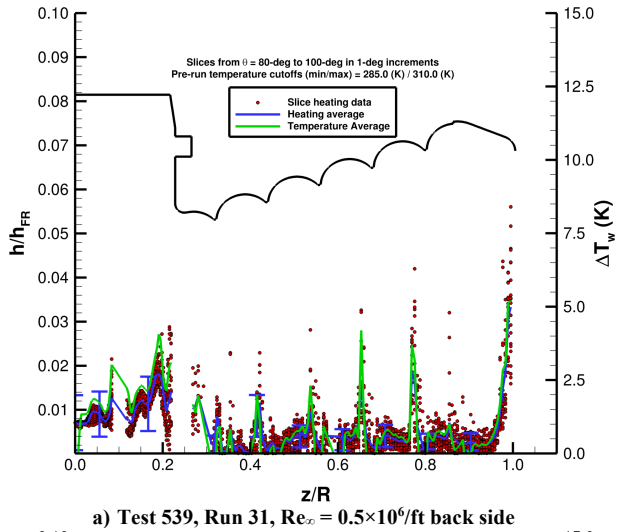


e) Test 539, Run 30, $Re_\infty = 1.9\times10^6$/ft heating.



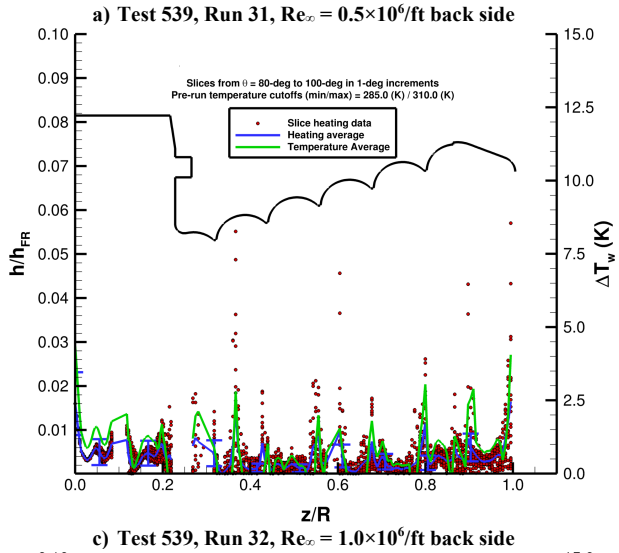
f) Test 539, Run 30, $Re_\infty = 1.9\times10^6$/ft intensity.

Figure 38. Toroid model T-1 back side images at Mach 10, α = -5 deg , ϕ = 0 deg.



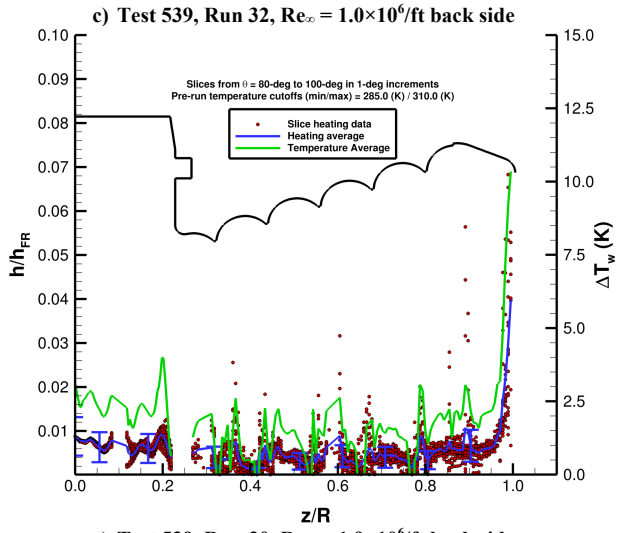
a) Test 539, Run 31, $Re_\infty = 0.5\times10^6$/ft back side

b) Test 539, Run 31, $Re_\infty = 0.5\times10^6$/ft payload (view N/A)



c) Test 539, Run 32, $Re_\infty = 1.0\times10^6$/ft back side

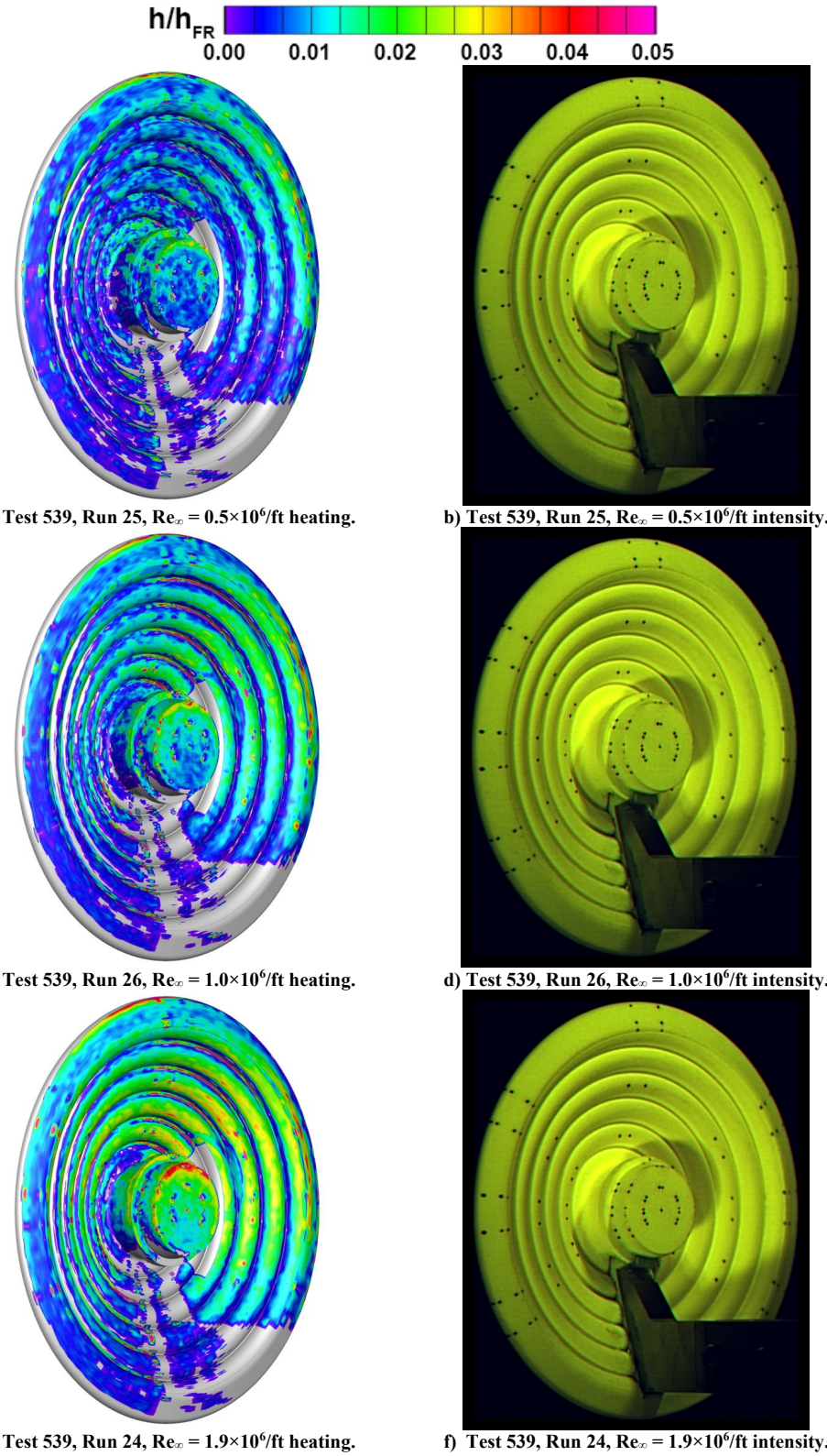
d) Test 539, Run 32, $Re_\infty = 1.0\times10^6$/ft payload (view NA)



e) Test 539, Run 30, $Re_\infty = 1.9\times10^6$/ft back side

Test 539, Run 30, $Re_\infty = 1.9\times10^6$/ft payload (view N/A)

Figure 39. Toroid model T-1 back side plots at Mach 10, α = 5 deg , ϕ = 0 deg.



a) Test 539, Run 25, $Re_\infty = 0.5\times10^6$/ft heating.

b) Test 539, Run 25, $Re_\infty = 0.5\times10^6$/ft intensity.

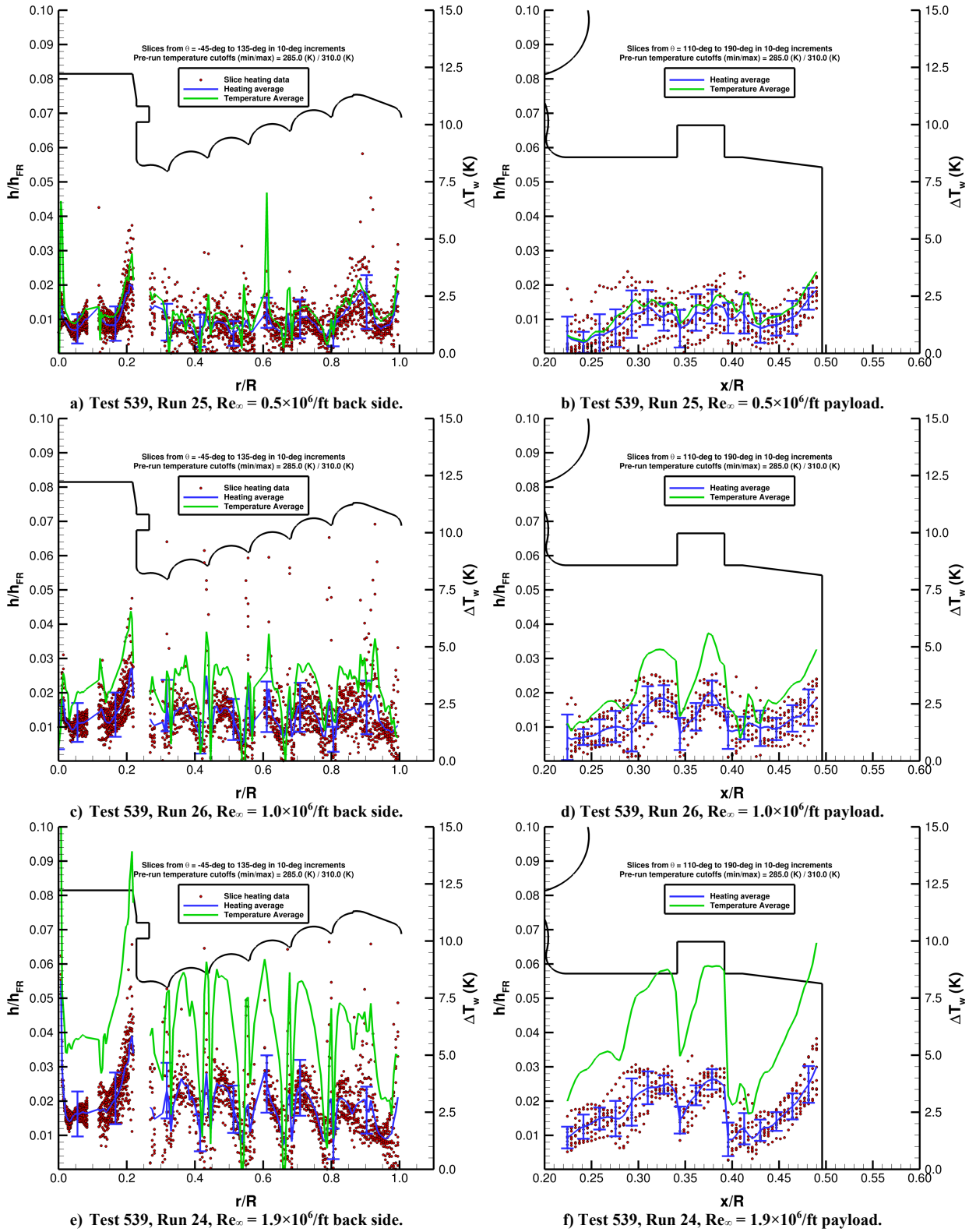
c) Test 539, Run 26, $Re_\infty = 1.0\times10^6$/ft heating.

d) Test 539, Run 26, $Re_\infty = 1.0\times10^6$/ft intensity.

e) Test 539, Run 24, $Re_\infty = 1.9\times10^6$/ft heating.

f) Test 539, Run 24, $Re_\infty = 1.9\times10^6$/ft intensity.

Figure 40. Toroid model T-1 back side images at Mach 10, $\alpha = 0$ deg , $\phi = 0$ deg.



a) Test 539, Run 25, $Re_\infty = 0.5\times10^6$/ft back side.

b) Test 539, Run 25, $Re_\infty = 0.5\times10^6$/ft payload.

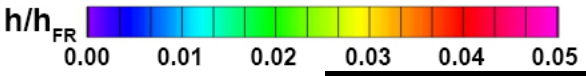
c) Test 539, Run 26, $Re_\infty = 1.0\times10^6$/ft back side.

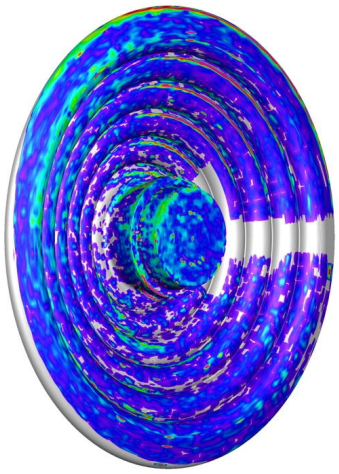
d) Test 539, Run 26, $Re_\infty = 1.0\times10^6$/ft payload.

e) Test 539, Run 24, $Re_\infty = 1.9\times10^6$/ft back side.

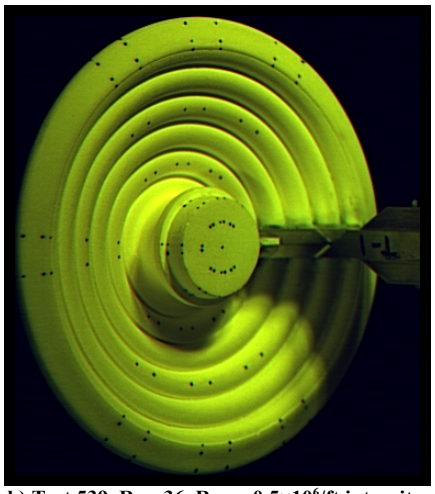
f) Test 539, Run 24, $Re_\infty = 1.9\times10^6$/ft payload.

Figure 41. Toroid model T-1 back side plots at Mach 10, $\alpha = 0$ deg , $\phi = 0$ deg.

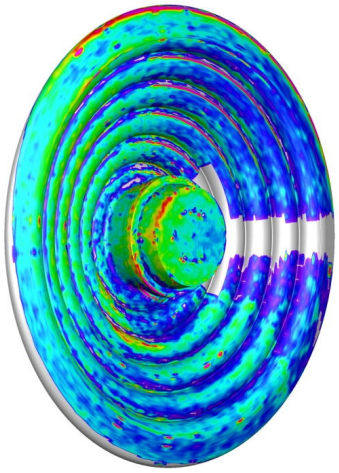




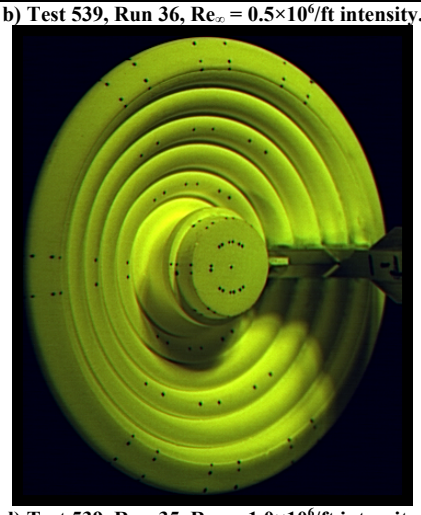
a) Test 539, Run 36, $Re_\infty = 0.5\times10^6$/ft heating.



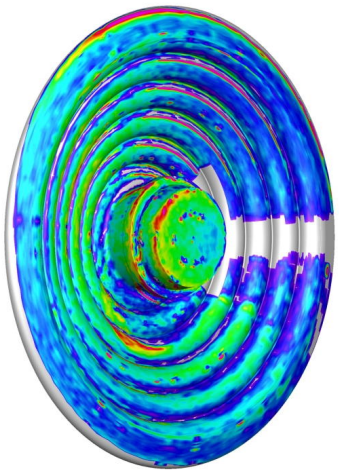
b) Test 539, Run 36, $Re_\infty = 0.5\times10^6$/ft intensity.



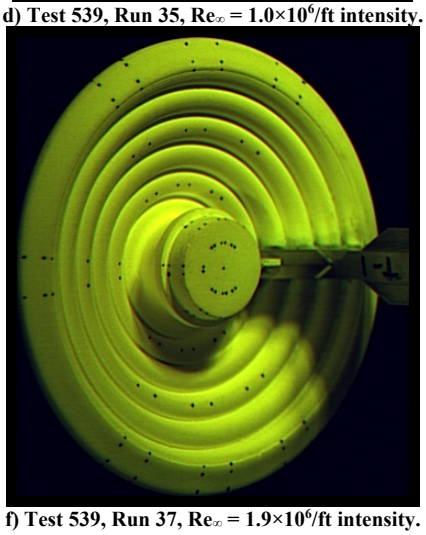
c) Test 539, Run 35, $Re_\infty = 1.0\times10^6$/ft heating.



d) Test 539, Run 35, $Re_\infty = 1.0\times10^6$/ft intensity.

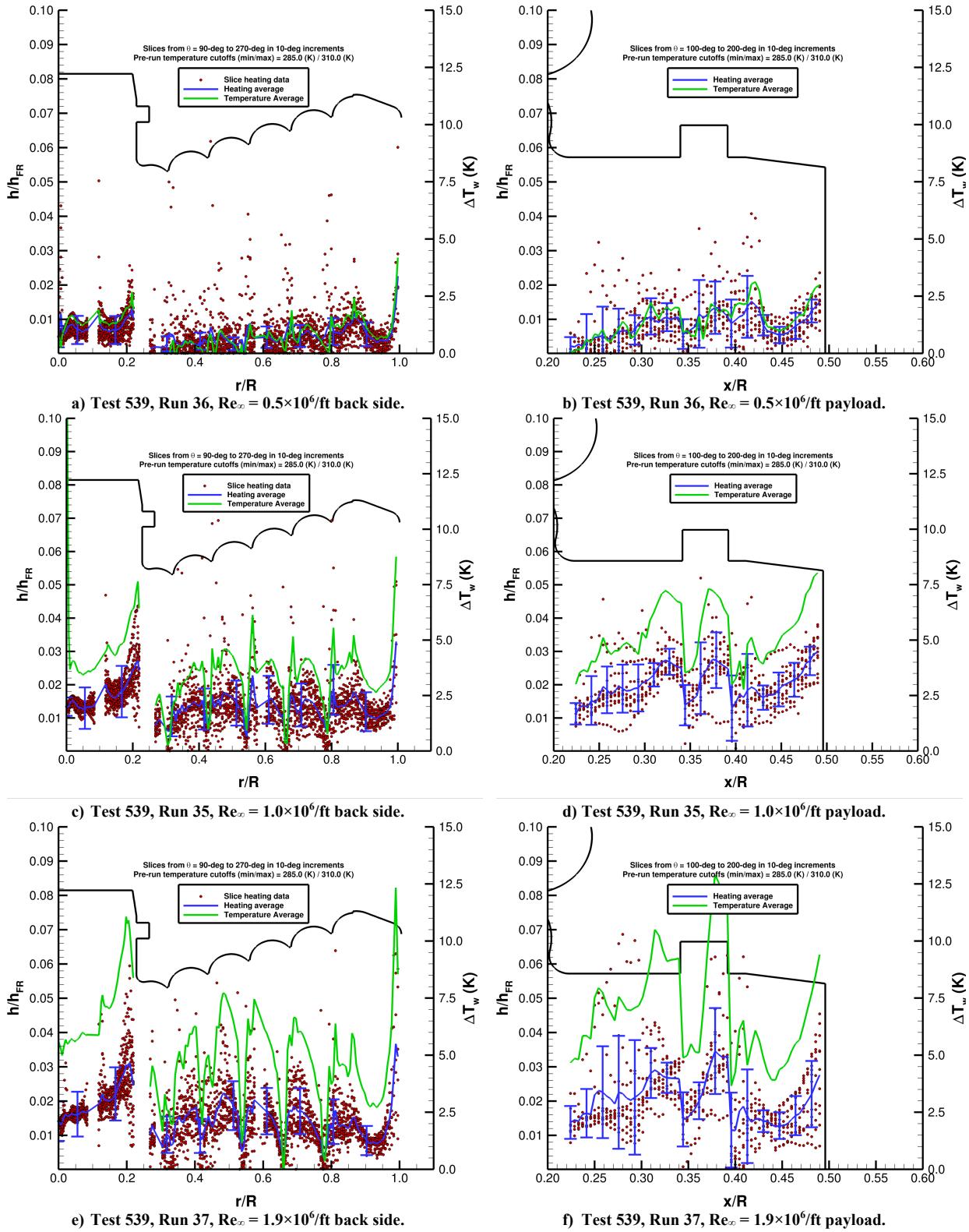


e) Test 539, Run 37, $Re_\infty = 1.9\times10^6$/ft heating.



f) Test 539, Run 37, $Re_\infty = 1.9\times10^6$/ft intensity.

Figure 42. Toroid model T-1 back side images at Mach 10, $\alpha = 0$ deg , $\phi = 90$ deg.



a) Test 539, Run 36, $Re_\infty = 0.5\times10^6$/ft back side.

b) Test 539, Run 36, $Re_\infty = 0.5\times10^6$/ft payload.

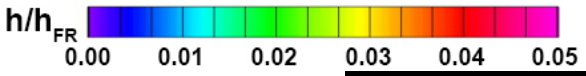
c) Test 539, Run 35, $Re_\infty = 1.0\times10^6$/ft back side.

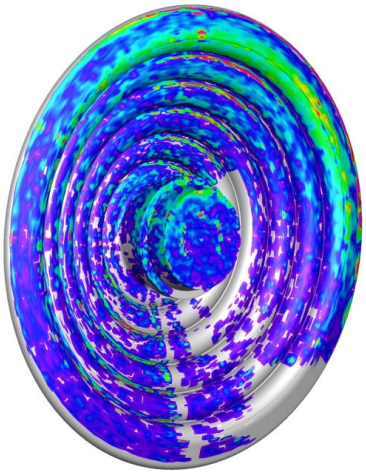
d) Test 539, Run 35, $Re_\infty = 1.0\times10^6$/ft payload.

e) Test 539, Run 37, $Re_\infty = 1.9\times10^6$/ft back side.

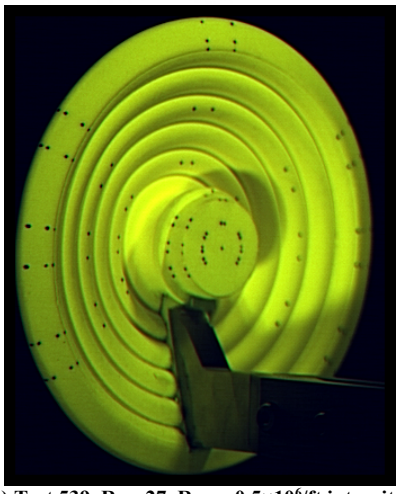
f) Test 539, Run 37, $Re_\infty = 1.9\times10^6$/ft payload.

Figure 43. Toroid mode T-1 back side plots at Mach 10, $\alpha = 0$ deg , $\phi = 90$ deg.

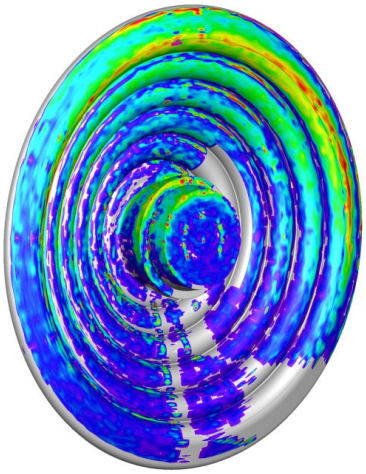




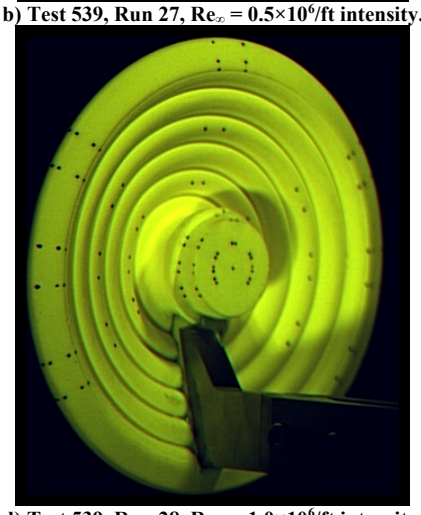
a) Test 539, Run 27, $Re_\infty = 0.5\times10^6$/ft heating.



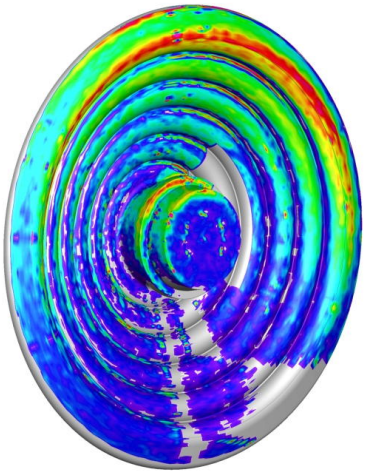
b) Test 539, Run 27, $Re_\infty = 0.5\times10^6$/ft intensity.



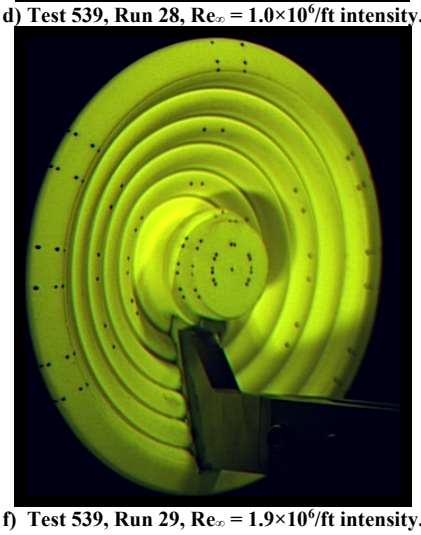
c) Test 539, Run 28, $Re_\infty = 1.0\times10^6$/ft heating.



d) Test 539, Run 28, $Re_\infty = 1.0\times10^6$/ft intensity.

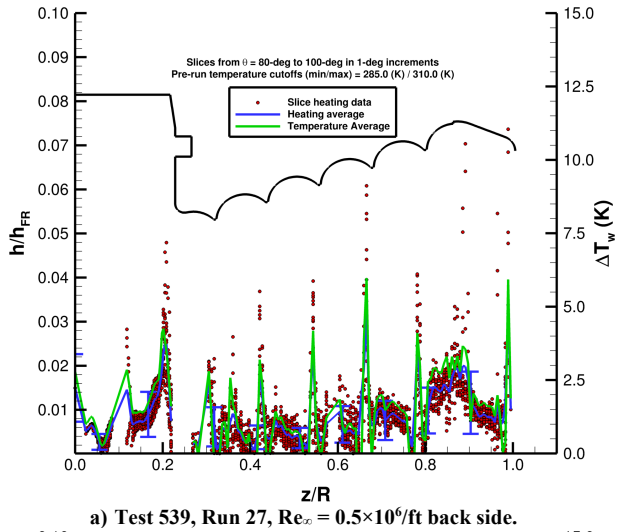


e) Test 539, Run 29, $Re_\infty = 1.9\times10^6$/ft heating.



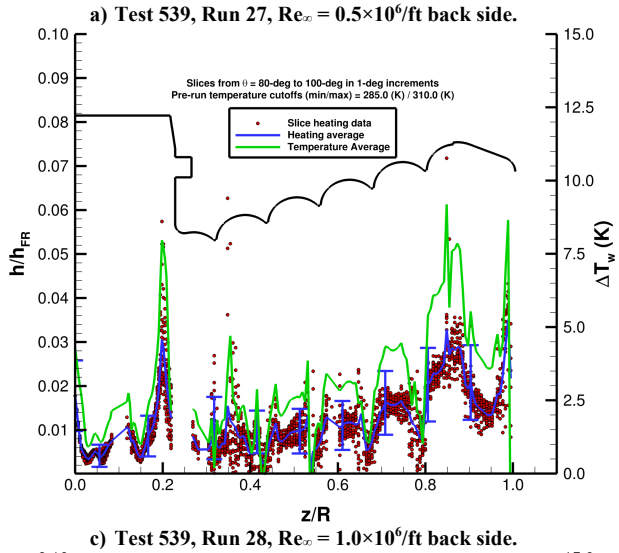
f) Test 539, Run 29, $Re_\infty = 1.9\times10^6$/ft intensity.

Figure 44. Toroid model T-1 back side images at Mach 10, α = +5 deg , ϕ = 0 deg.



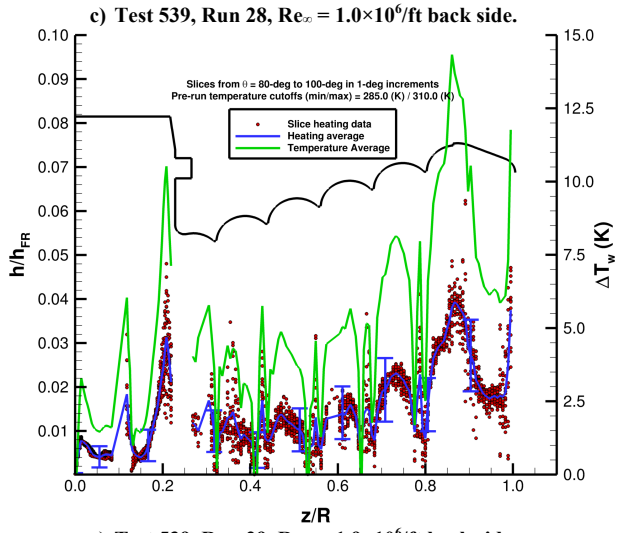
a) Test 539, Run 27, $Re_\infty = 0.5\times10^6$/ft back side.

b) Test 539, Run 27, $Re_\infty = 0.5\times10^6$/ft payload (view N/A).



c) Test 539, Run 28, $Re_\infty = 1.0\times10^6$/ft back side.

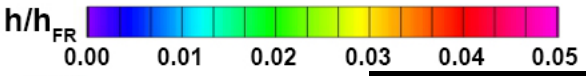
d) Test 539, Run 28, $Re_\infty = 1.0\times10^6$/ft payload (view N/A).

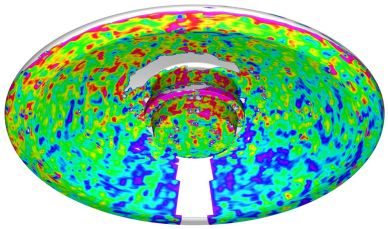


e) Test 539, Run 29, $Re_\infty = 1.9\times10^6$/ft back side.

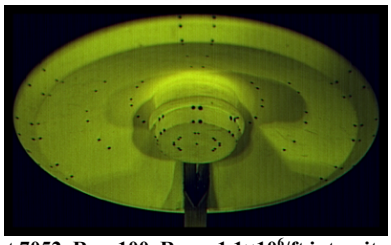
f) Test 539, Run 29, $Re_\infty = 1.9\times10^6$/ft payload (N/A).

Figure 45. Toroid model T-1 back side plots at Mach 10, α = +5 deg , ϕ = 0 deg.

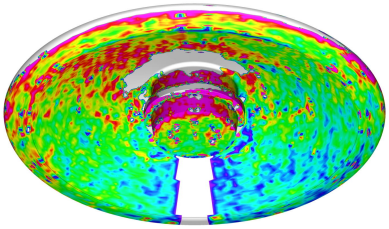




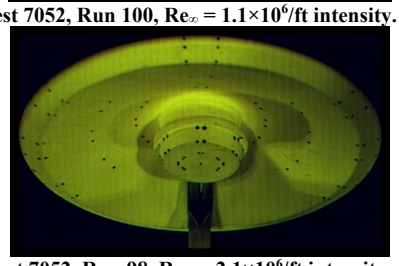
a) Test 7052, Run 100, $Re_\infty = 1.1\times10^6$/ft heating.



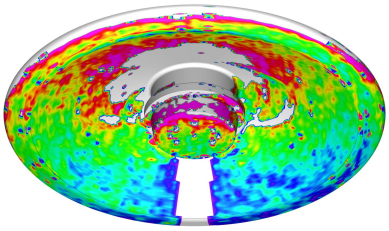
b) Test 7052, Run 100, $Re_\infty = 1.1\times10^6$/ft intensity.



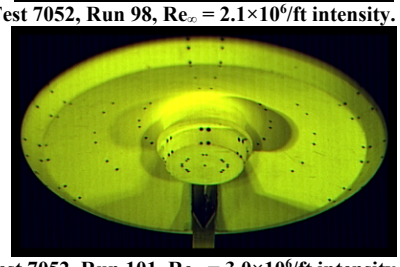
c) Test 7052, Run 98, $Re_\infty = 2.1\times10^6$/ft heating.



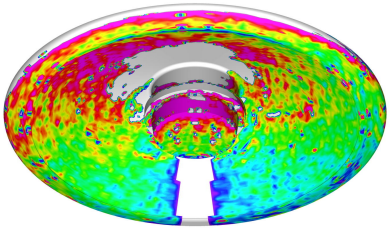
d) Test 7052, Run 98, $Re_\infty = 2.1\times10^6$/ft intensity.



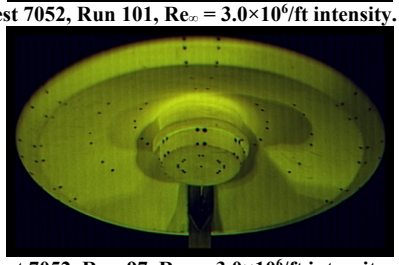
e) Test 7052, Run 101, $Re_\infty = 3.0\times10^6$/ft heating.



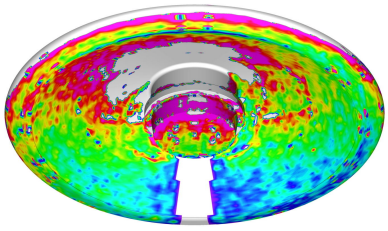
f) Test 7052, Run 101, $Re_\infty = 3.0\times10^6$/ft intensity.



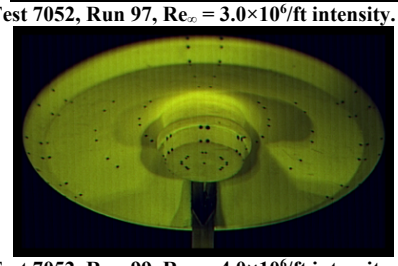
g) Test 7052, Run 97, $Re_\infty = 3.0\times10^6$/ft heating.



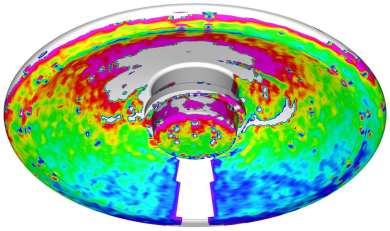
h) Test 7052, Run 97, $Re_\infty = 3.0\times10^6$/ft intensity.



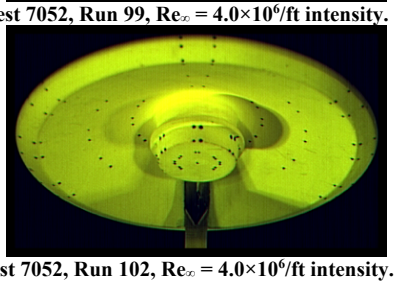
i) Test 7052, Run 99, $Re_\infty = 4.0\times10^6$/ft heating.



j) Test 7052, Run 99, $Re_\infty = 4.0\times10^6$/ft intensity.

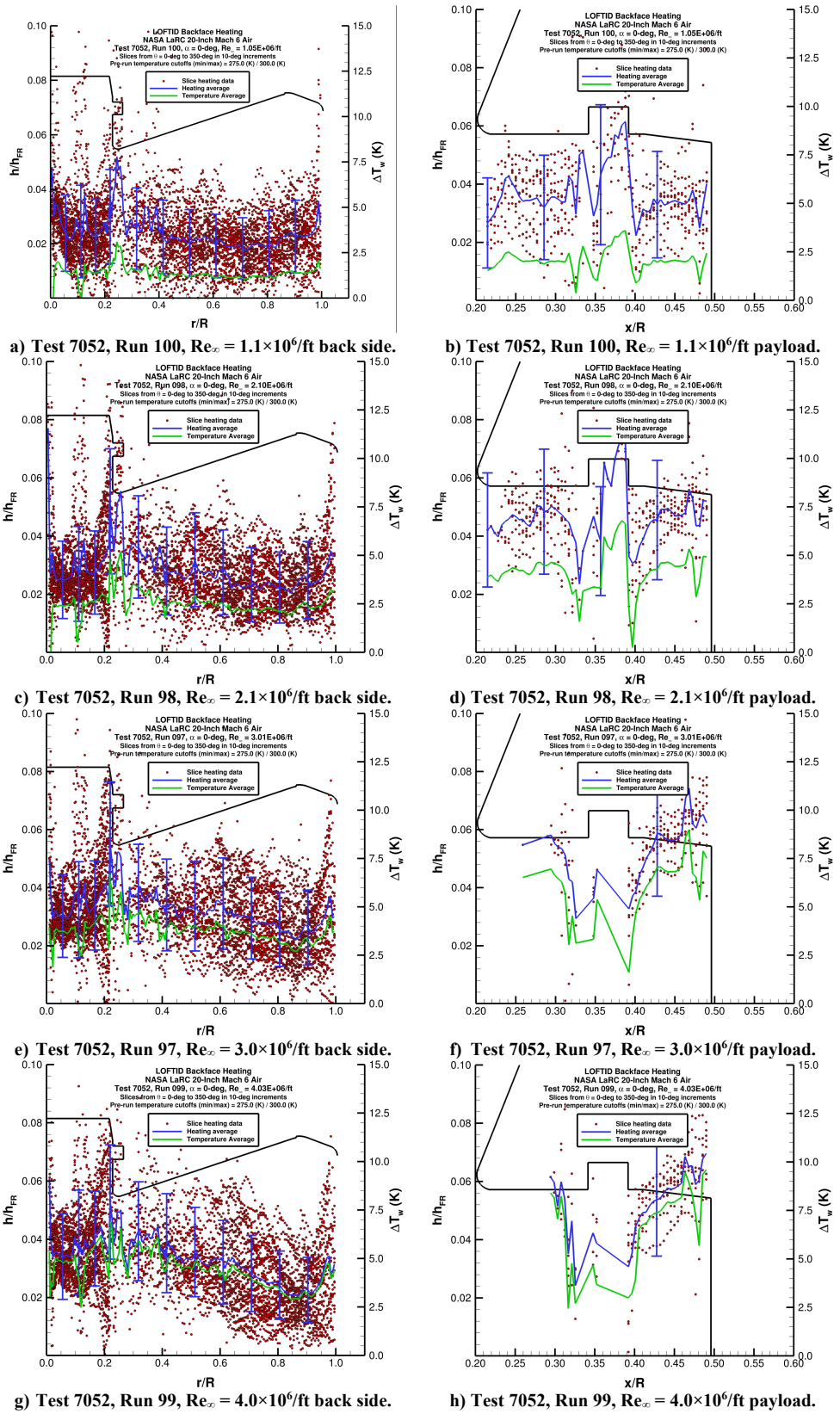


k) Test 7052, Run 102, $Re_\infty = 4.0\times10^6$/ft heating.



l) Test 7052, Run 102, $Re_\infty = 4.0\times10^6$/ft intensity.

Figure 46. Smooth model S-1 back side images at Mach 6, $\alpha = 0$ deg , $\phi = 0$ deg.



a) Test 7052, Run 100, $Re_\infty = 1.1\times10^6$/ft back side.

b) Test 7052, Run 100, $Re_\infty = 1.1\times10^6$/ft payload.

c) Test 7052, Run 98, $Re_\infty = 2.1\times10^6$/ft back side.

d) Test 7052, Run 98, $Re_\infty = 2.1\times10^6$/ft payload.

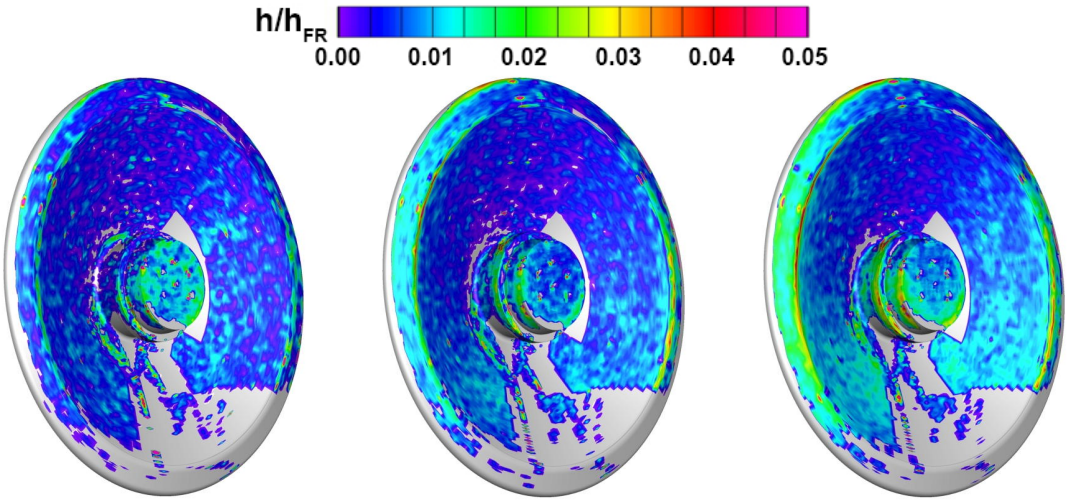
e) Test 7052, Run 97, $Re_\infty = 3.0\times10^6$/ft back side.

f) Test 7052, Run 97, $Re_\infty = 3.0\times10^6$/ft payload.

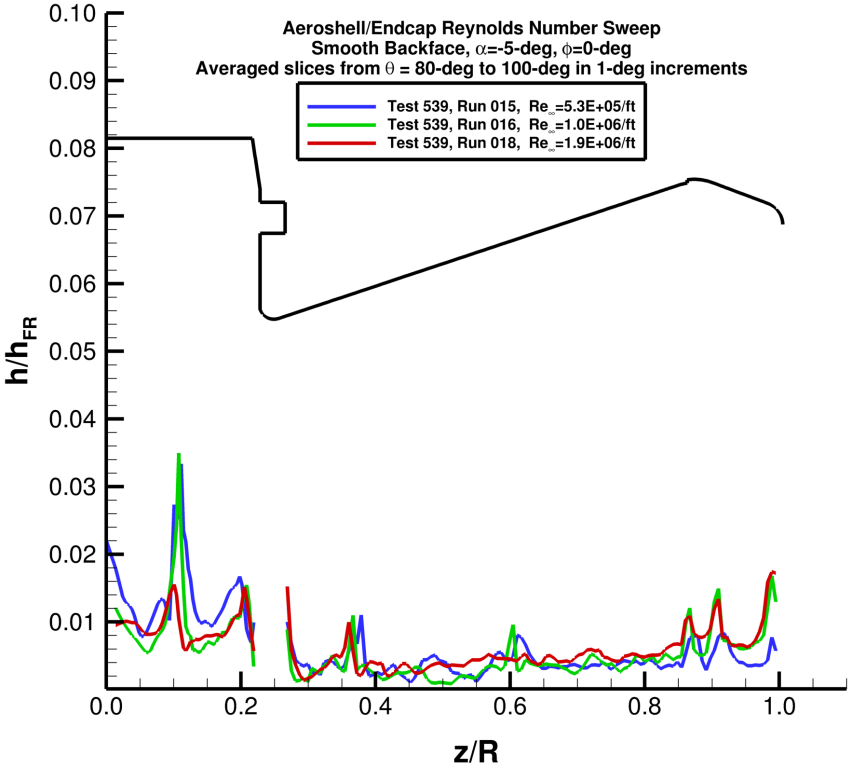
g) Test 7052, Run 99, $Re_\infty = 4.0\times10^6$/ft back side.

h) Test 7052, Run 99, $Re_\infty = 4.0\times10^6$/ft payload.

Figure 47. Smooth model S-1 back side plots at Mach 6, $\alpha = 0$ deg , $\phi = 0$ deg.

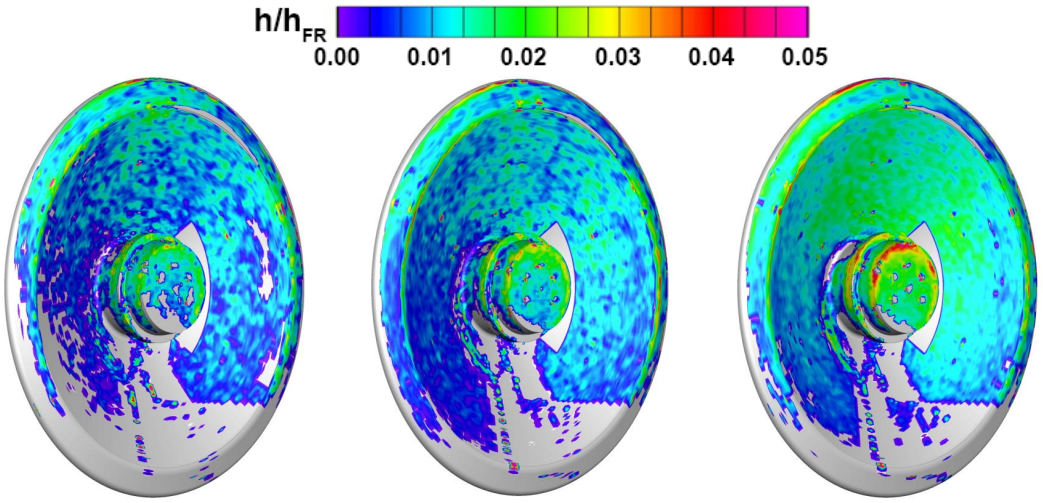


a) Test 539, Run 15, $Re_\infty = 0.5\times10^6$/ft. b) Test 539, Run 16, $Re_\infty = 1.0\times10^6$/ft. c) Test 539, Run 18, $Re_\infty = 1.9\times10^6$/ft.

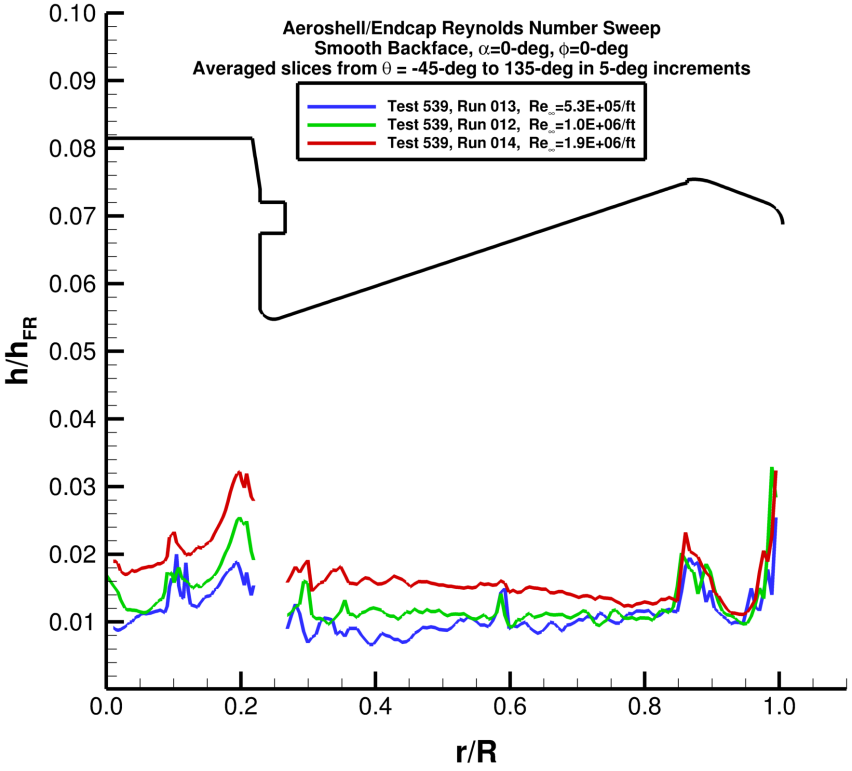


d) Symmetry plane data.

Figure 48. Smooth model S-1: Reynolds number effects at Mach 10, α = -5 deg, ϕ = 0 deg.

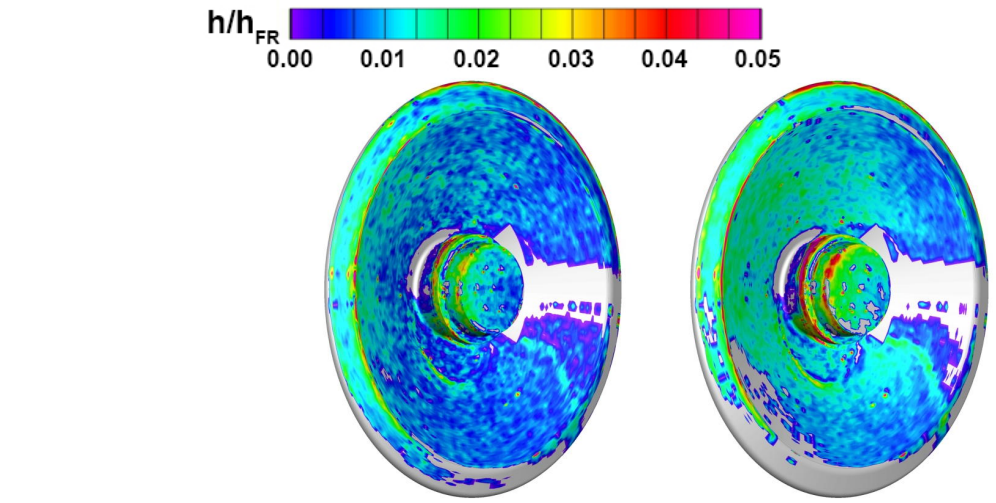


a) Test 539, Run 13, $Re_\infty = 0.5\times10^6$/ft. b) Test 539, Run 12, $Re_\infty = 1.0\times10^6$/ft. c) Test 539, Run 14, $Re_\infty = 1.9\times10^6$/ft.

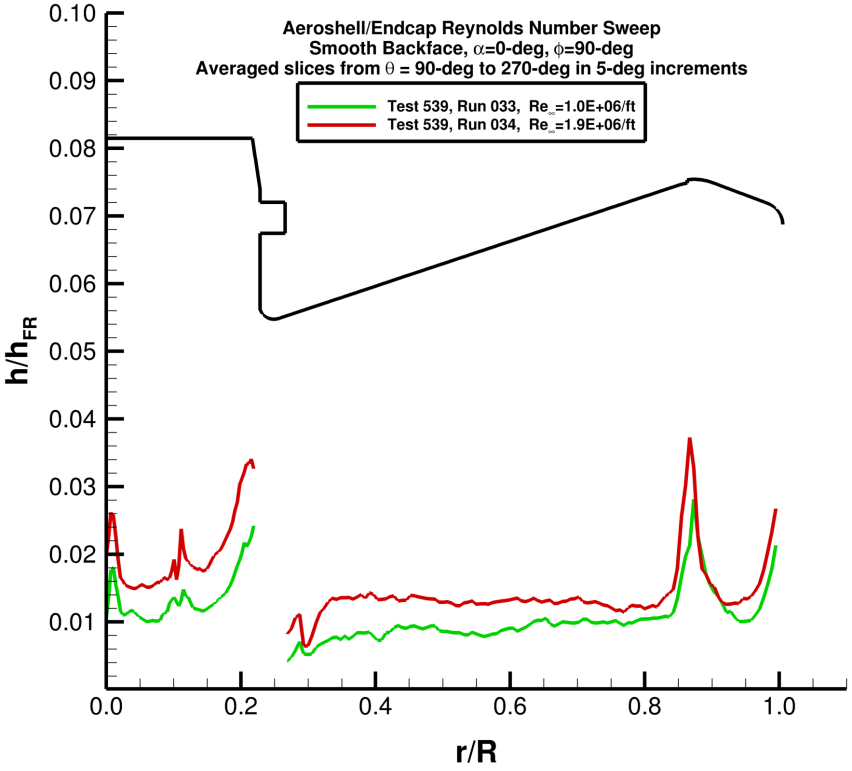


d) Symmetry plane data

Figure 49. Smooth model S-1: Re_∞ effects at Mach 10, α = 0 deg, ϕ = 0 deg.

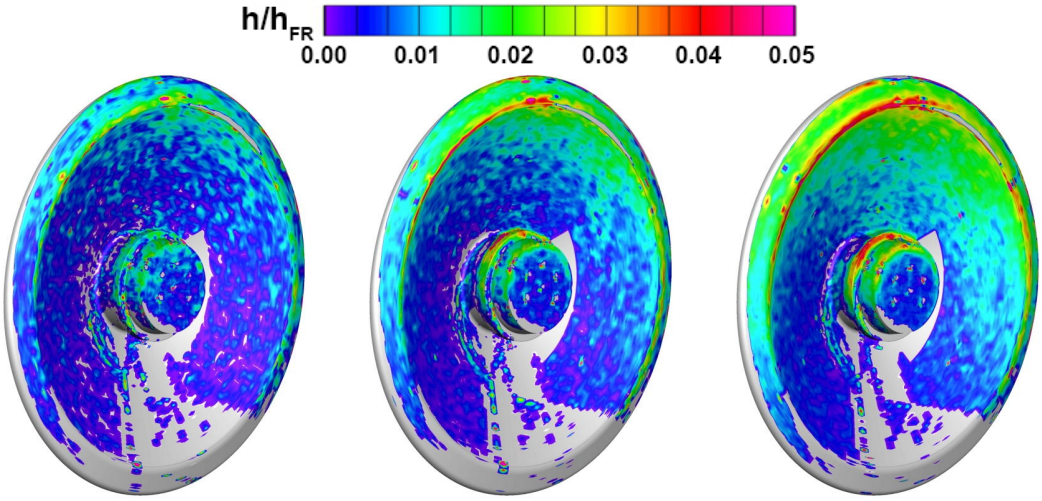


a) $Re_\infty = 0.5\times10^6$/ft (N/A). b) Test 539, Run 33, $Re_\infty = 1.0\times10^6$/ft. c) Test 539, Run 34, $Re_\infty = 1.9\times10^6$/ft.

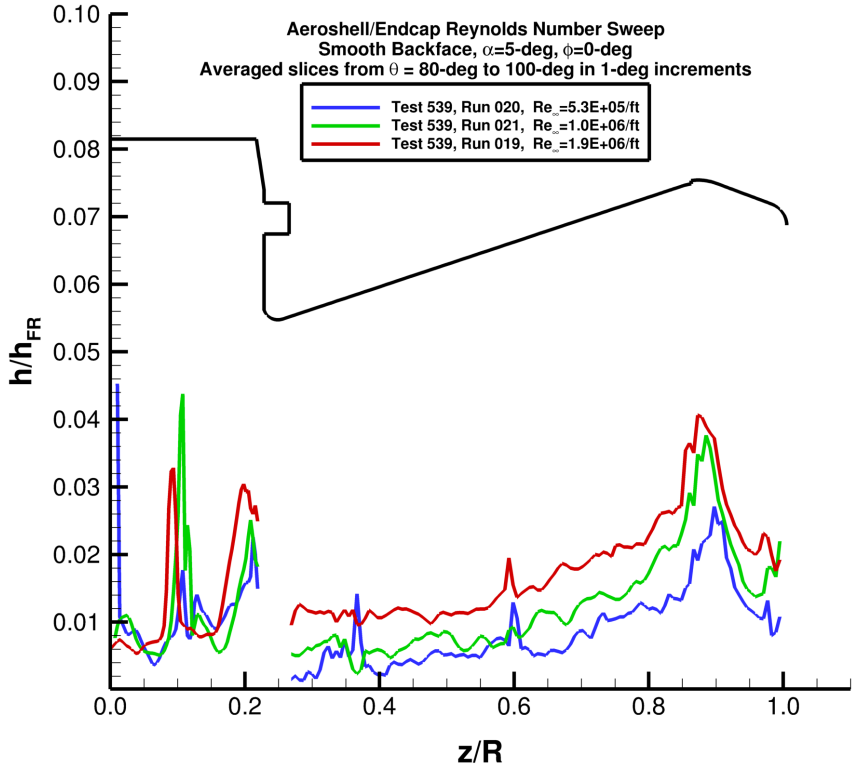


d) Symmetry plane data.

Figure 50. Smooth model S-1: Re_∞ effects at Mach 10, α = 0 deg, ϕ = 0 deg.

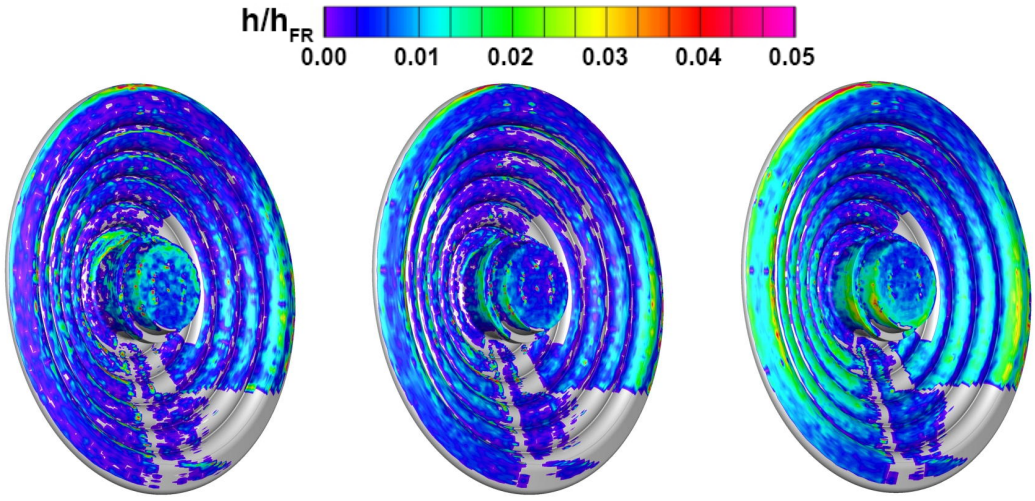


a) Test 539, Run 20, $Re_\infty = 0.5\times10^6$/ft. b) Test 539, Run 21, $Re_\infty = 1.0\times10^6$/ft. c) Test 539, Run 19, $Re_\infty = 1.9\times10^6$/ft.

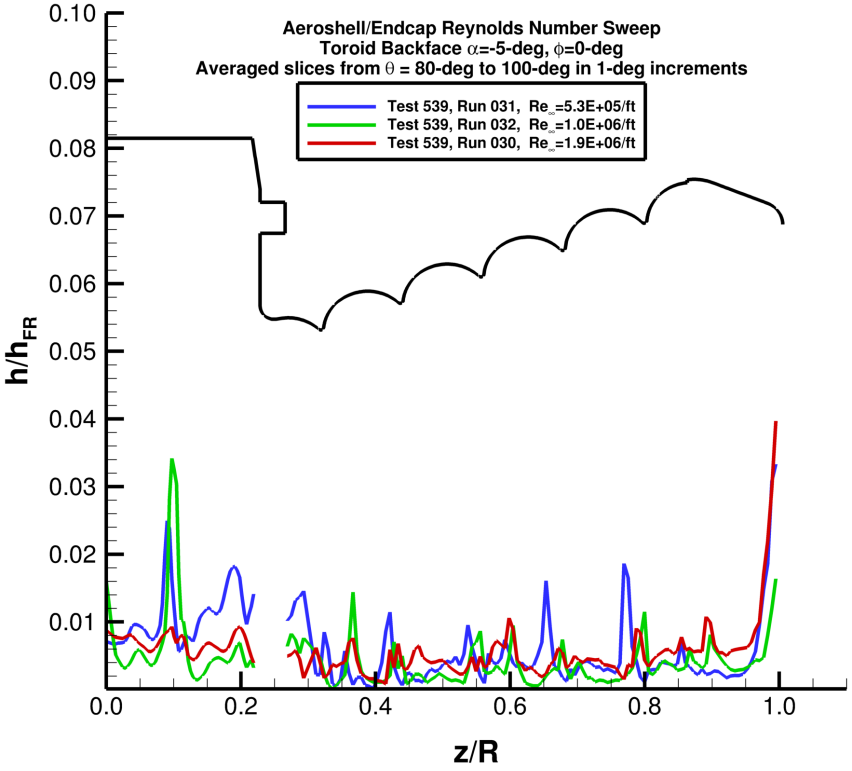


d) Symmetry plane data.

Figure 51. Smooth model S-1: Re_∞ effects at Mach 10, α = +5 deg, ϕ = 0 deg.

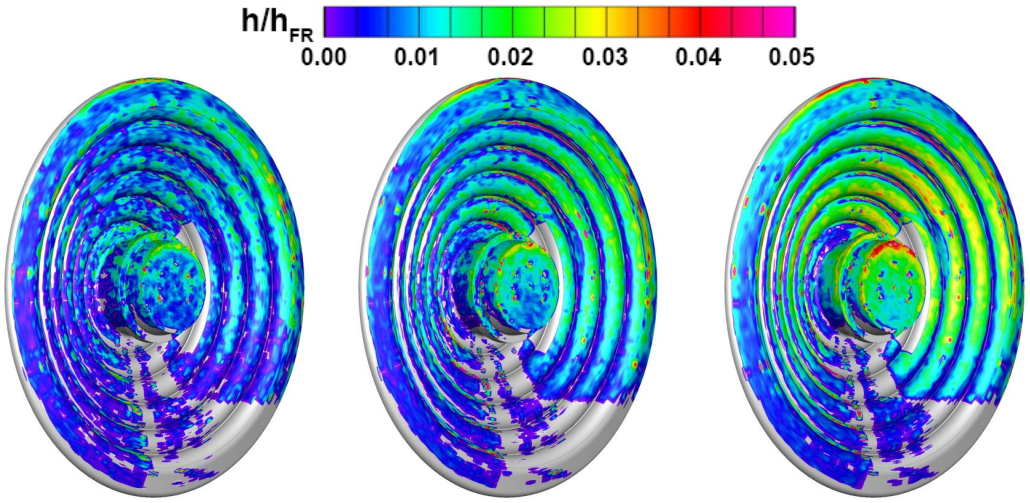


a) Test 539, Run 31, $Re_\infty = 0.5\times10^6$/ft. b) Test 539, Run 32, $Re_\infty = 1.0\times10^6$/ft. c) Test 539, Run 30, $Re_\infty = 1.9\times10^6$/ft.

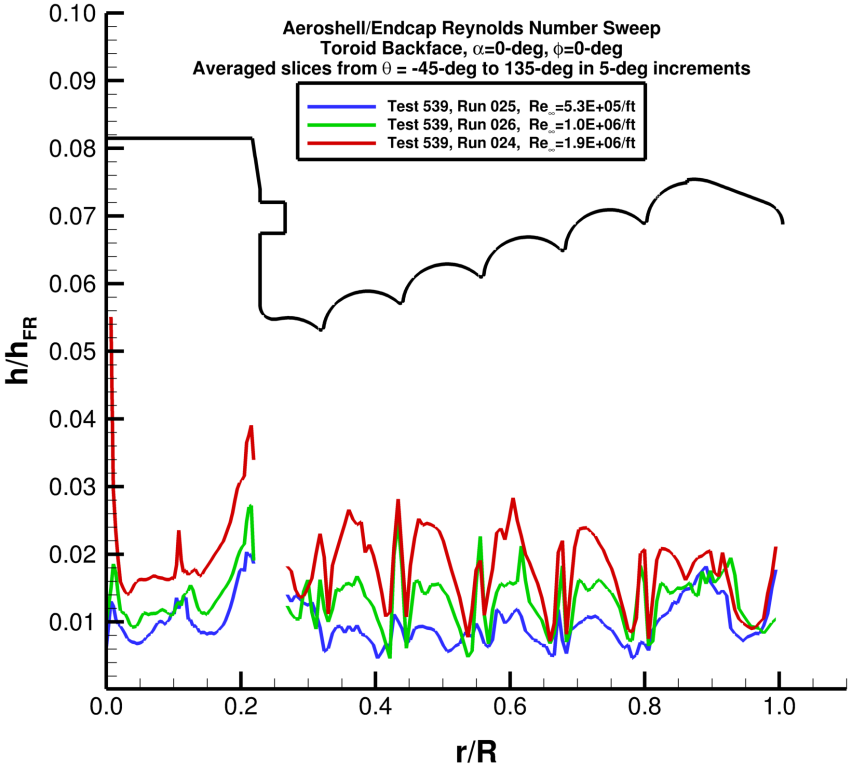


d) Symmetry plane data.

Figure 52. Toroid model T-1: Re_∞ effects at Mach 10, α = -5 deg, ϕ = 0 deg.

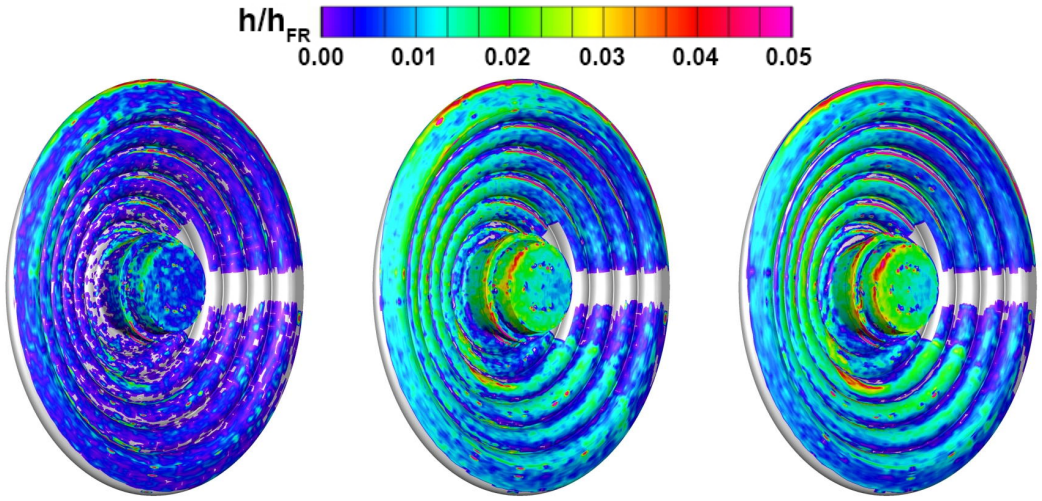


a) Test 539, Run 25, $Re_\infty = 0.5\times10^6$/ft. b) Test 539, Run 26, $Re_\infty = 1.0\times10^6$/ft. c) Test 539, Run 24, $Re_\infty = 1.9\times10^6$/ft.

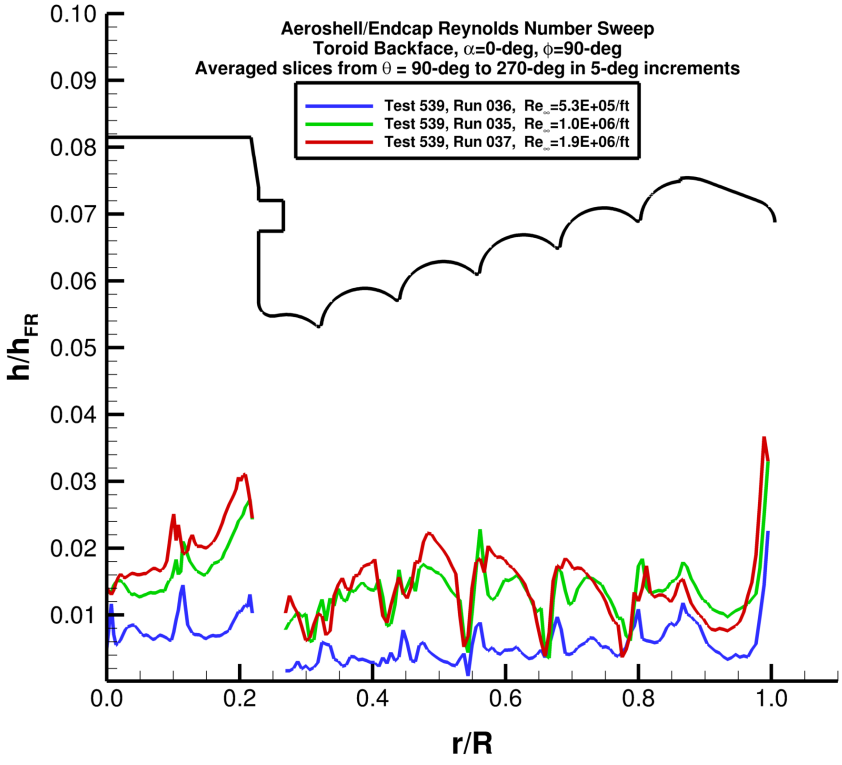


d) Symmetry plane data.

Figure 53. Toroid model T-1: Re_∞ effects at Mach 10, α = 0 deg, ϕ = 0 deg.

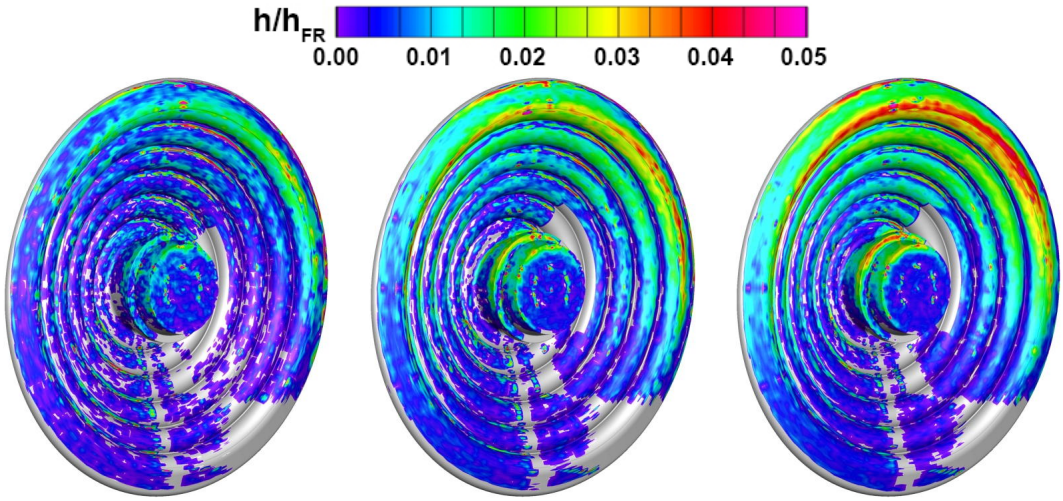


a) Test 539, Run 36, $Re_\infty = 0.5\times10^6$/ft. b) Test 539, Run 35, $Re_\infty = 1.0\times10^6$/ft. c) Test 539, Run 37, $Re_\infty = 1.9\times10^6$/ft.

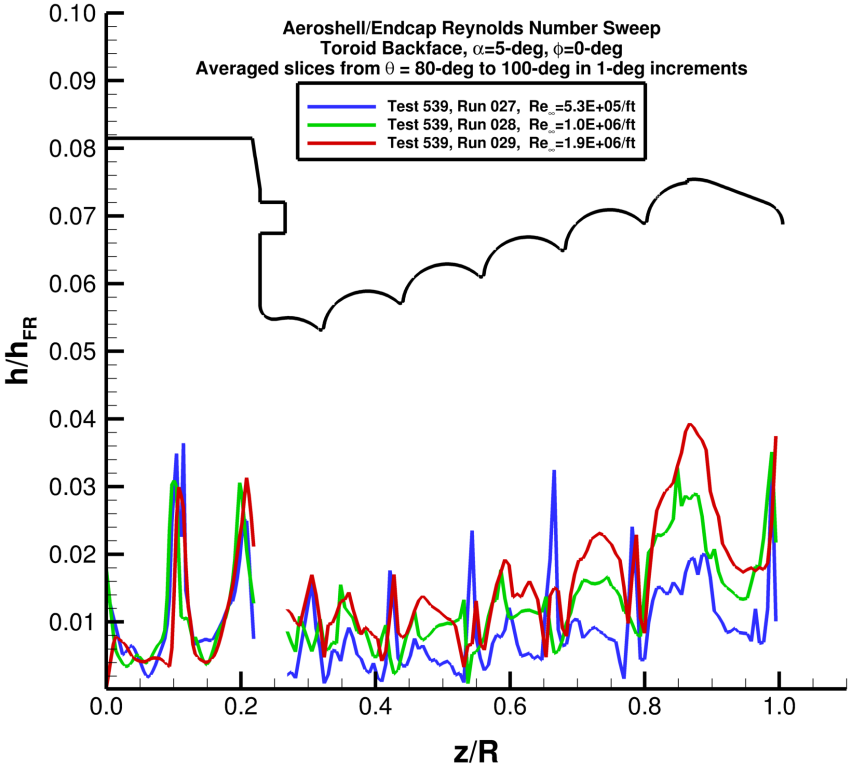


d) Symmetry plane data.

Figure 54. Toroid model T-1: Re_∞ effects at Mach 10, α = 0 deg, ϕ = 90 deg.

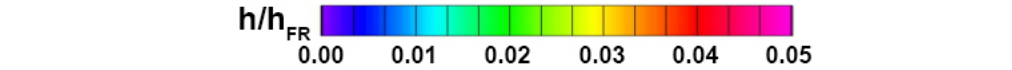


a) Test 539, Run 27, $Re_\infty = 0.5\times10^6$/ft. b) Test 539, Run 28, $Re_\infty = 1.0\times10^6$/ft. c) Test 539, Run 29, $Re_\infty = 1.9\times10^6$/ft.



d) Symmetry plane data.

Figure 55. Toroid model T-1: Re_∞ effects at Mach 10, α = +5 deg, ϕ = 0 deg.



a) Test 7052, Run 100, $Re_\infty = 1.1\times10^6$/ft.

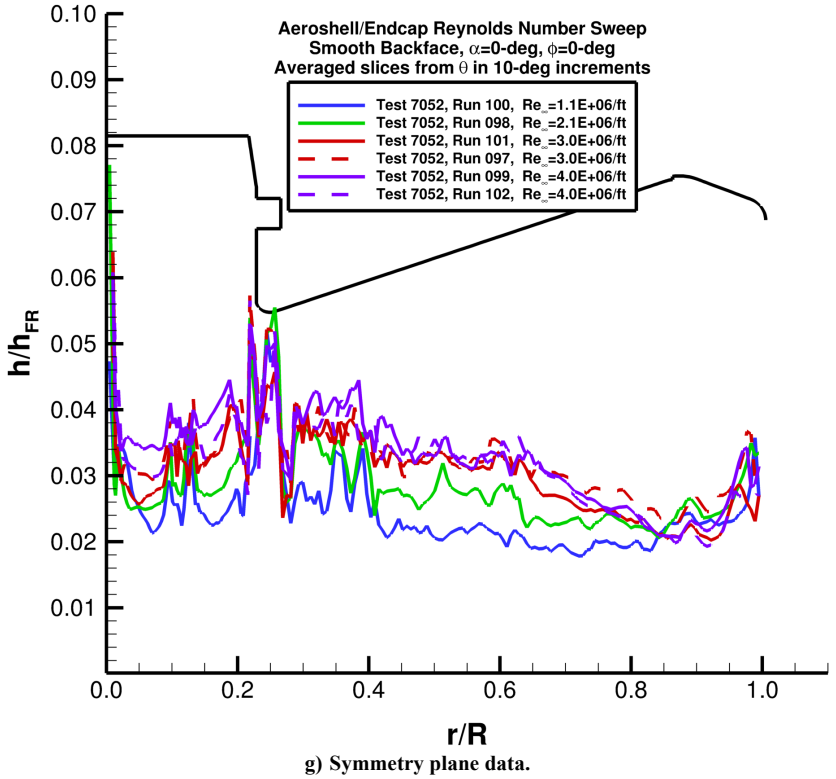
b) Test 7052, Run 98, $Re_\infty = 2.1\times10^6$/ft.

c) Test 7052, Run 101, $Re_\infty = 3.0\times10^6$/ft.

d) Test 7052, Run 97, $Re_\infty = 3.0\times10^6$/ft.

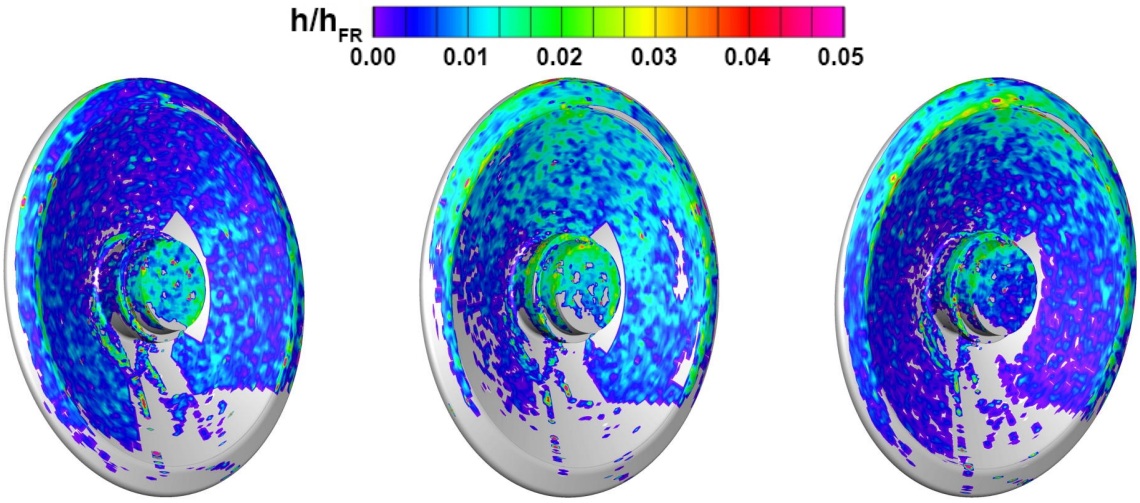
e) Test 7052, Run 99, $Re_\infty = 4.0\times10^6$/ft.

f) Test 7052, Run 102, $Re_\infty = 4.0\times10^6$/ft.



g) Symmetry plane data.

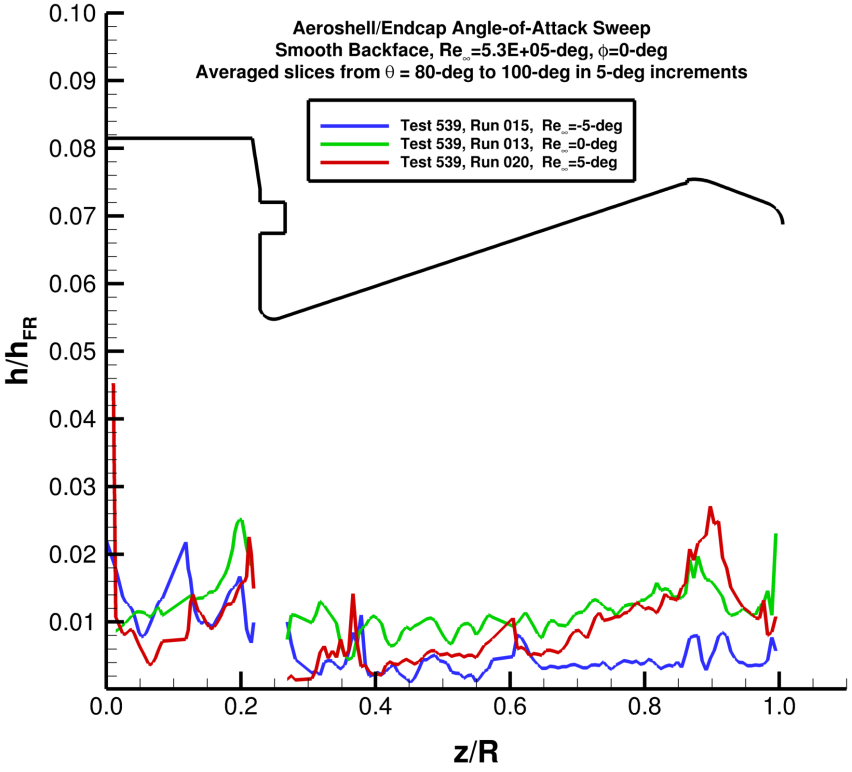
Figure 56. Smooth model S-1: Re_∞ effects at Mach 6, $\alpha = 0$ deg, $\phi = 0$ deg.



a) Test 539, Run 15, α = -5 deg.

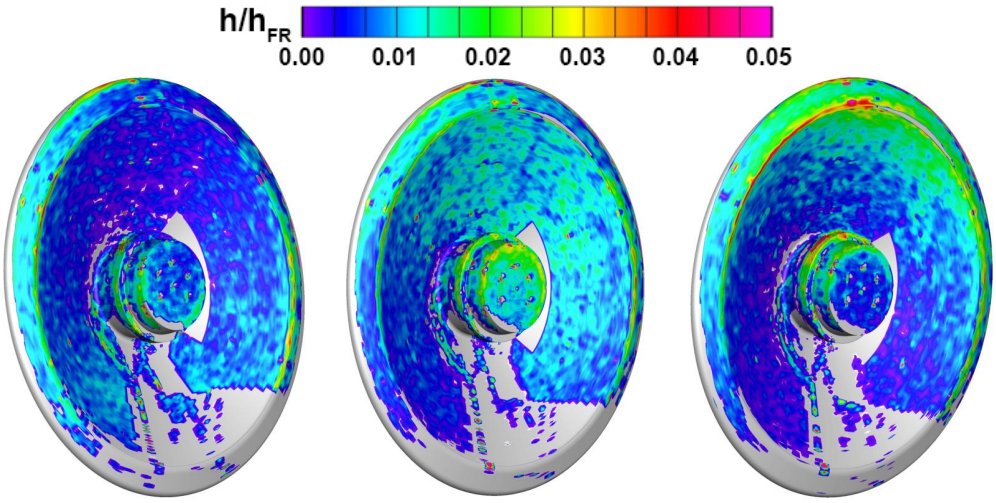
b) Test 539, Run 13, α = 0 deg.

c) Test 539, Run 20, α = +5 deg.

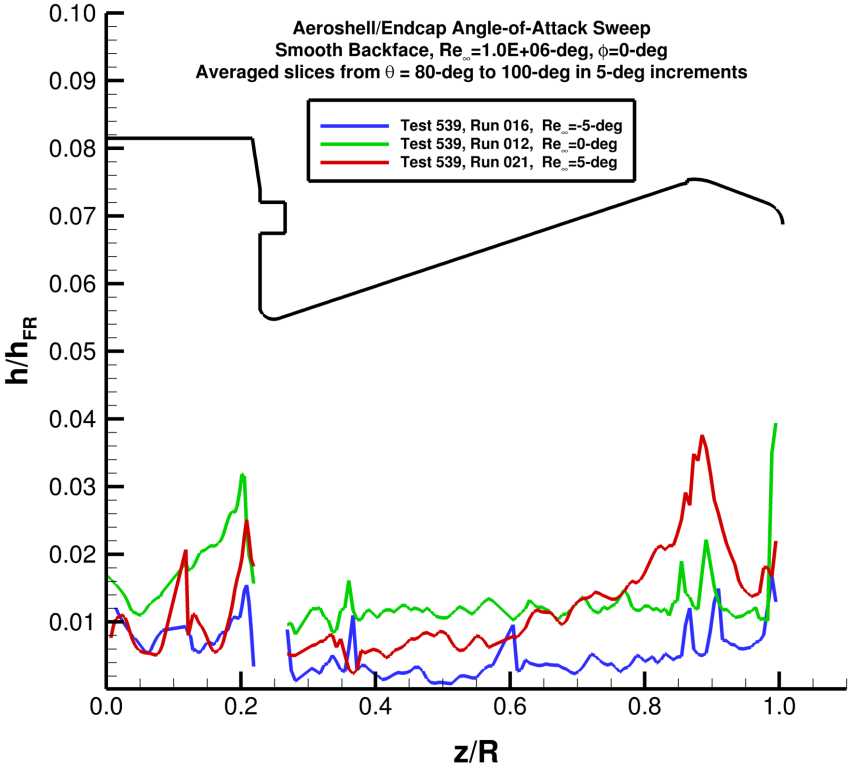


d) Symmetry plane data.

Figure 57. Smooth model S-1: α sweep at Mach 10, $Re_\infty = 0.5\times10^6$/ft, ϕ = 0 deg.

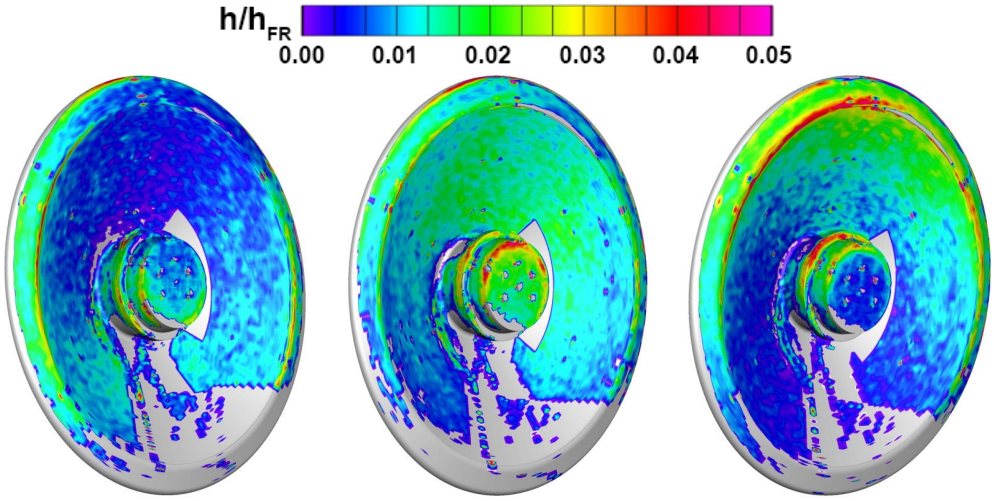


a) Test 539, Run 16, α = -5 deg. b) Test 539, Run 12, α = 0 deg. c) Test 539, Run 21, α = +5 deg.

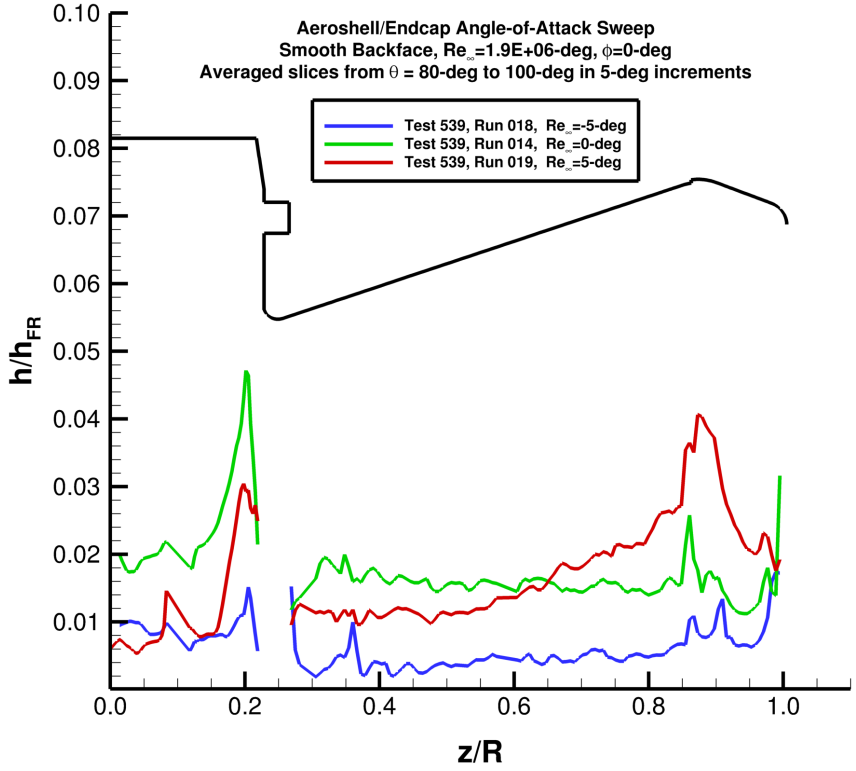


d) Symmetry plane data.

Figure 58. Smooth model S-1: α sweep at Mach 10, $Re_\infty = 1.0\times10^6$/ft, ϕ = 0 deg.

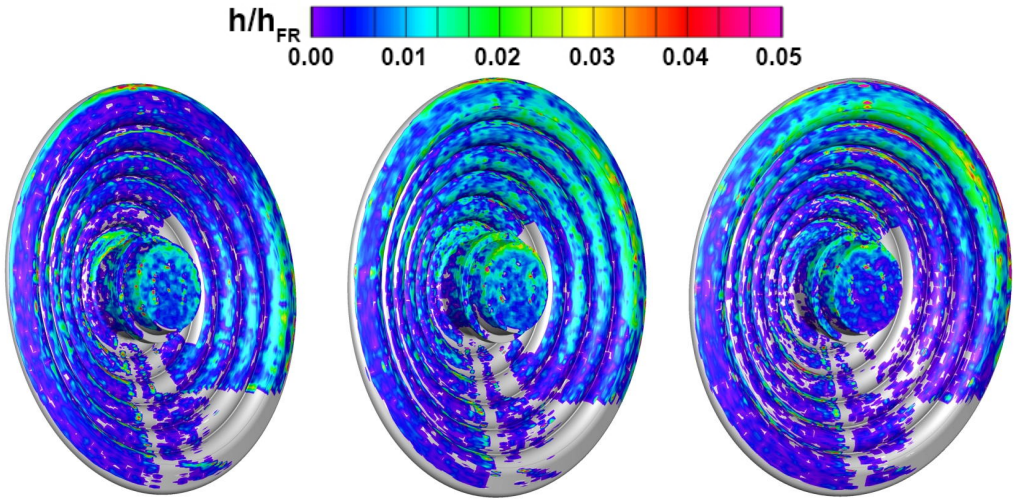


a) Test 539, Run 18, α = -5 deg. b) Test 539, Run 14, α = 0 deg. c) Test 539, Run 19, α = +5 deg.

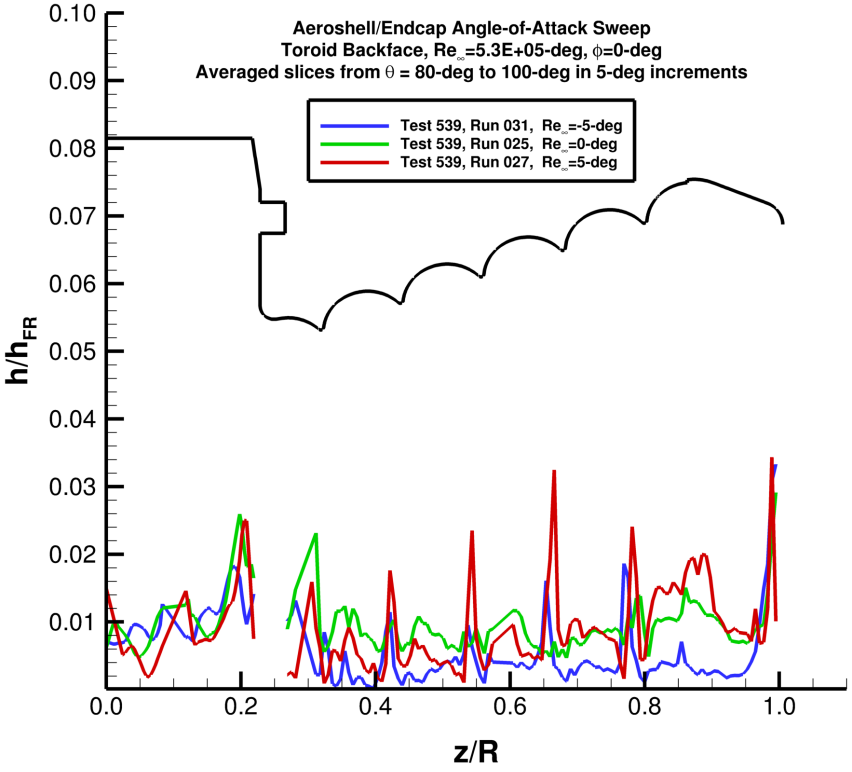


d) Symmetry plane data.

Figure 59. Smooth model S-1: α sweep at Mach 10, Re_∞ = 1.9×10^6/ft, ϕ = 0 deg.

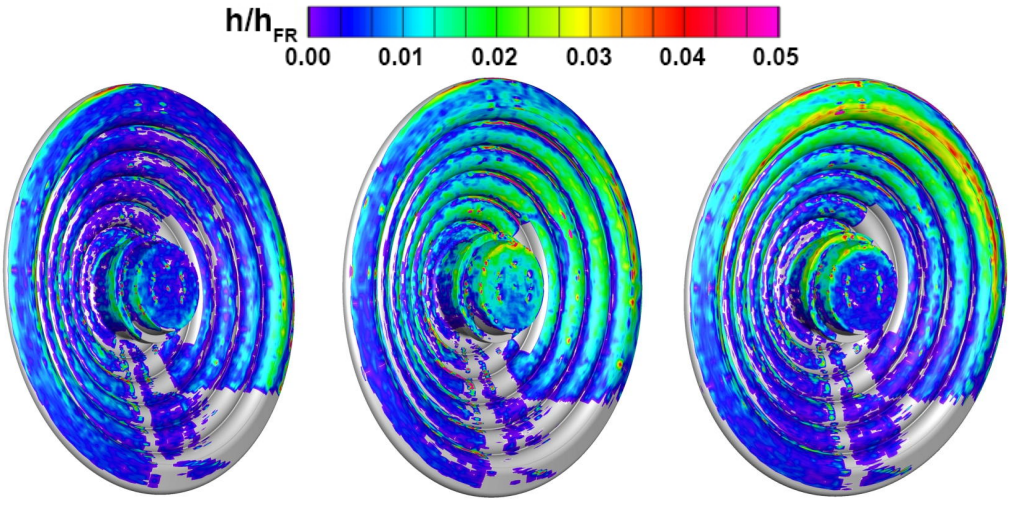


a) Test 539, Run 31, α = -5 deg. b) Test 539, Run 25, α = 0 deg. c) Test 539, Run 27, α = +5 deg.

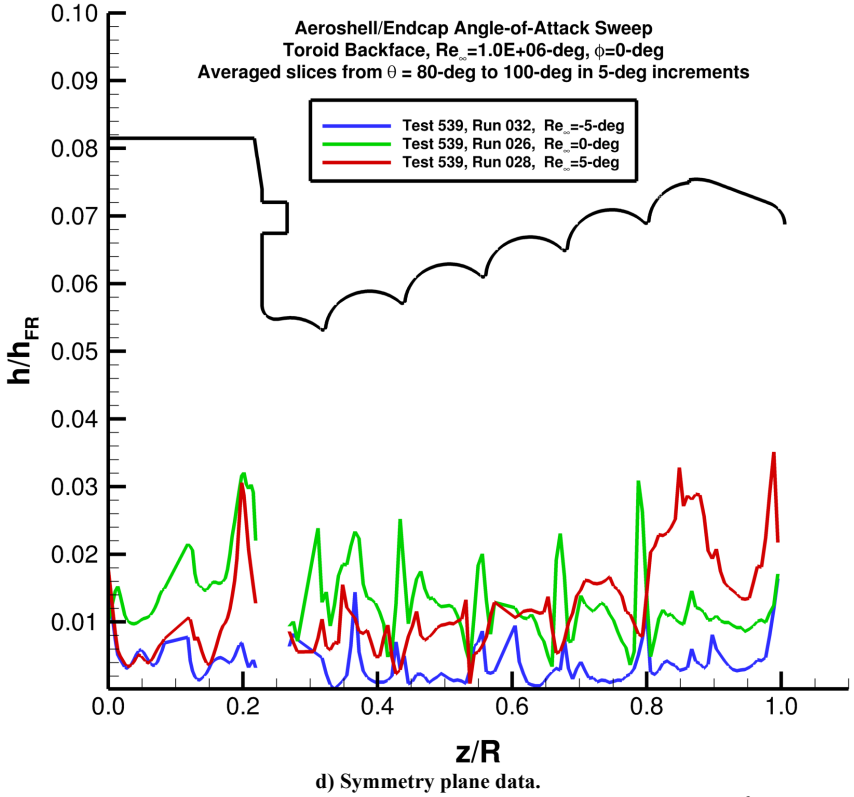


d) Symmetry plane data.

Figure 60. Toroid model T-1: α sweep at Mach 10, $Re_\infty = 0.5\times10^6$/ft, ϕ = 0 deg.

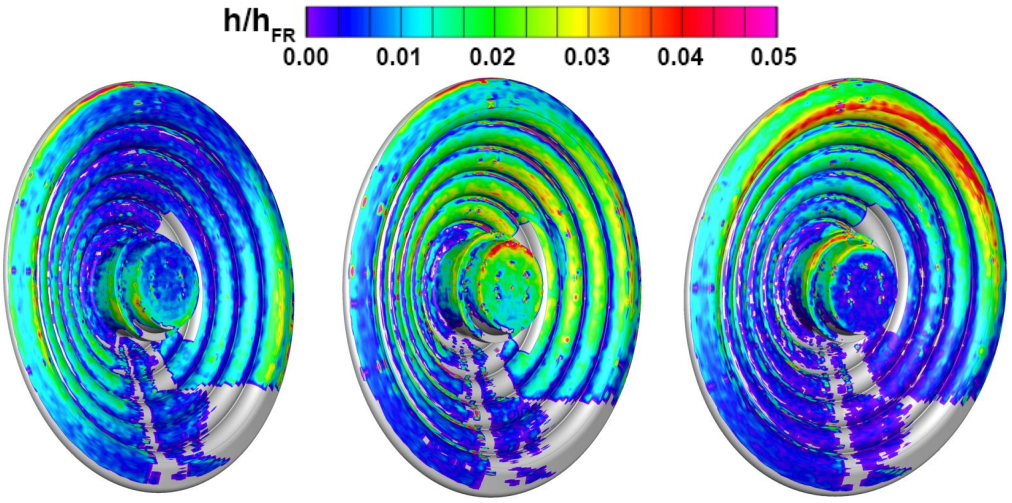


a) Test 539, Run 32, α = -5 deg. b) Test 539, Run 26, α = 0 deg. c) Test 539, Run 28, α = +5 deg.

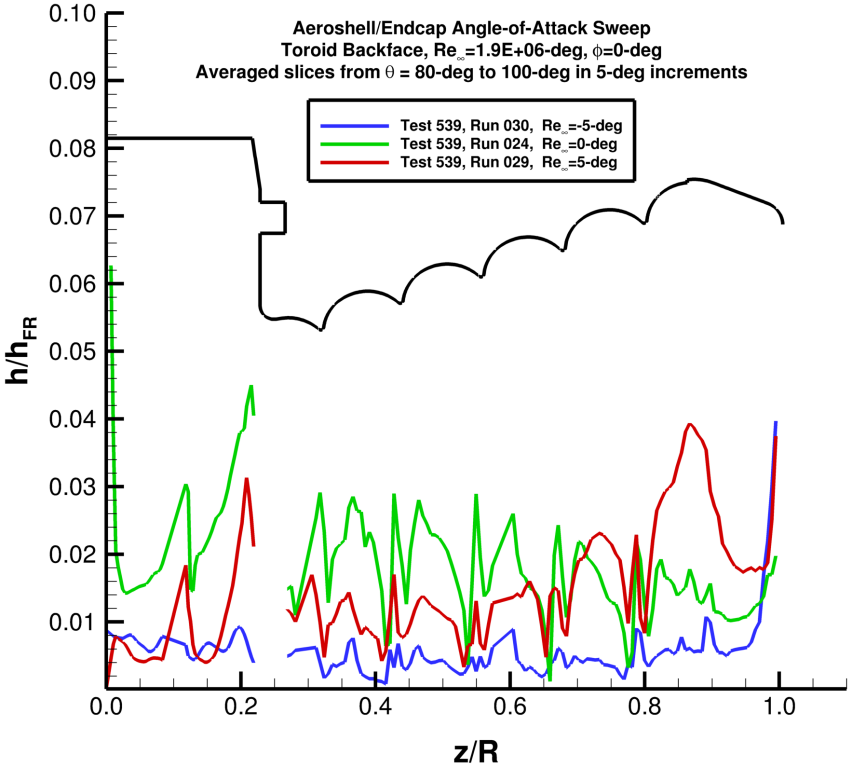


d) Symmetry plane data.

Figure 61. Toroid model T-1: α sweep at Mach 10, $Re_\infty = 1.0\times10^6$/ft, ϕ = 0 deg.

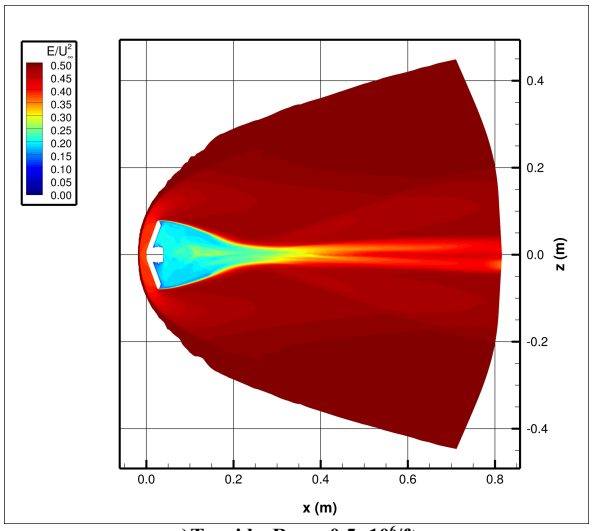


a) Test 539, Run 30, α = -5 deg. b) Test 539, Run 24, α = 0 deg. c) Test 539, Run 29, α = +5 deg.

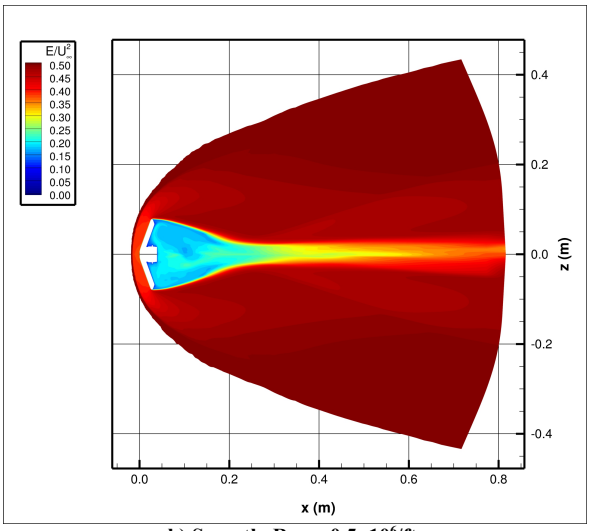


d)Symmetry plane data.

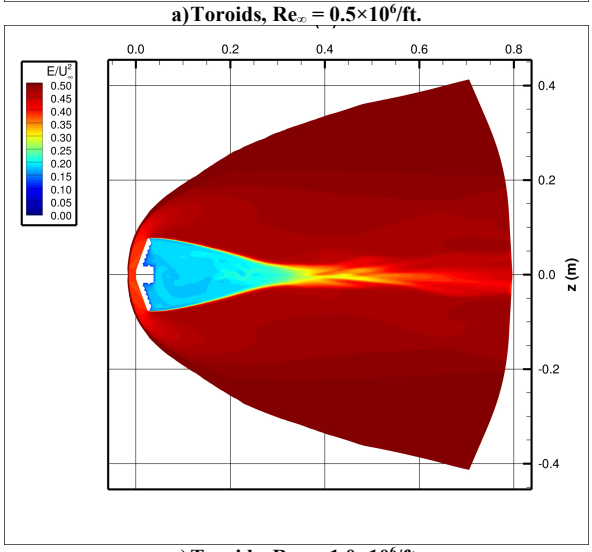
Figure 62. Toroid model T-1: α sweep at Mach 10, $Re_\infty = 1.9\times10^6$/ft, ϕ = 0 deg.



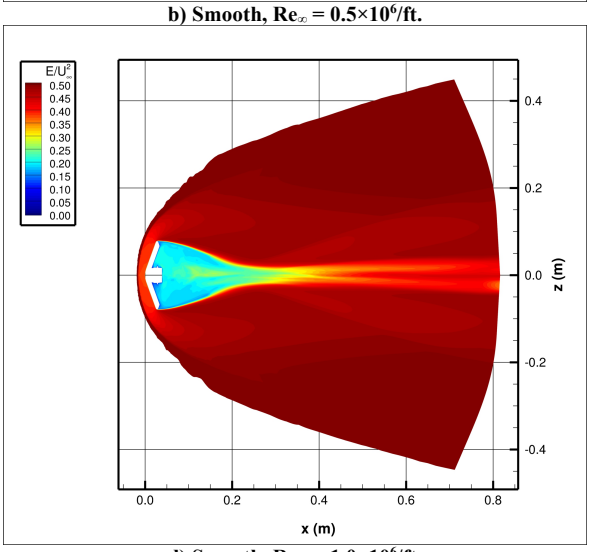
a) Toroids, $Re_\infty = 0.5\times10^6$/ft.



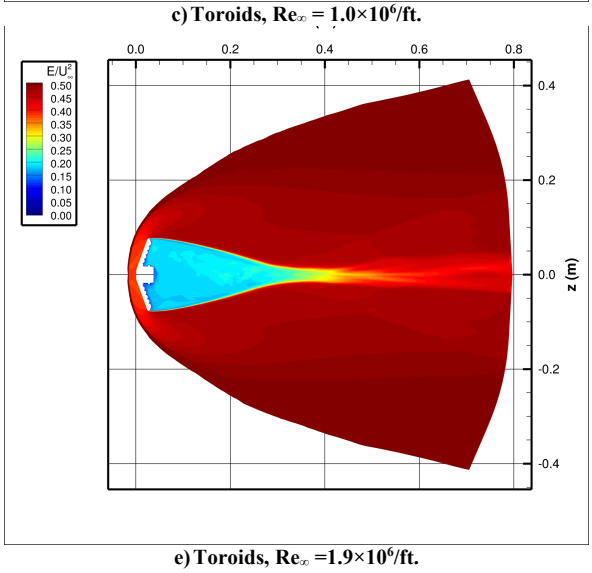
b) Smooth, $Re_\infty = 0.5\times10^6$/ft.



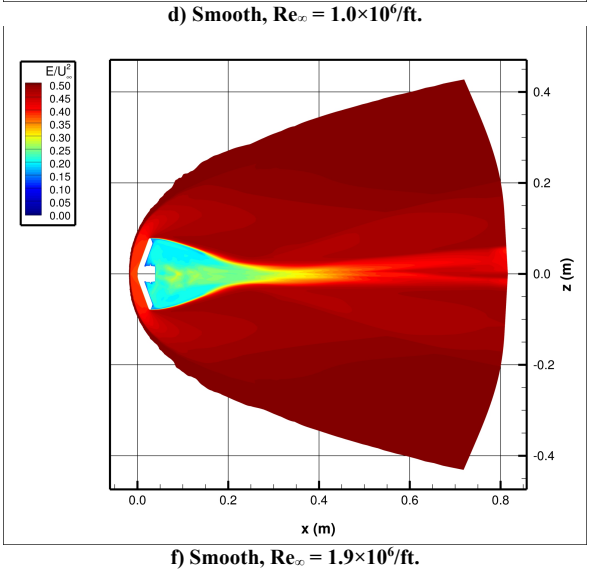
c) Toroids, $Re_\infty = 1.0\times10^6$/ft.



d) Smooth, $Re_\infty = 1.0\times10^6$/ft.

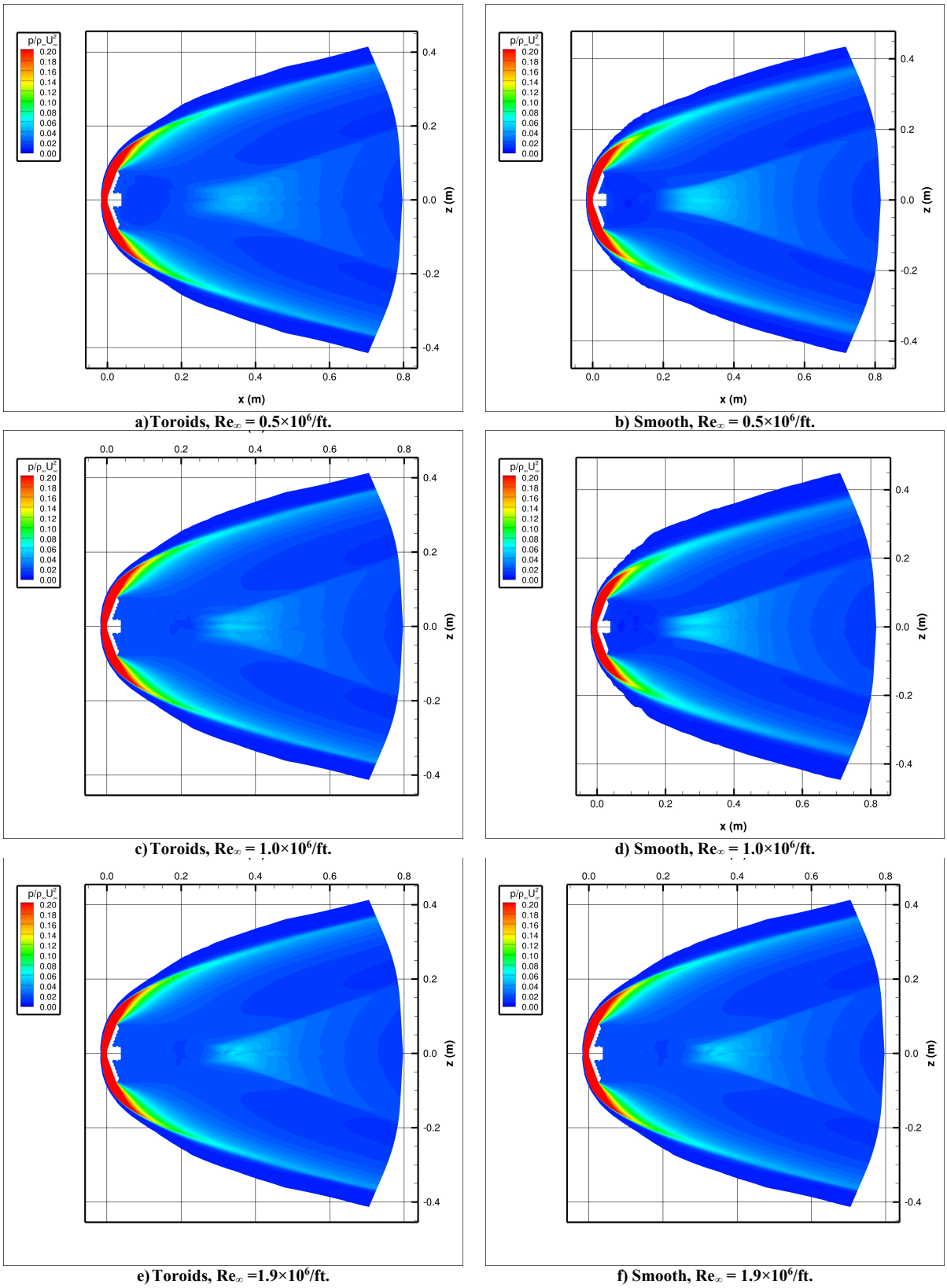


e) Toroids, $Re_\infty = 1.9\times10^6$/ft.



f) Smooth, $Re_\infty = 1.9\times10^6$/ft.

Figure 63. Predicted flow field properties: total energy at Mach 10.



a) Toroids, $Re_\infty = 0.5\times10^6$/ft.

b) Smooth, $Re_\infty = 0.5\times10^6$/ft.

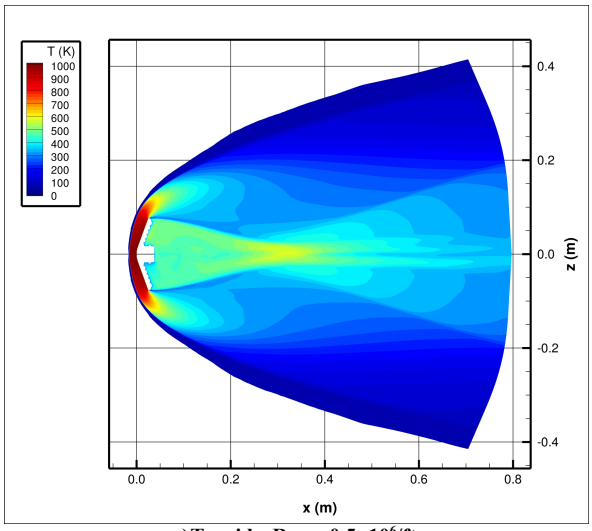
c) Toroids, $Re_\infty = 1.0\times10^6$/ft.

d) Smooth, $Re_\infty = 1.0\times10^6$/ft.

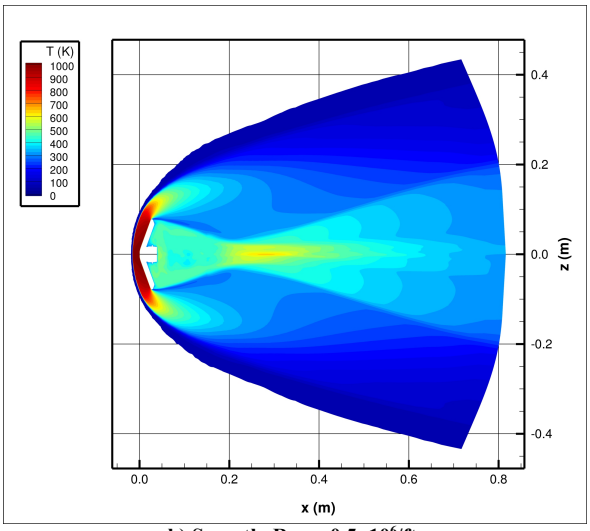
e) Toroids, $Re_\infty = 1.9\times10^6$/ft.

f) Smooth, $Re_\infty = 1.9\times10^6$/ft.

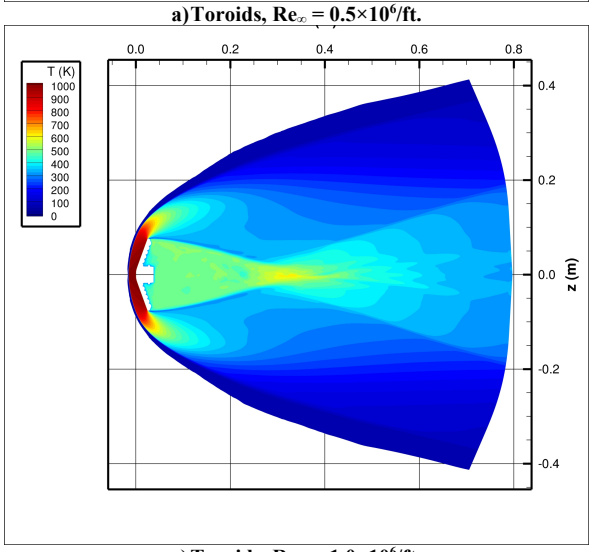
Figure 64. Predicted flow field properties: pressure at Mach 10.



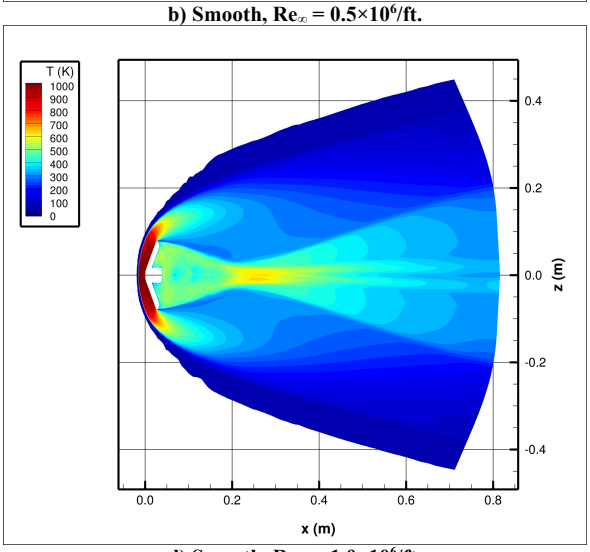
a) Toroids, $Re_\infty = 0.5\times10^6$/ft.



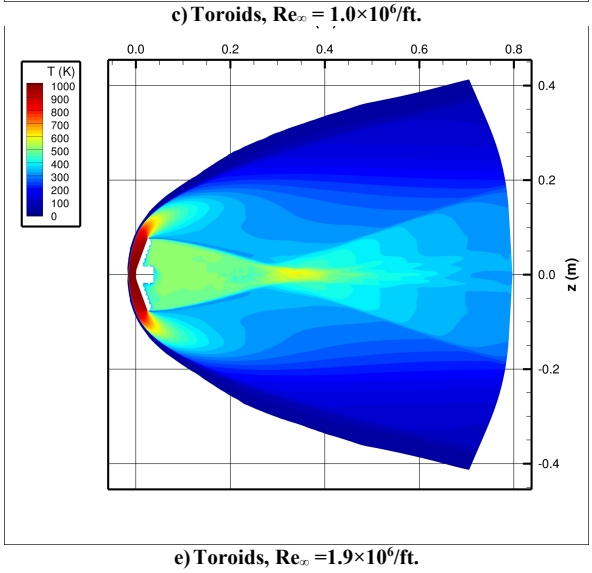
b) Smooth, $Re_\infty = 0.5\times10^6$/ft.



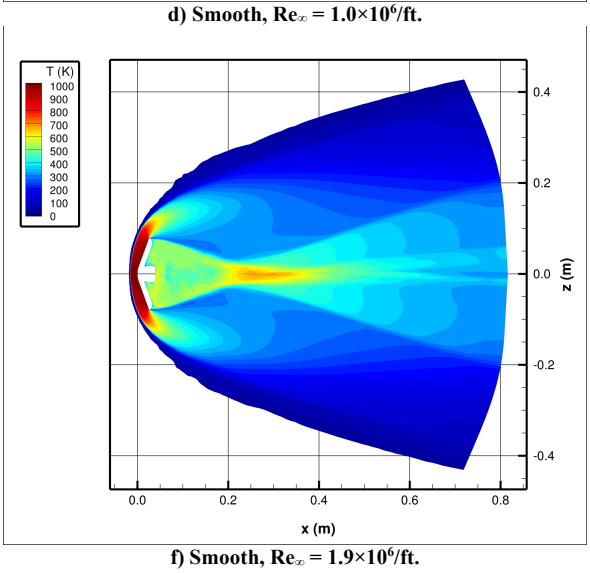
c) Toroids, $Re_\infty = 1.0\times10^6$/ft.



d) Smooth, $Re_\infty = 1.0\times10^6$/ft.

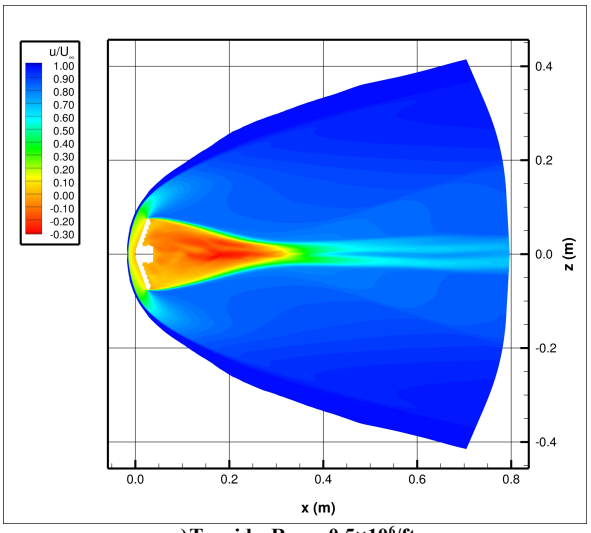


e) Toroids, $Re_\infty = 1.9\times10^6$/ft.

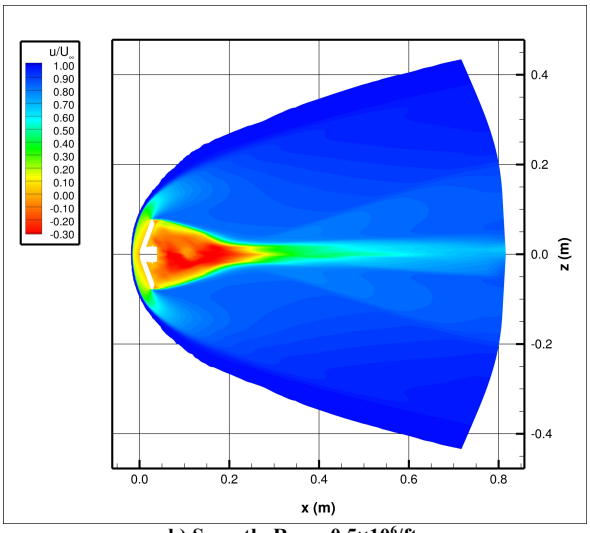


f) Smooth, $Re_\infty = 1.9\times10^6$/ft.

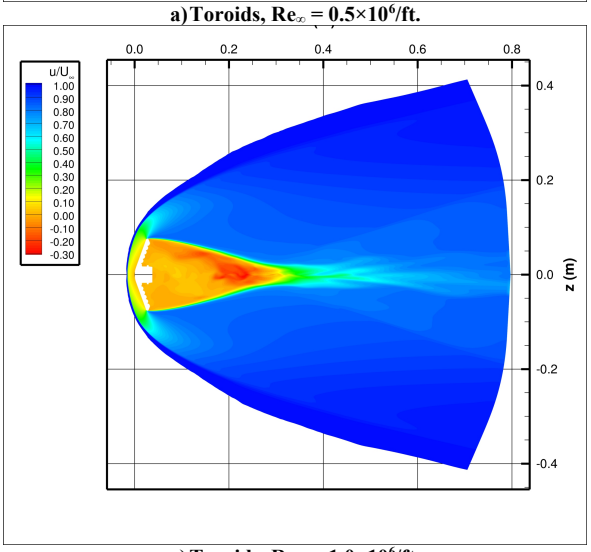
Figure 65. Predicted flow field properties: temperature at Mach 10.



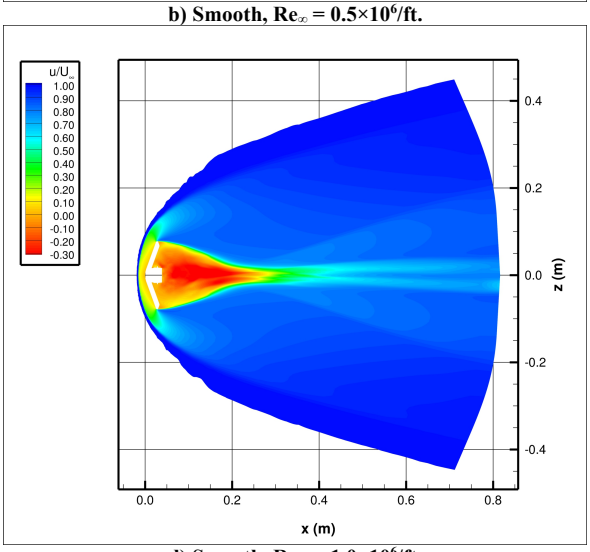
a) Toroids, $Re_\infty = 0.5\times10^6$/ft.



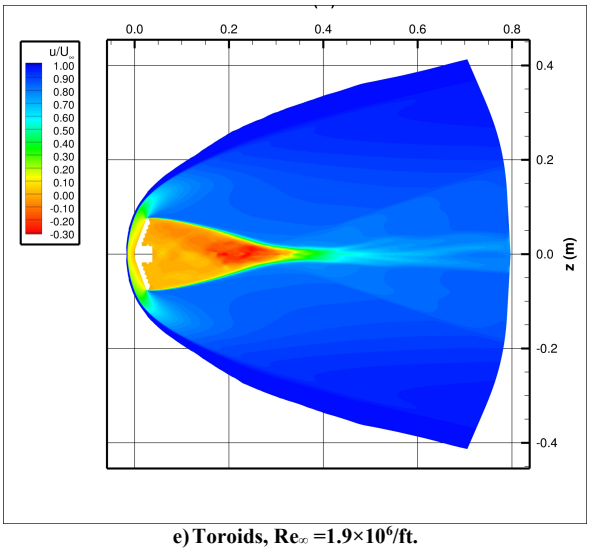
b) Smooth, $Re_\infty = 0.5\times10^6$/ft.



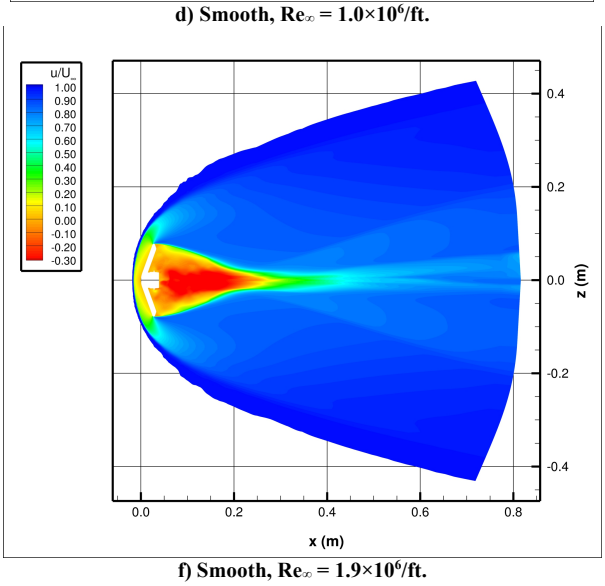
c) Toroids, $Re_\infty = 1.0\times10^6$/ft.



d) Smooth, $Re_\infty = 1.0\times10^6$/ft.

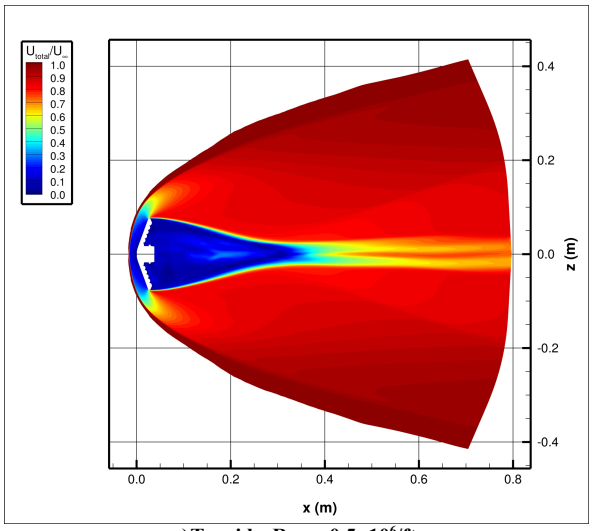


e) Toroids, $Re_\infty = 1.9\times10^6$/ft.

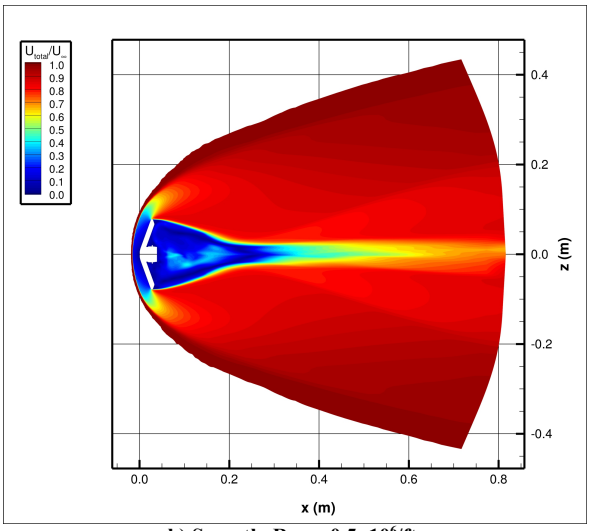


f) Smooth, $Re_\infty = 1.9\times10^6$/ft.

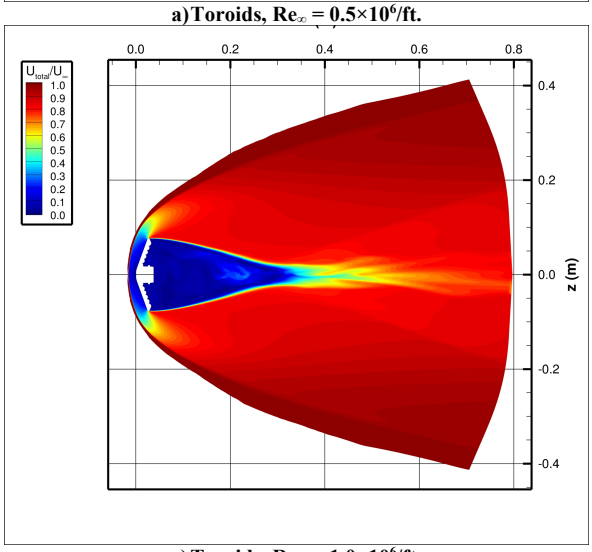
Figure 66. Predicted flow field properties: *x*-component of velocity at Mach 10.



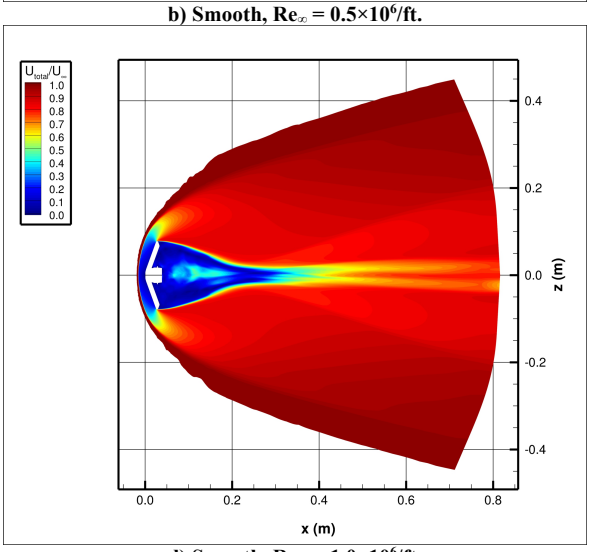
a) Toroids, $Re_\infty = 0.5\times10^6$/ft.



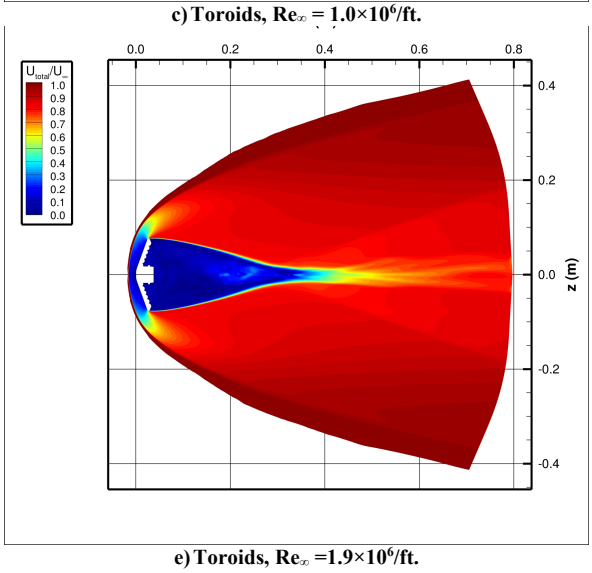
b) Smooth, $Re_\infty = 0.5\times10^6$/ft.



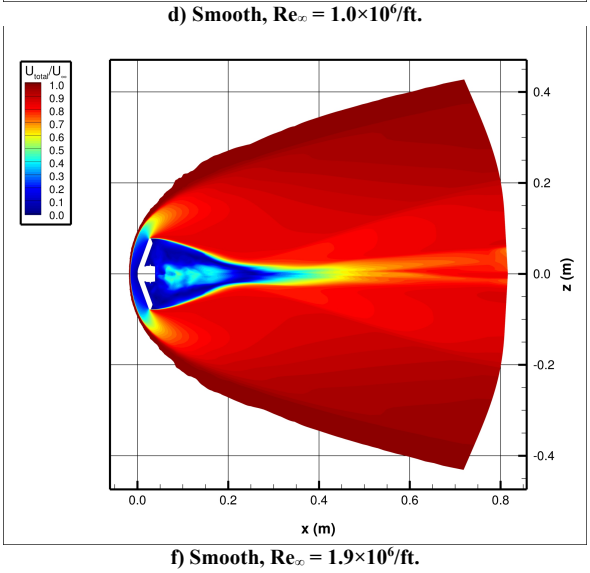
c) Toroids, $Re_\infty = 1.0\times10^6$/ft.



d) Smooth, $Re_\infty = 1.0\times10^6$/ft.

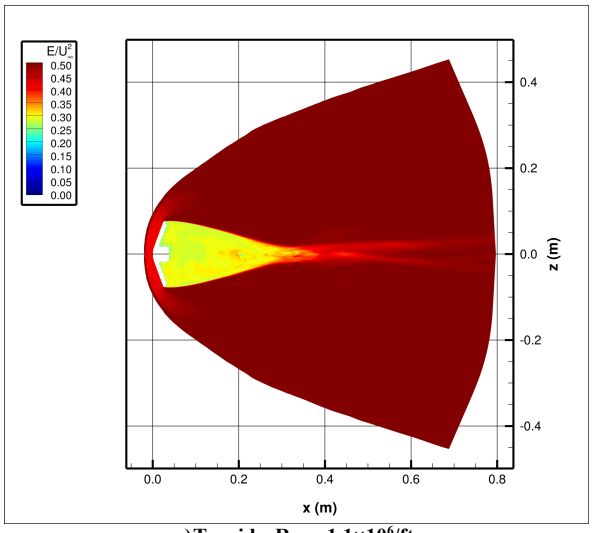


e) Toroids, $Re_\infty = 1.9\times10^6$/ft.

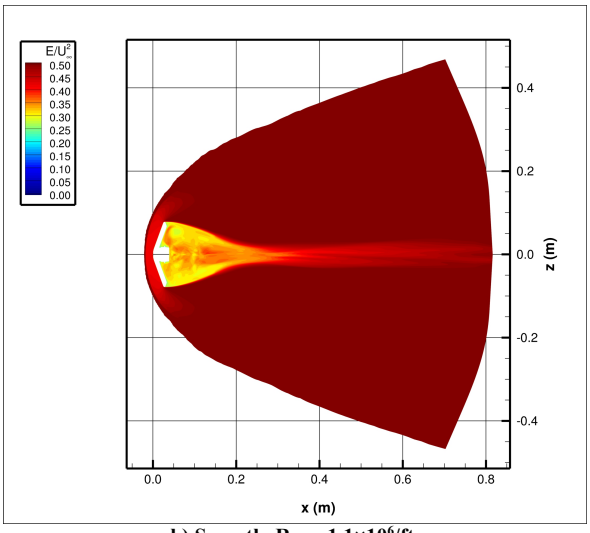


f) Smooth, $Re_\infty = 1.9\times10^6$/ft.

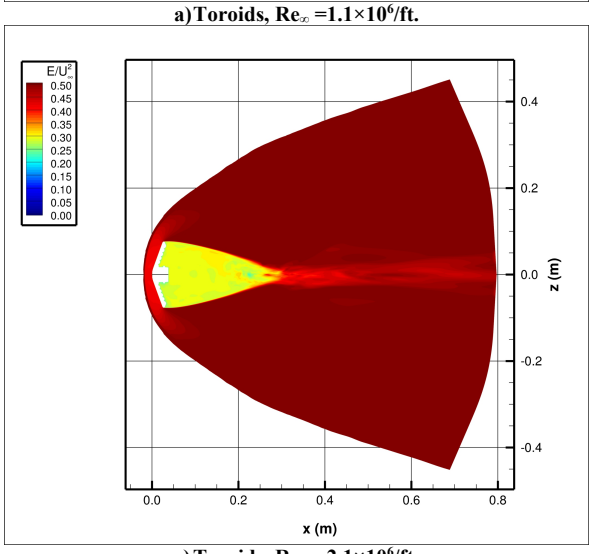
Figure 67. Predicted flow field properties: total velocity at Mach 10.



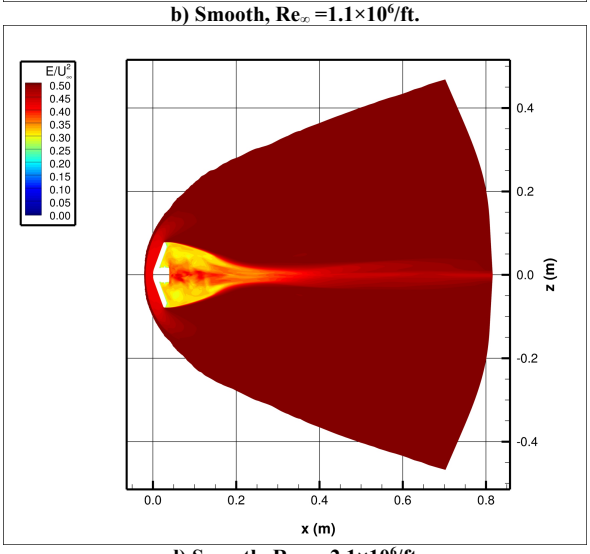
a) Toroids, Re_∞ =1.1×10⁶/ft.



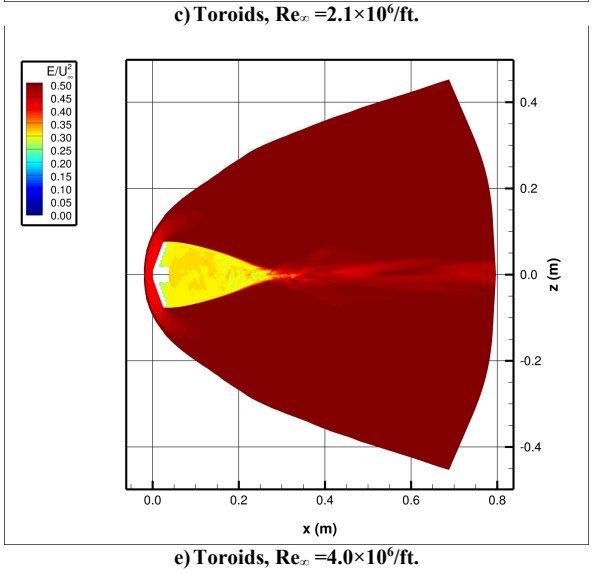
b) Smooth, Re_∞ =1.1×10⁶/ft.



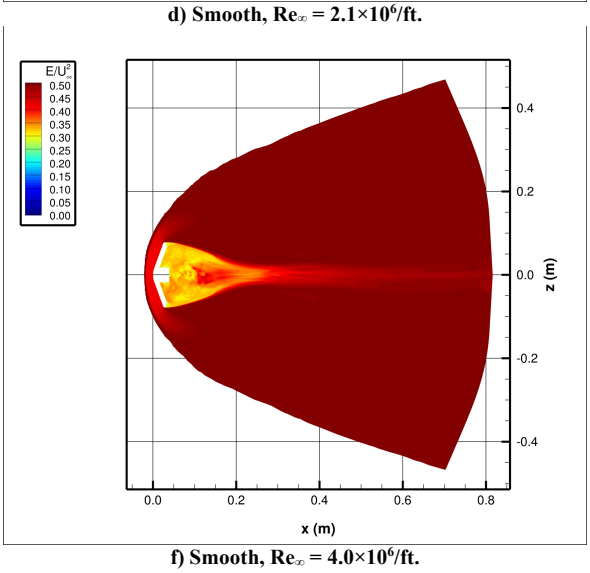
c) Toroids, Re_∞ =2.1×10⁶/ft.



d) Smooth, Re_∞ = 2.1×10⁶/ft.

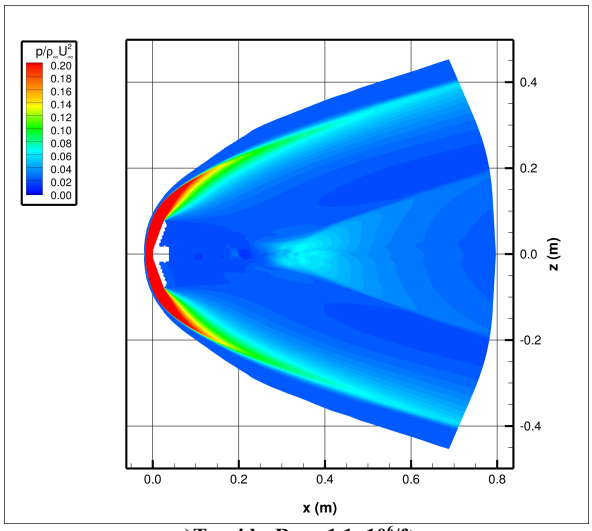


e) Toroids, Re_∞ =4.0×10⁶/ft.

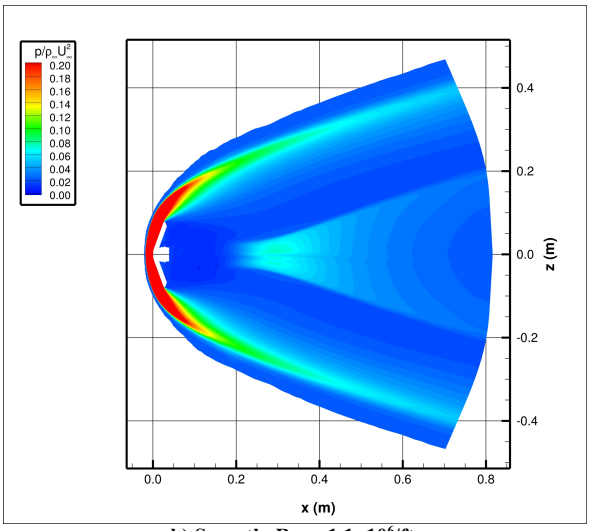


f) Smooth, Re_∞ = 4.0×10⁶/ft.

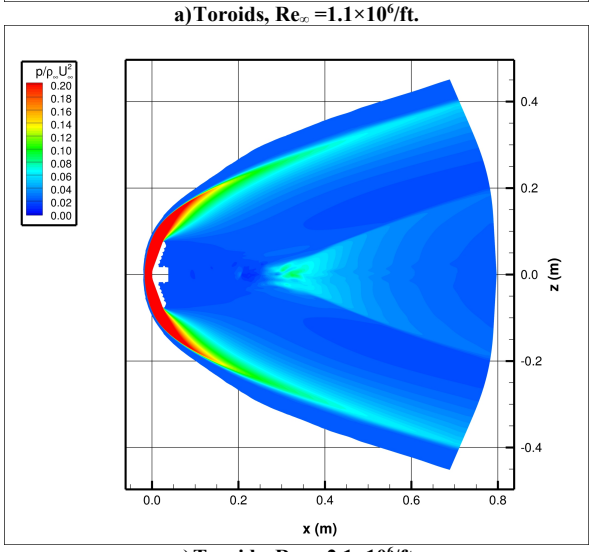
Figure 68. Predicted flow field properties: total energy at Mach 6.



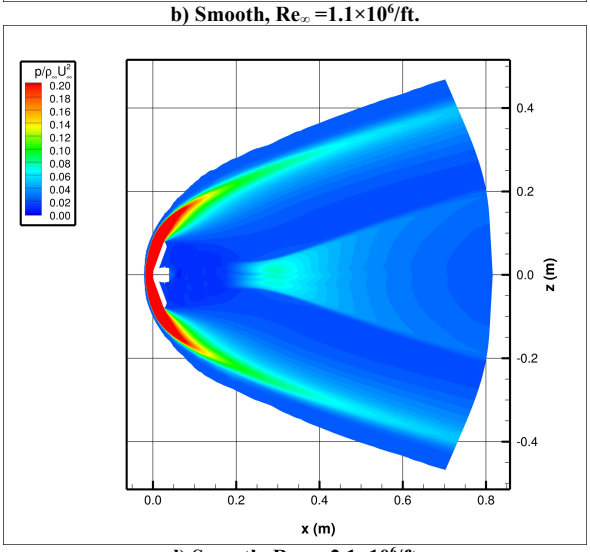
a) Toroids, Re_∞ =1.1×10^6/ft.



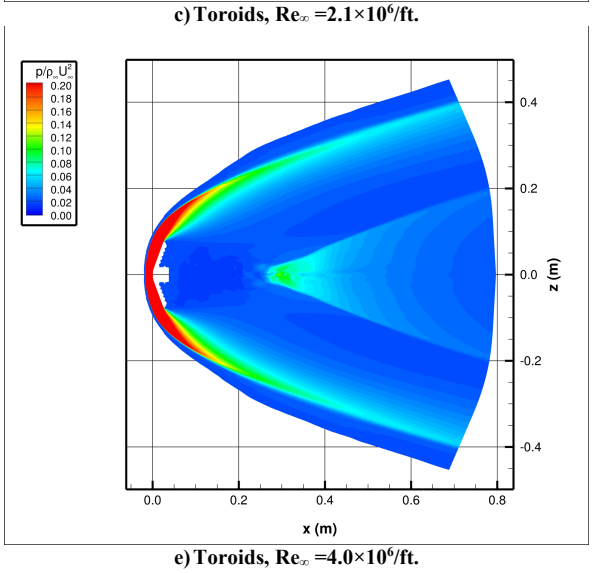
b) Smooth, Re_∞ =1.1×10^6/ft.



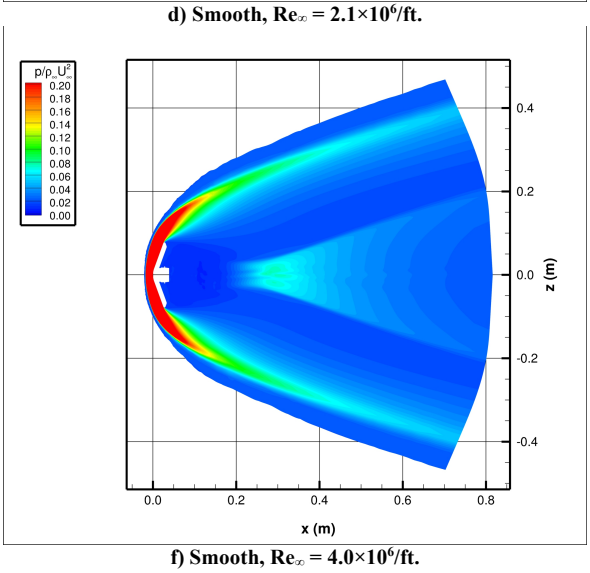
c) Toroids, Re_∞ =2.1×10^6/ft.



d) Smooth, Re_∞ = 2.1×10^6/ft.

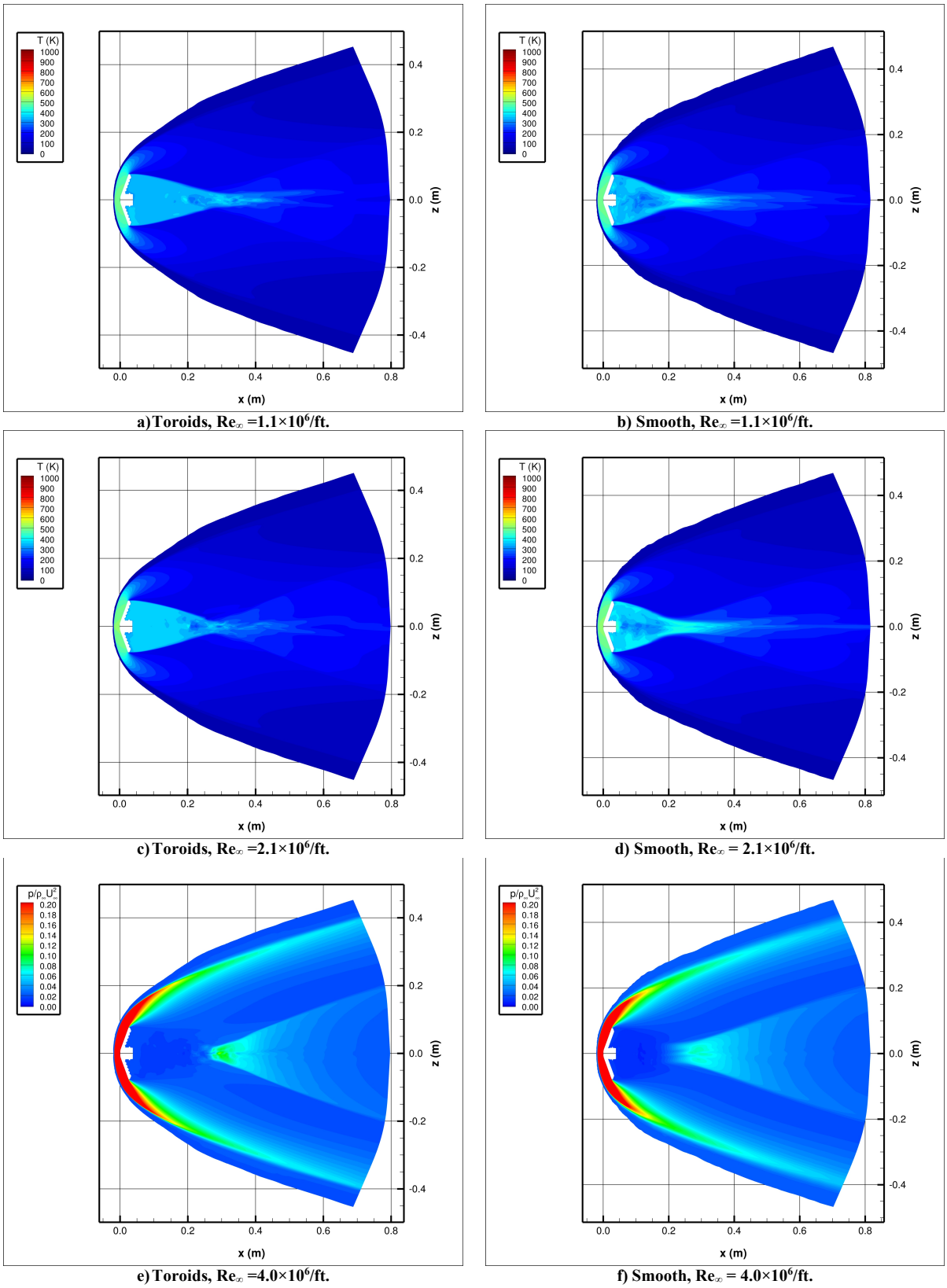


e) Toroids, Re_∞ =4.0×10^6/ft.



f) Smooth, Re_∞ = 4.0×10^6/ft.

Figure 69. Predicted flow field properties: pressure at Mach 6.



a) Toroids, Re_∞ =1.1×10^6/ft.

b) Smooth, Re_∞ =1.1×10^6/ft.

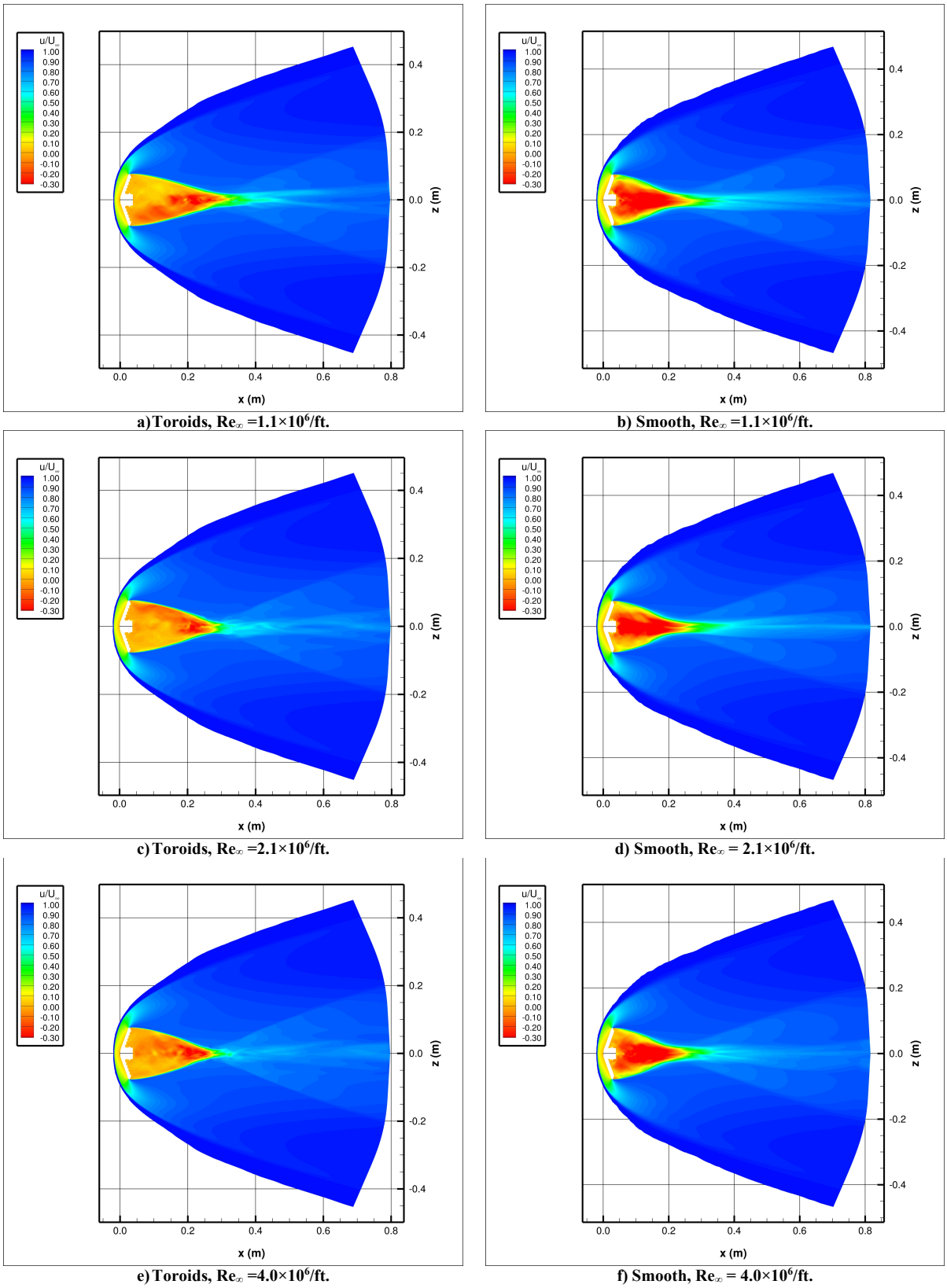
c) Toroids, Re_∞ =2.1×10^6/ft.

d) Smooth, Re_∞ = 2.1×10^6/ft.

e) Toroids, Re_∞ =4.0×10^6/ft.

f) Smooth, Re_∞ = 4.0×10^6/ft.

Figure 70. Predicted flow field properties: temperature at Mach 6.



a) Toroids, Re_∞ =1.1×10^6/ft.

b) Smooth, Re_∞ =1.1×10^6/ft.

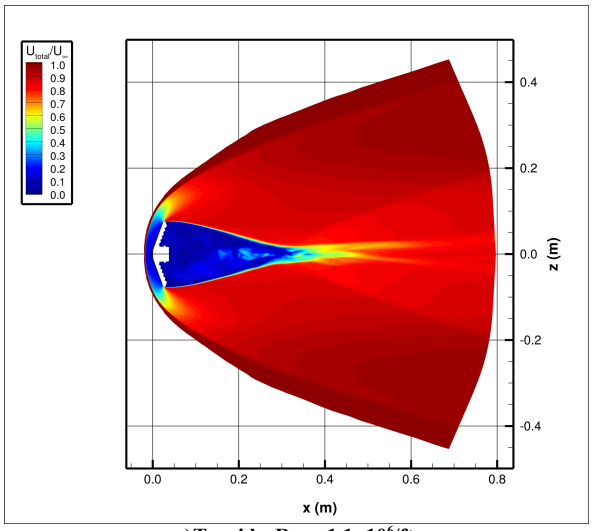
c) Toroids, Re_∞ =2.1×10^6/ft.

d) Smooth, Re_∞ = 2.1×10^6/ft.

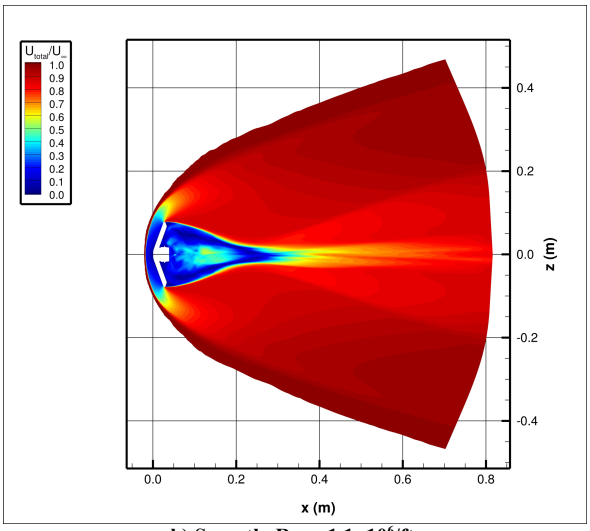
e) Toroids, Re_∞ =4.0×10^6/ft.

f) Smooth, Re_∞ = 4.0×10^6/ft.

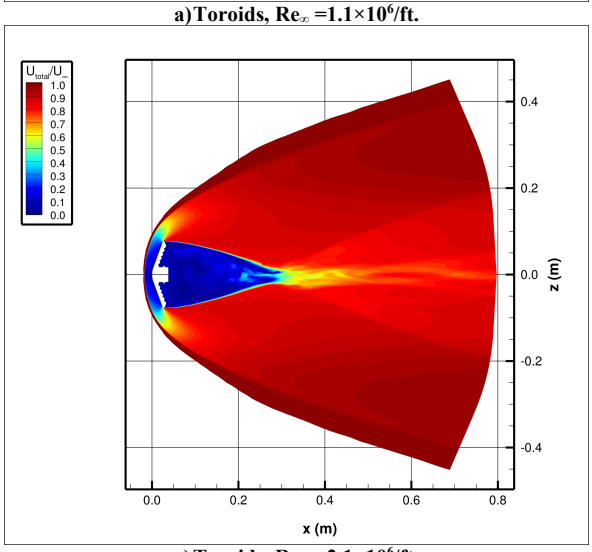
Figure 71. Predicted flow field properties: *x*-component of velocity at Mach 6.



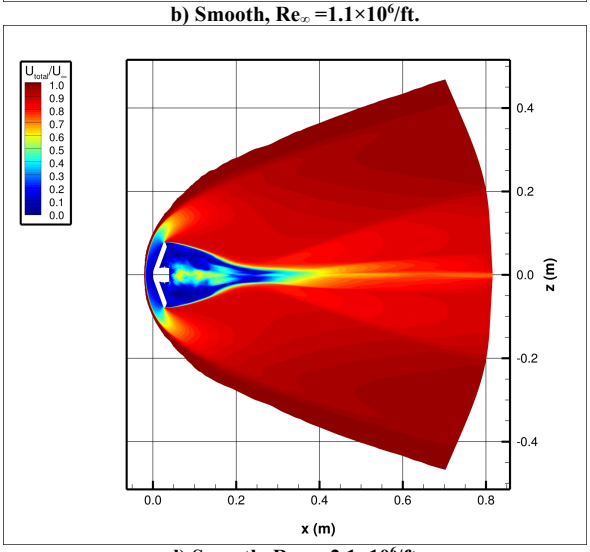
a) Toroids, Re_∞ =1.1×10^6/ft.



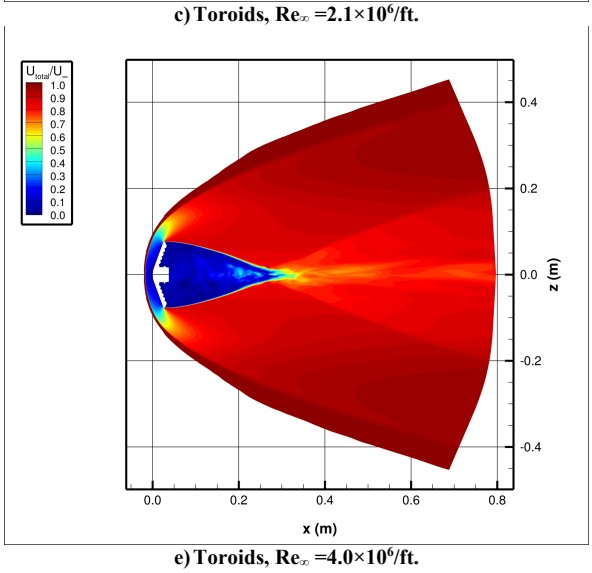
b) Smooth, Re_∞ =1.1×10^6/ft.



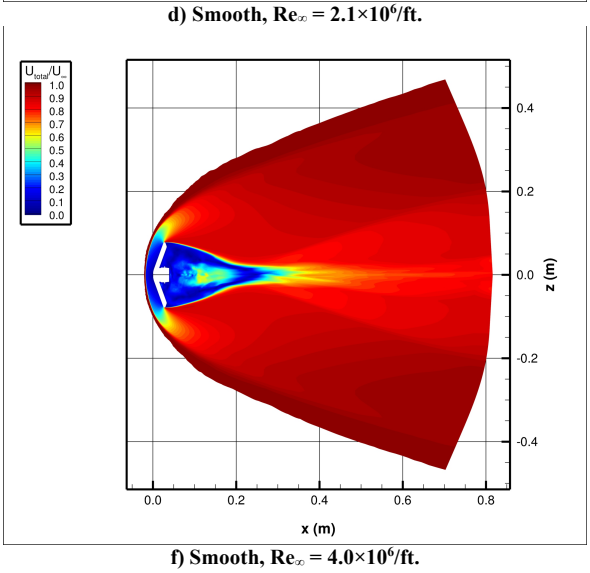
c) Toroids, Re_∞ =2.1×10^6/ft.



d) Smooth, Re_∞ = 2.1×10^6/ft.



e) Toroids, Re_∞ =4.0×10^6/ft.



f) Smooth, Re_∞ = 4.0×10^6/ft.

Figure 72. Predicted flow field properties: total velocity at Mach 6.

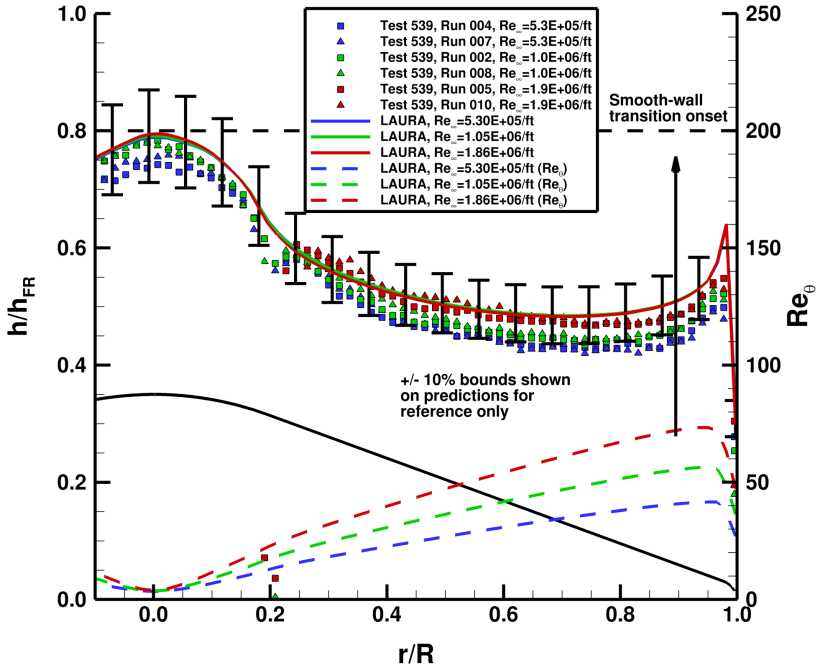


Figure 73. Aeroshell front heating comparison, LAURA vs. Mach 10 data.

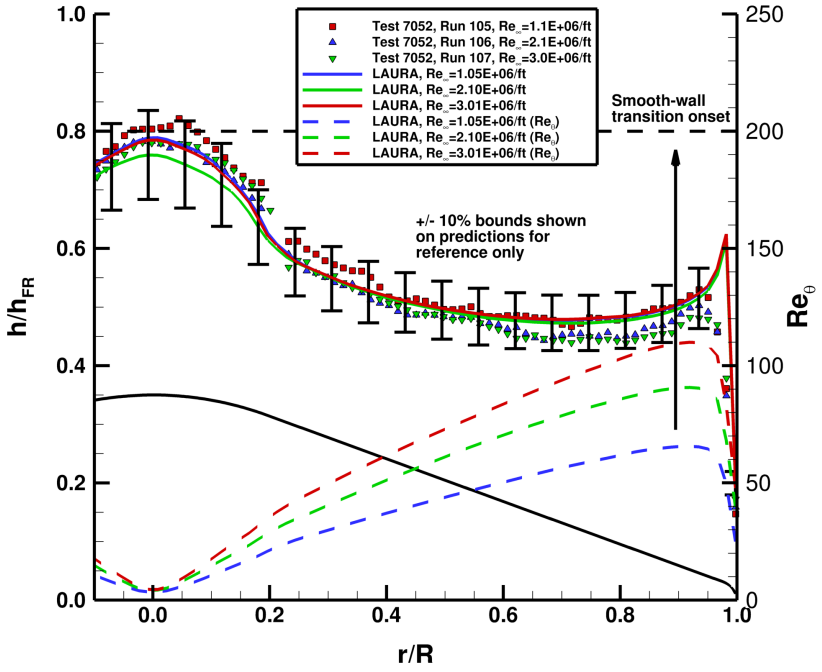
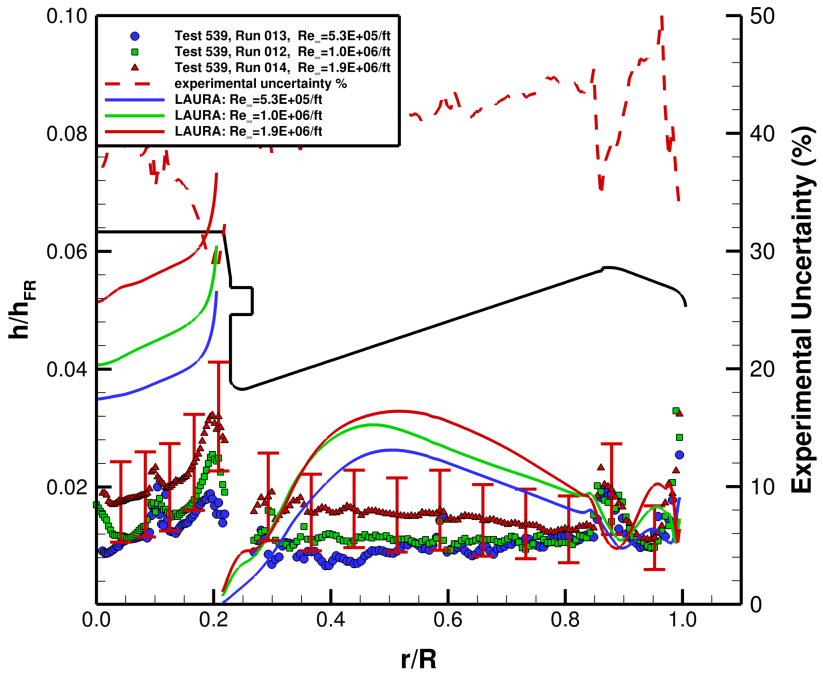
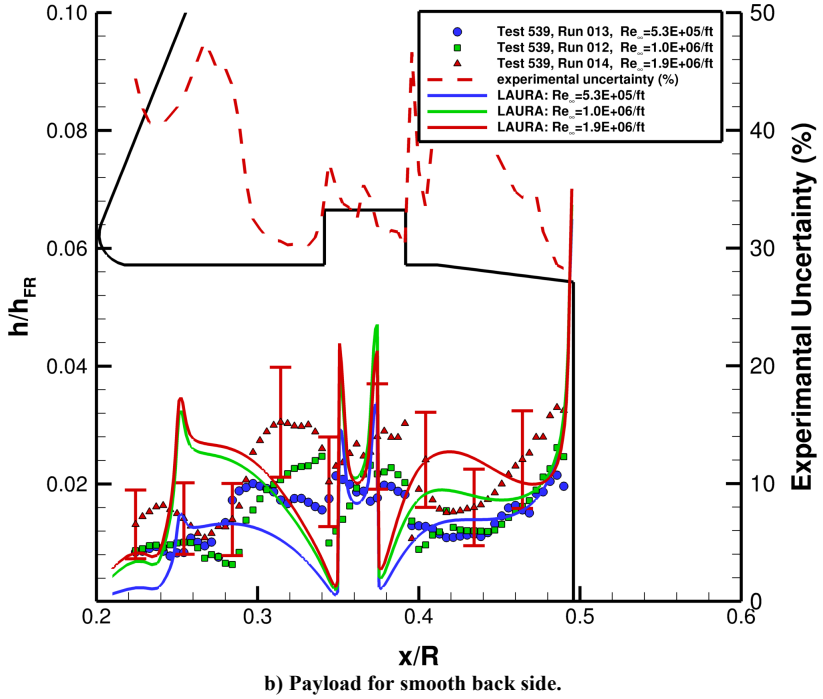


Figure 74. Aeroshell front heating comparison, LAURA vs. Mach 6 data.

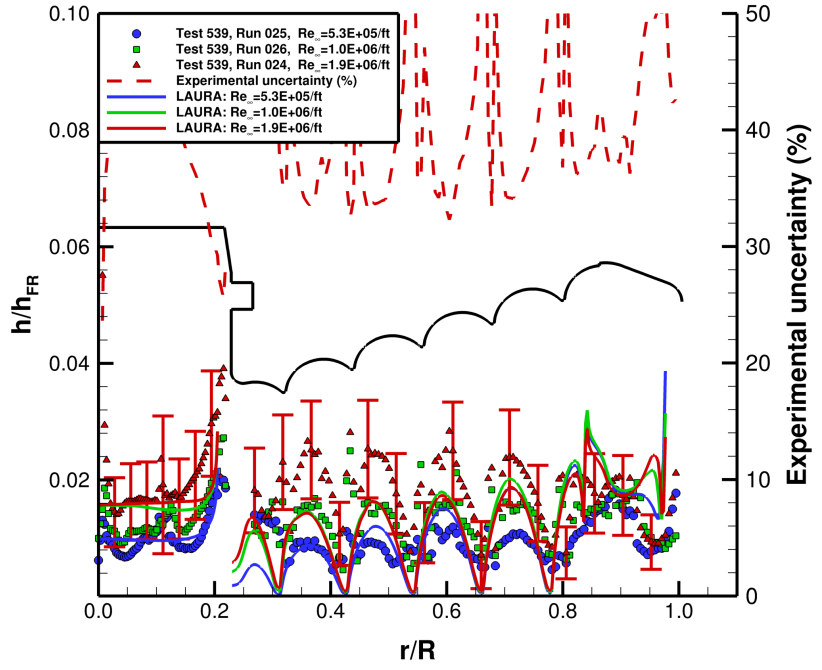


a) Smooth back side.

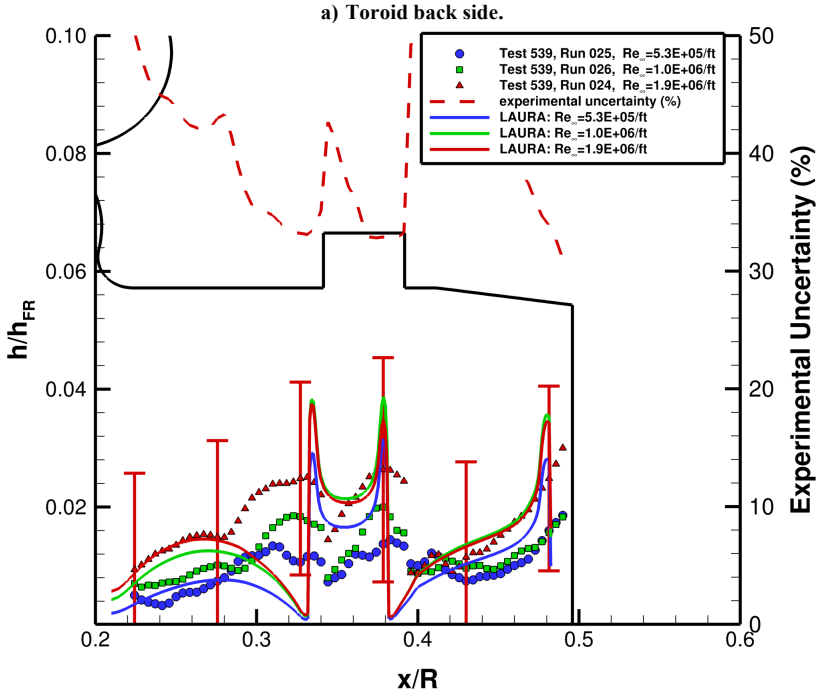


b) Payload for smooth back side.

Figure 75. Smooth model back side and payload comparisons with LAURA vs. Mach 10 data.

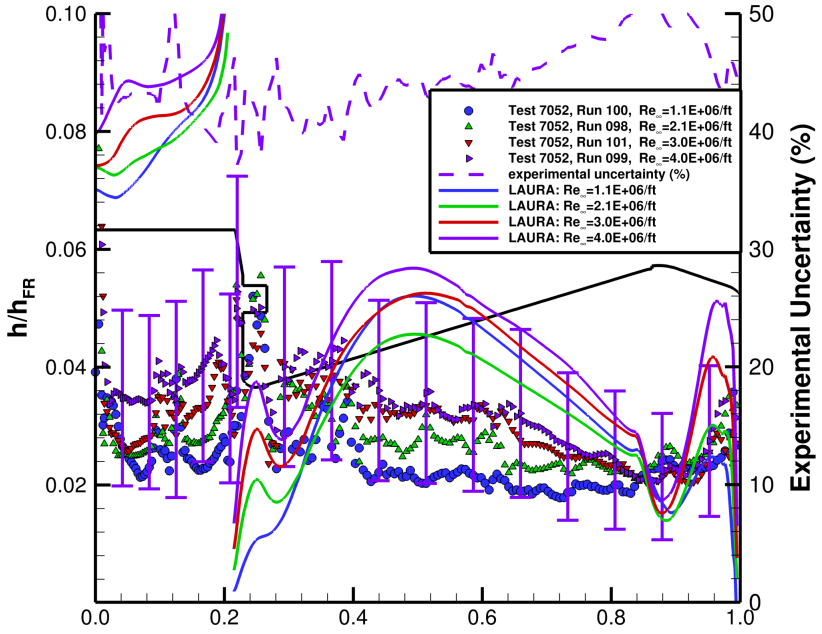


a) Toroid back side.

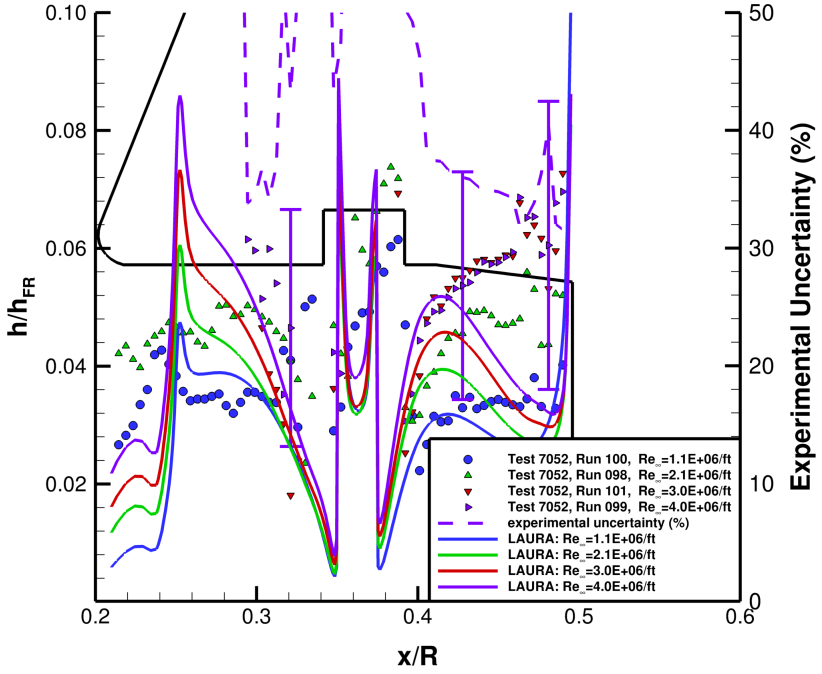


b) Payload for toroid back side.

Figure 76. Toroid model back side and payload comparisons with LAURA vs. Mach 10 data.

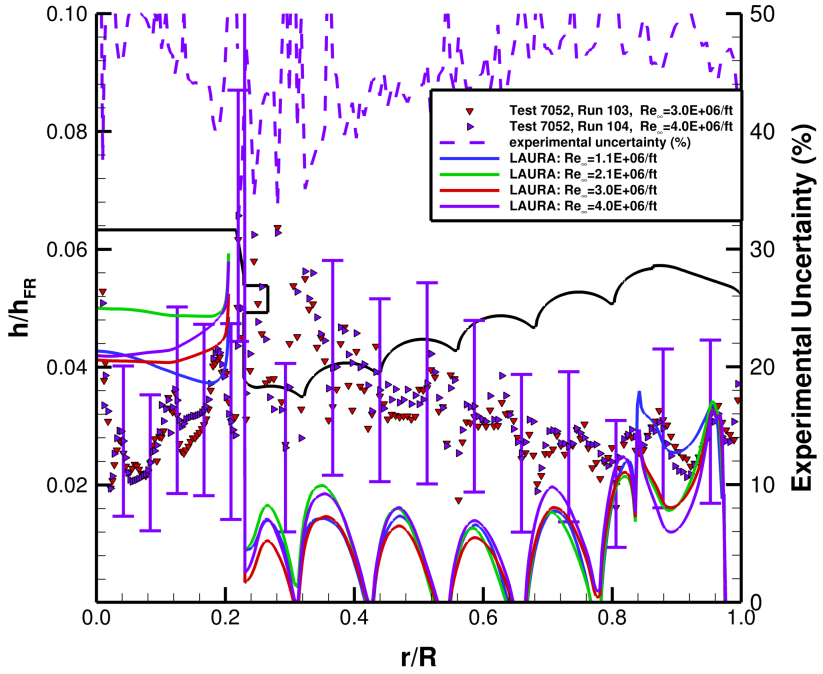


a) Smooth back side.

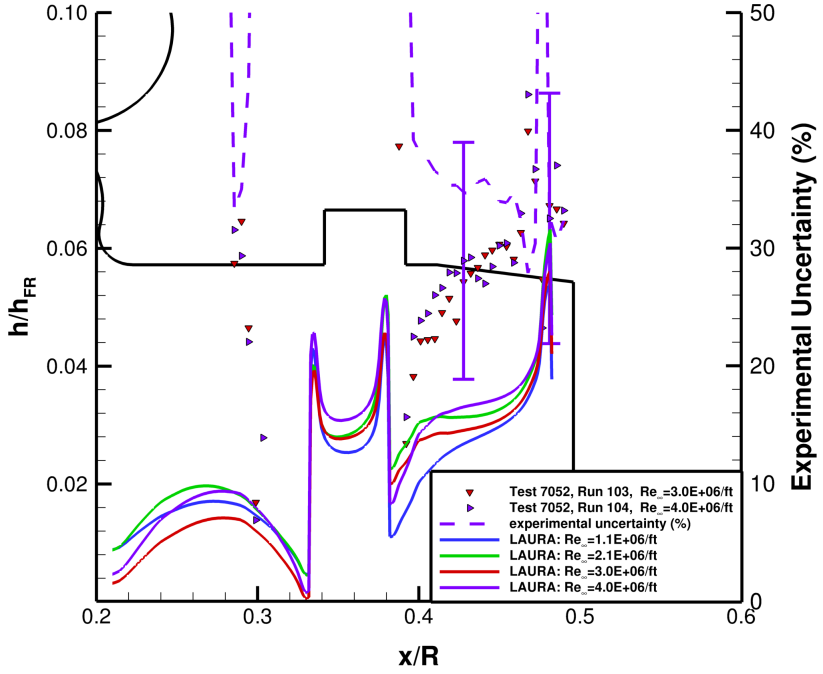


b) Payload for smooth back side.

Figure 77. Smooth model back side and payload comparisons with LAURA vs. Mach 6 data.



a) Toroid back side.



b) Payload for toroid back side.

Figure 78. Smooth model backside and payload comparisons with LAURA vs. Mach 6 data.

Appendix A. Mach 10 Phosphor Thermography Global Heating Images

Global heating images on the LOFTID models from Test 539 in the LAL 31-Inch Mach 10 Air Tunnel are presented in this Appendix. Images of the front of the aeroshell are shown in Figure 79 through Figure 84 and images of the back side of the aeroshell and on the payload are shown in Figure 85 through Figure 107 for both the smooth and toroid models. Three figures are presented on each page (when data are available) representing the three different Mach 10 Reynolds number conditions at the same angle-of-attack.

In these images, the color white represents regions where the model surface temperature exceeded the calibration range of the phosphor system (~430 K), which occurred only around the nose at the highest Reynolds number condition of 1.9×10^6/ft. The color grey represents regions on the back of the aeroshell where either A) the temperature was below the resolution of the phosphor systems and no heating was measured or B) the camera field of view was obscured (e.g. by the support blade and sting, or by the payload).

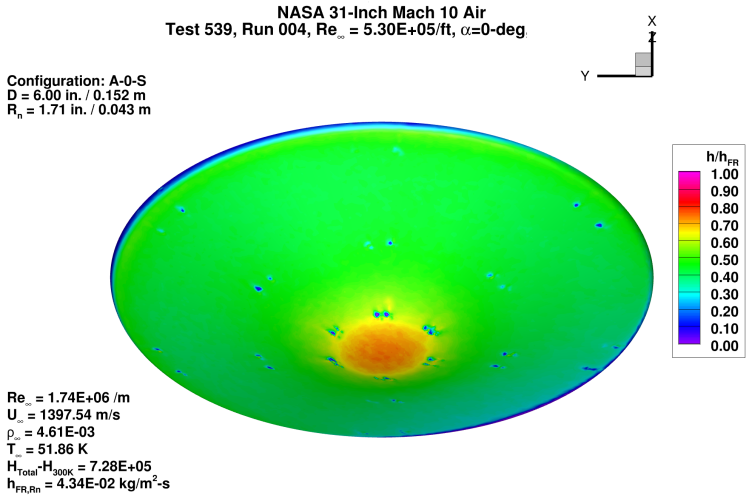


Figure 79. Test 539, Run 04, $Re_\infty = 0.5\times10^6$/ft, $\alpha = 0$ deg, $\phi = 0$ deg.

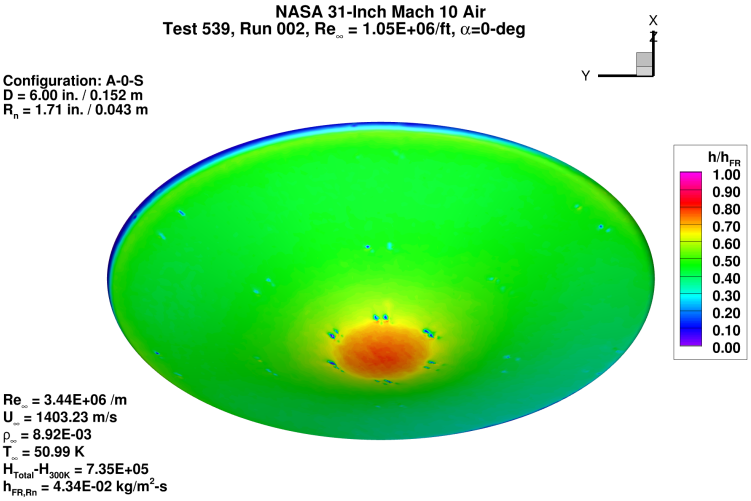


Figure 80. Test 539, Run 02, $Re_\infty = 1.0\times10^6$/ft, $\alpha = 0$ deg, $\phi = 0$ deg.

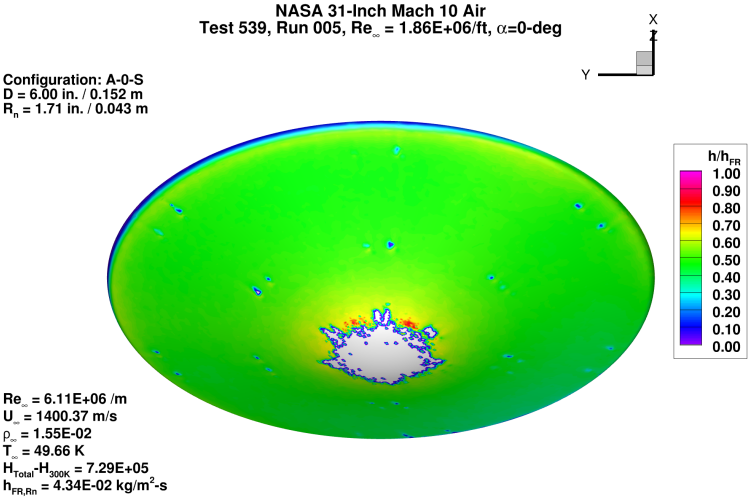


Figure 81. Test 539, Run 05, $Re_\infty = 1.9\times10^6$/ft, $\alpha = 0$ deg, $\phi = 0$ deg.

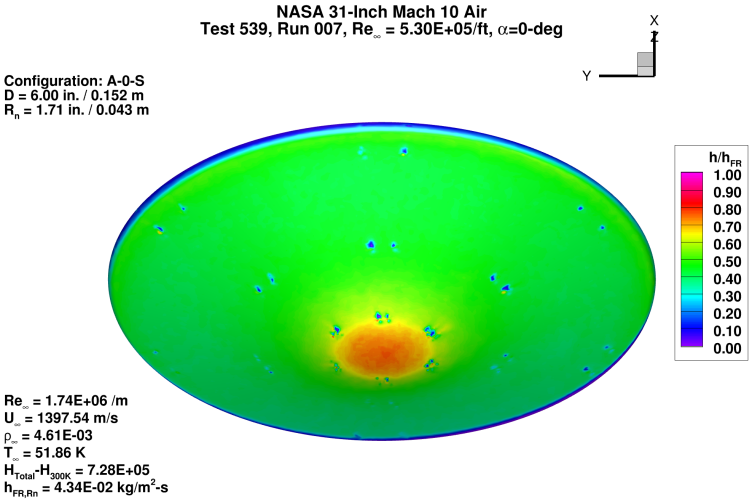


Figure 82. Test 539, Run 07, $Re_\infty = 0.5\times10^6$/ft, $\alpha = 0$ deg, $\phi = 30$ deg.

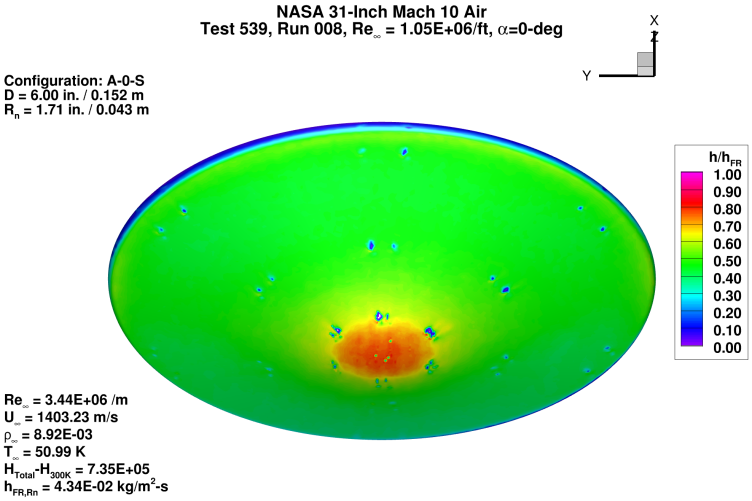


Figure 83. Test 539, Run 08, $Re_\infty = 1.0\times10^6$/ft, $\alpha = 0$ deg, $\phi = 30$ deg.

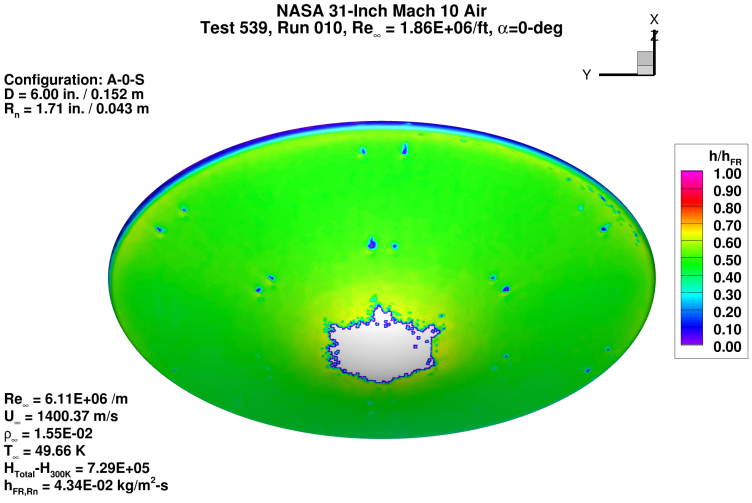


Figure 84. Test 539, Run 10, $Re_\infty = 1.9\times10^6$/ft, $\alpha = 0$ deg, $\phi = 30$ deg.

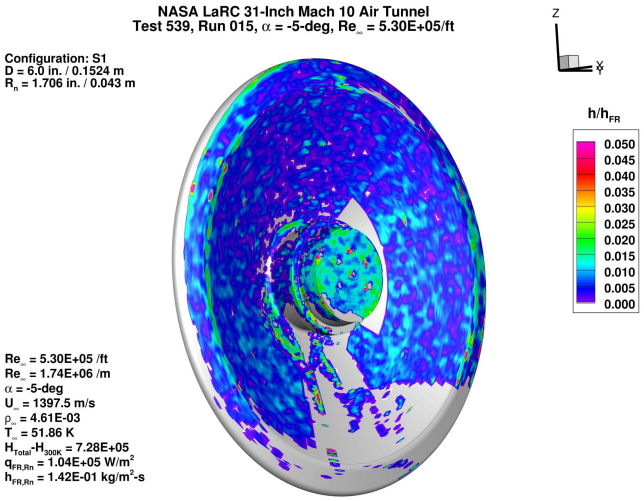


Figure 85. Test 539, Run 15, $Re_\infty = 0.5\times10^6$/ft, α = -5 deg, ϕ = 0 deg.

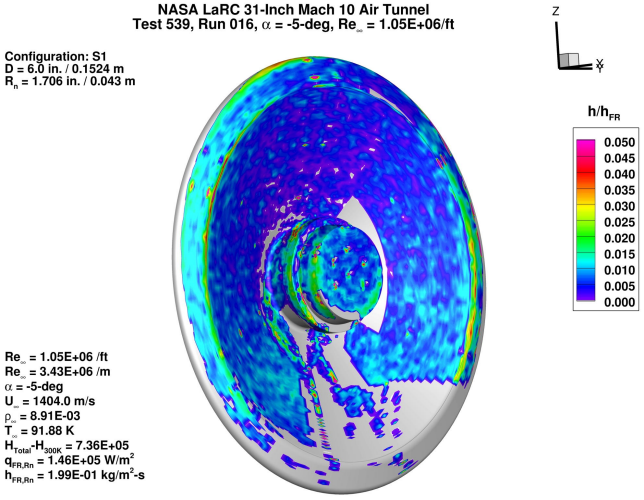


Figure 86. Test 539, Run 16, $Re_\infty = 1.0\times10^6$/ft, α = -5 deg, ϕ = 0 deg.

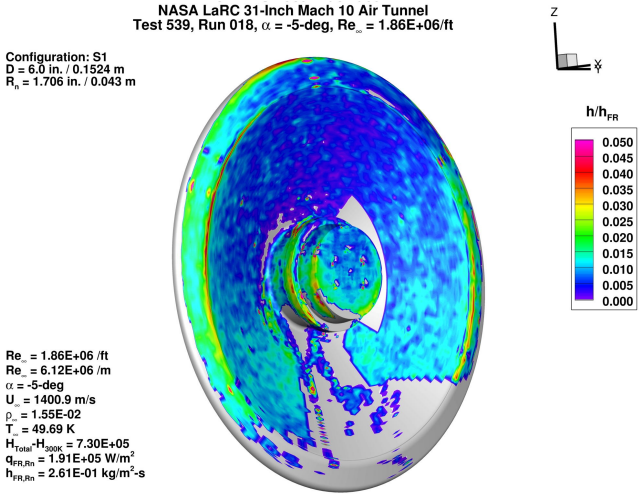


Figure 87. Test 539, Run 18, $Re_\infty = 1.9\times10^6$/ft, α = -5 deg, ϕ = 0 deg.

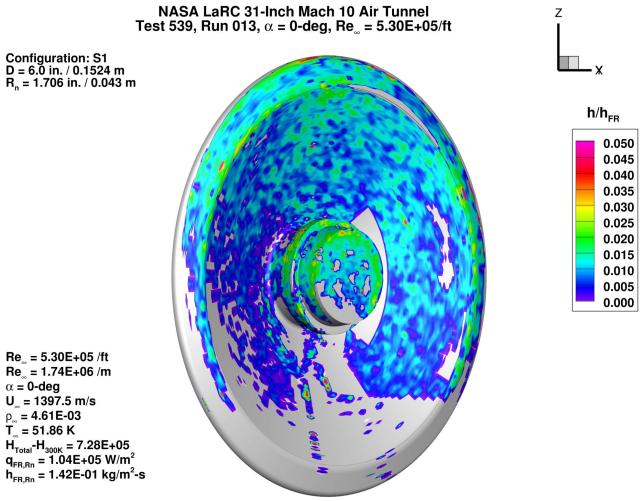


Figure 88. Test 539, Run 13, $Re_\infty = 0.5\times10^6$/ft, $\alpha = 0$ deg, $\phi = 0$ deg.

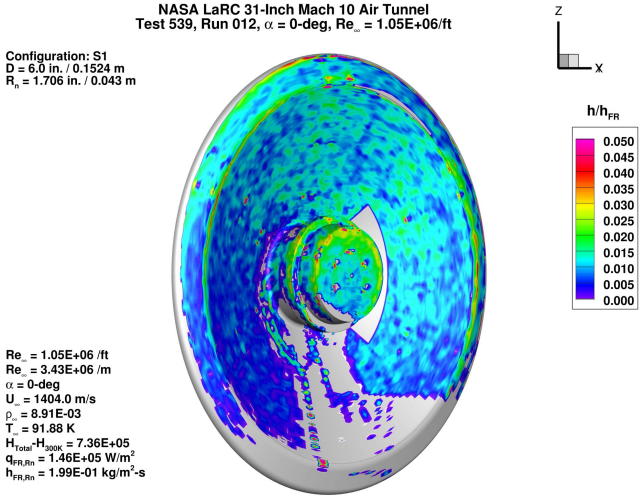


Figure 89. Test 539, Run 12, $Re_\infty = 1.0\times10^6$/ft, $\alpha = 0$ deg, $\phi = 0$ deg.

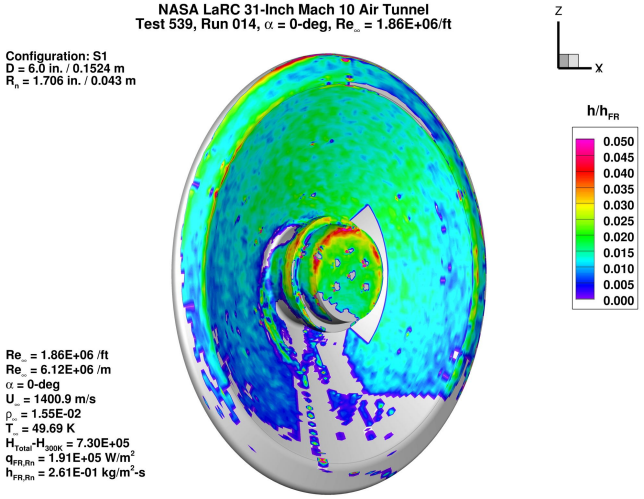


Figure 90. Test 539, Run 14, $Re_\infty = 1.9\times10^6$/ft, $\alpha = 0$ deg, $\phi = 0$ deg.

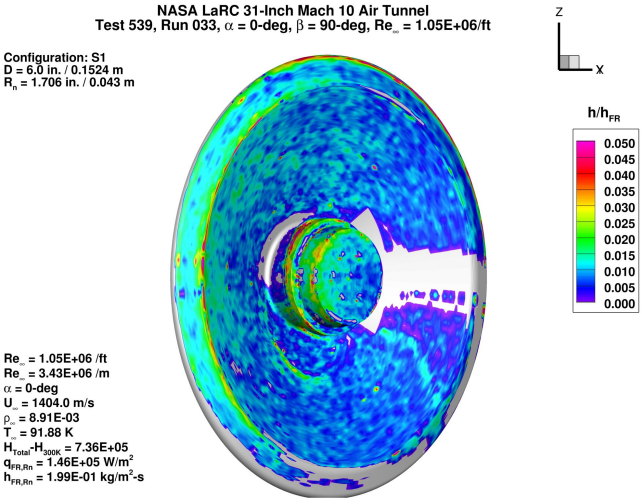


Figure 91. Test 539, Run 33, $Re_\infty = 1.0\times10^6$/ft, $\alpha = 0$ deg, $\phi = 90$ deg.

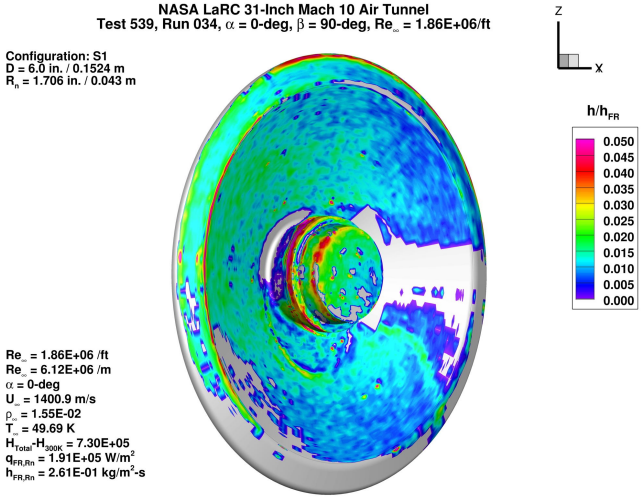


Figure 92. Test 539, Run 34, $Re_\infty = 1.9\times10^6$/ft, $\alpha = 0$ deg, $\phi = 90$ deg.

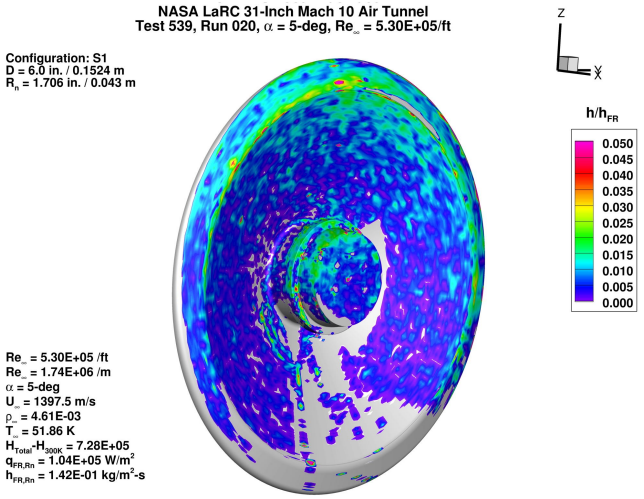


Figure 93. Test 539, Run 20, $Re_\infty = 0.5\times10^6$/ft, α = +5 deg, ϕ = 0 deg.

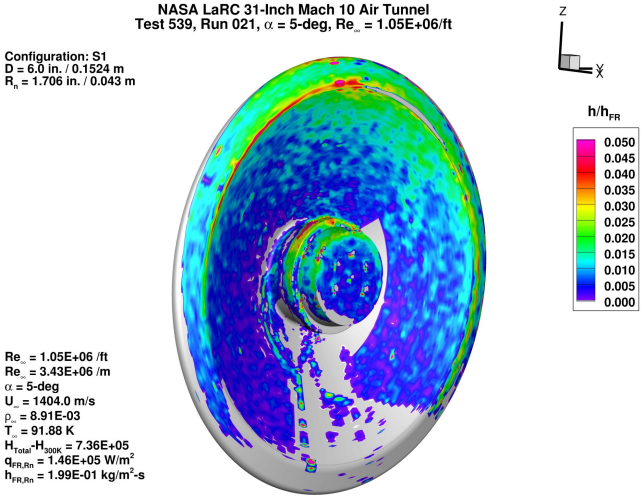


Figure 94. Test 539, Run 21, $Re_\infty = 1.0\times10^6$/ft, α = +5 deg, ϕ = 0 deg.

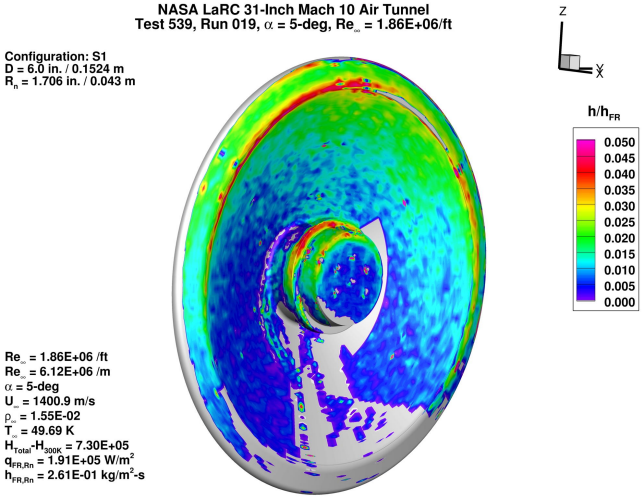


Figure 95. Test 539, Run 19, $Re_\infty = 1.9\times10^6$/ft, α = +5 deg, ϕ = 0 deg.

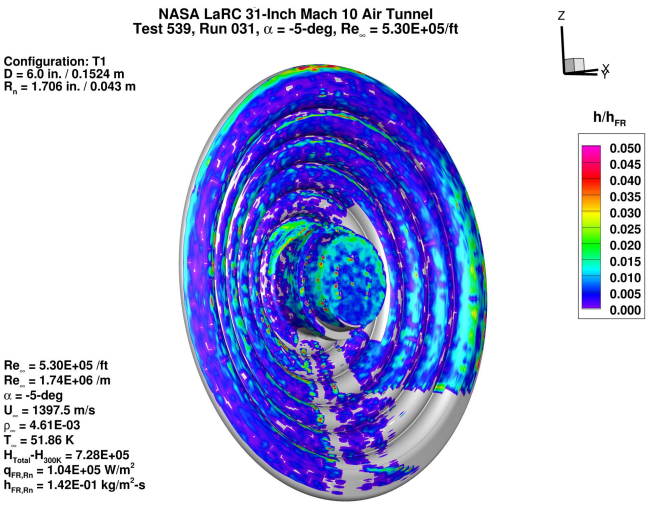


Figure 96. Test 539, Run 31, $Re_\infty = 0.5\times10^6$/ft, α = -5 deg, ϕ = 0 deg.

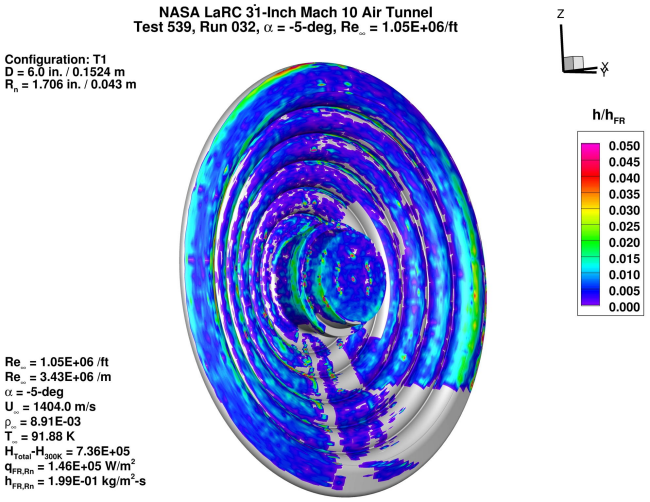


Figure 97. Test 539, Run 32, $Re_\infty = 1.0\times10^6$/ft, α = -5 deg, ϕ = 0 deg.

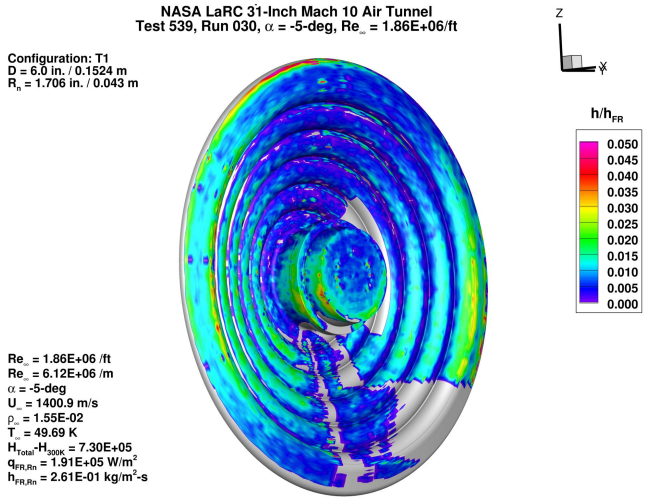


Figure 98. Test 539, Run 30, $Re_\infty = 1.9\times10^6$/ft, α = -5 deg, ϕ = 0 deg.

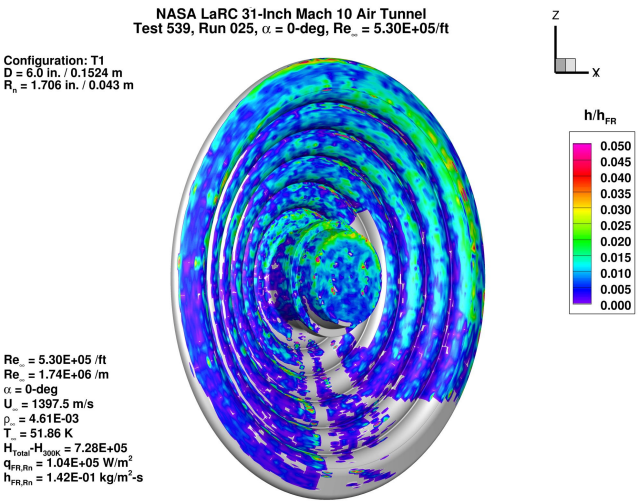


Figure 99. Test 539, Run 25, $Re_\infty = 0.5\times10^6$/ft, $\alpha = 0$ deg, $\phi = 0$ deg.

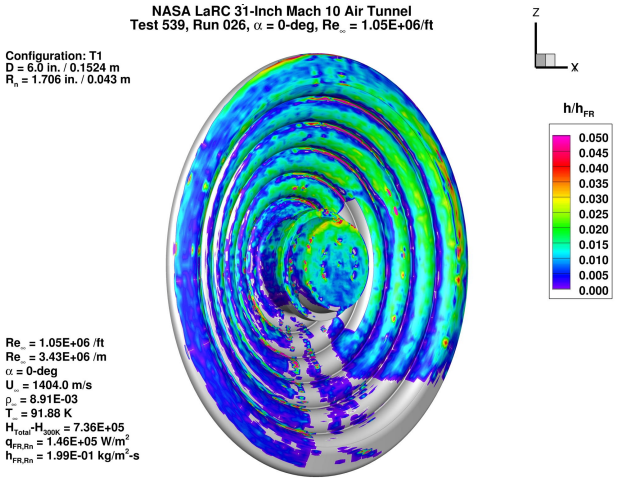


Figure 100. Test 539, Run 26, $Re_\infty = 1.0\times10^6$/ft, $\alpha = 0$ deg, $\phi = 0$ deg.

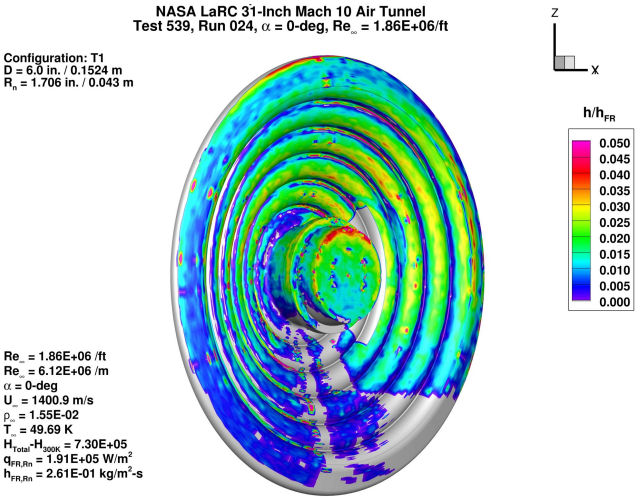


Figure 101. Test 539, Run 24, $Re_\infty = 1.9\times10^6$/ft, $\alpha = 0$ deg, $\phi = 0$ deg.

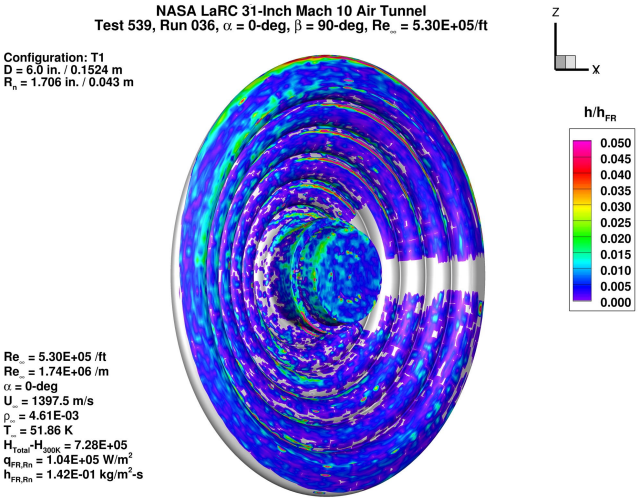


Figure 102. Test 539, Run 36, $Re_\infty = 0.5\times10^6$/ft, $\alpha = 0$ deg, $\phi = 90$ deg.

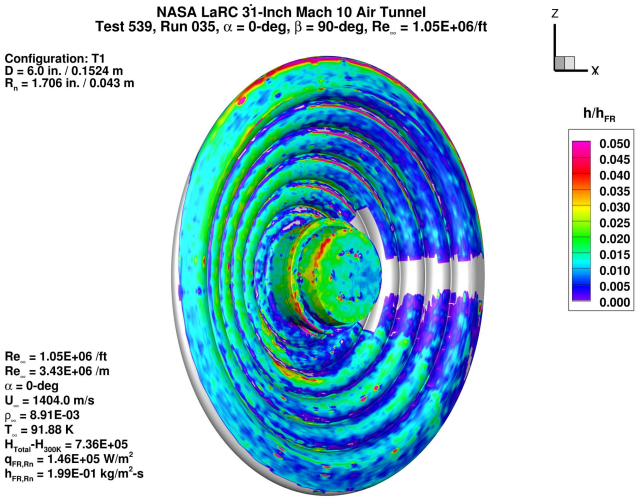


Figure 103. Test 539, Run 35, $Re_\infty = 1.0\times10^6$/ft, $\alpha = 0$ deg, $\phi = 90$ deg.

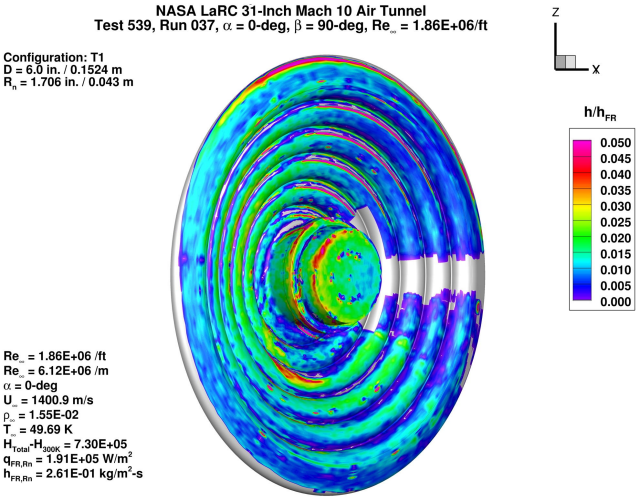


Figure 104. Test 539, Run 37, $Re_\infty = 1.9\times10^6$/ft, $\alpha = 0$ deg, $\phi = 90$ deg.

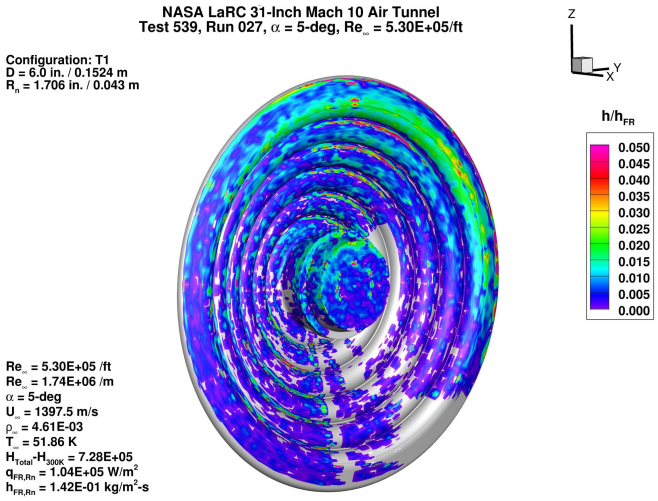


Figure 105. Test 539, Run 27, $Re_\infty = 0.5\times10^6$/ft, $\alpha = +5$ deg, $\phi = 0$ deg.

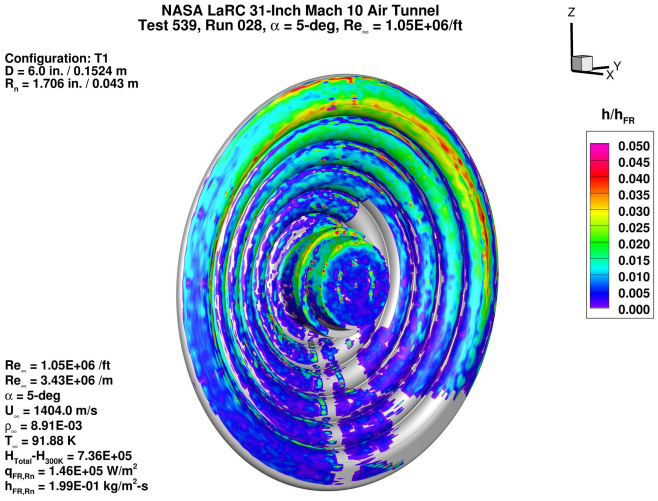


Figure 106. Test 539, Run 28, $Re_\infty = 1.0\times10^6$/ft, $\alpha = +5$ deg, $\phi = 0$ deg.

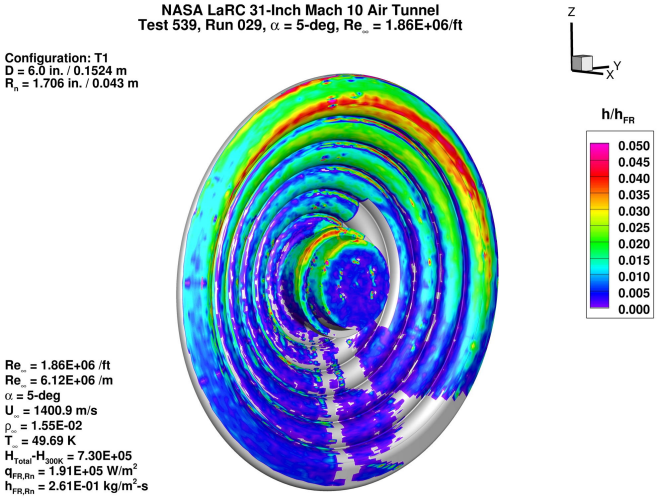


Figure 107. Test 539, Run 29, $Re_\infty = 1.9\times10^6$/ft, $\alpha = +5$ deg, $\phi = 0$ deg.

Appendix B. Mach 6 Phosphor Thermography Global Heating Images

Global heating images on the LOFTID models from Test 7052 in the LAL 20-Inch Mach 6 Air Tunnel are presented in this Appendix. Images of the front of the aeroshell are shown in Figure 108 through Figure 110 and images of the back side of the aeroshell and on the payload are shown in Figure 111 through Figure 118 for both the smooth and toroid models.

In these images, the color grey represents regions on the back of the aeroshell where either A) the temperature was below the resolution of the phosphor systems and no heating was measured or B) the camera field of view was obscured (e.g. by the support blade and sting, or by the payload). Also, for the back view cases, small portions of the top-front (from the camera point-of-view) of the aeroshell were visible, but no attempt was made to properly illuminate this shoulder region, so these data were excluded from presentation

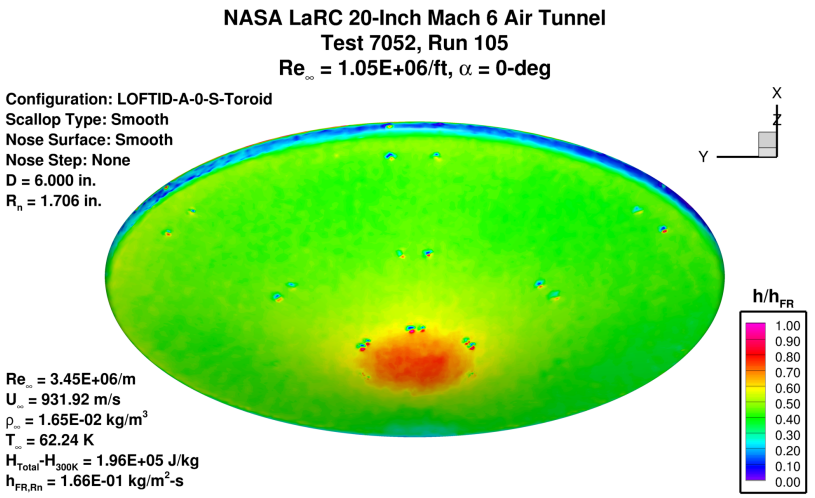


Figure 108. Test 7052, Run 105, $Re_\infty = 1.1\times10^6$/ft, $\alpha = 0$ deg, $\phi = 0$ deg.

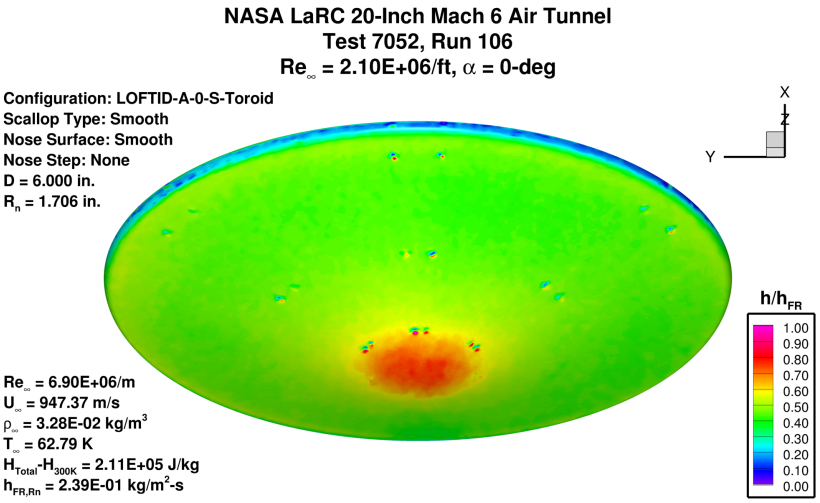


Figure 109. Test 7052, Run 106, $Re_\infty = 2.1\times10^6$/ft, $\alpha = 0$ deg, $\phi = 0$ deg.

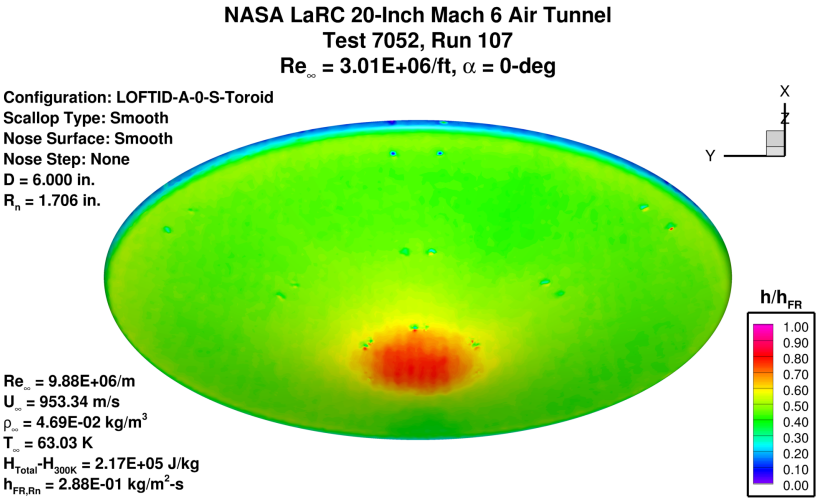


Figure 110. Test 7052, Run 107, $Re_\infty = 3.0\times10^6$/ft, $\alpha = 0$ deg, $\phi = 0$ deg.

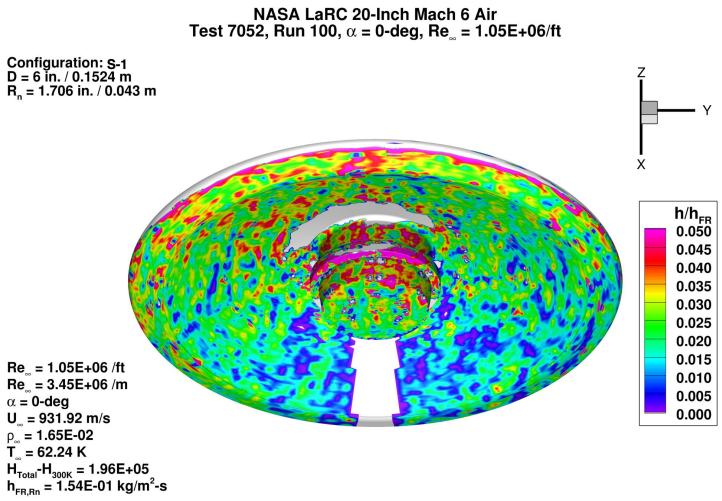


Figure 111. Test 7052, Run 100, $Re_\infty = 1.1\times10^6$/ft, $\alpha = 0$ deg, $\phi = 0$ deg.

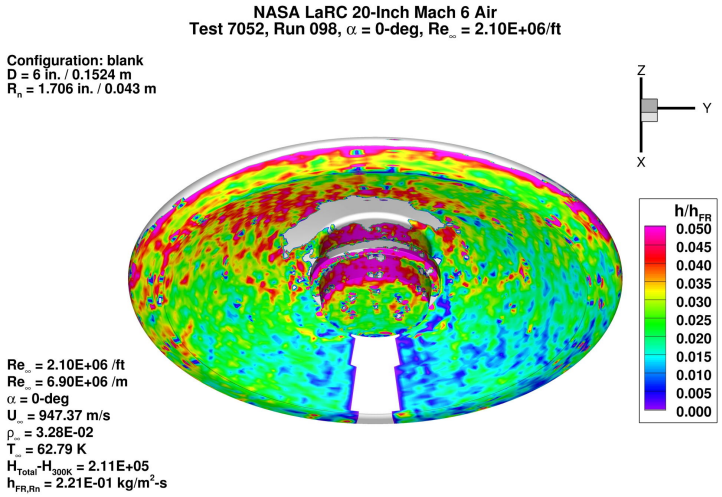


Figure 112. Test 7052, Run 98, $Re_\infty = 2.0\times10^6$/ft, $\alpha = 0$ deg, $\phi = 0$ deg.

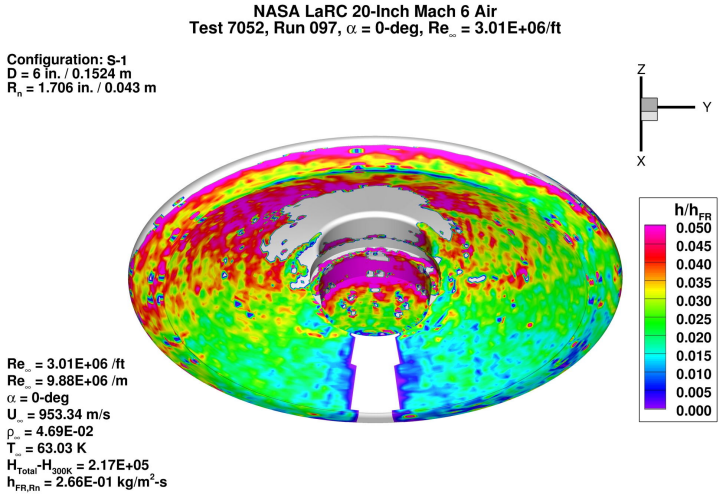


Figure 113. Test 7052, Run 97, $Re_\infty = 3.0\times10^6$/ft, $\alpha = 0$ deg, $\phi = 0$ deg.

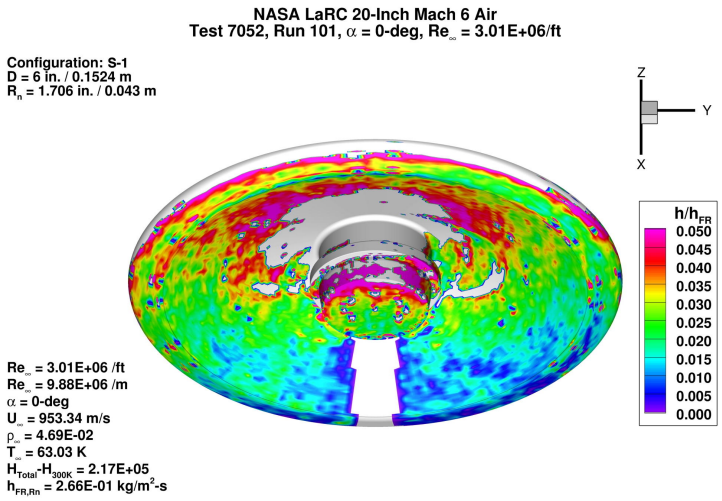


Figure 114. Test 7052, Run 101, $Re_\infty = 3.0\times10^6$/ft, $\alpha = 0$ deg, $\phi = 0$ deg.

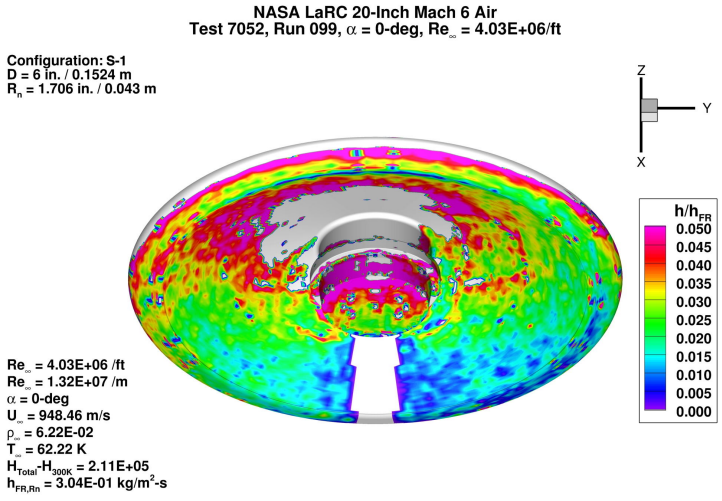


Figure 115. Test 7052, Run 99, $Re_\infty = 4.0\times10^6$/ft, $\alpha = 0$ deg, $\phi = 0$ deg.

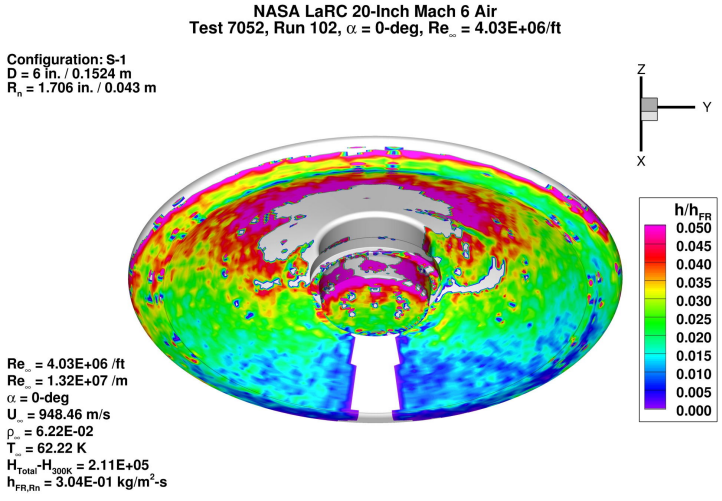


Figure 116. Test 7052, Run 102, $Re_\infty = 4.0\times10^6$/ft, $\alpha = 0$ deg, $\phi = 0$ deg.

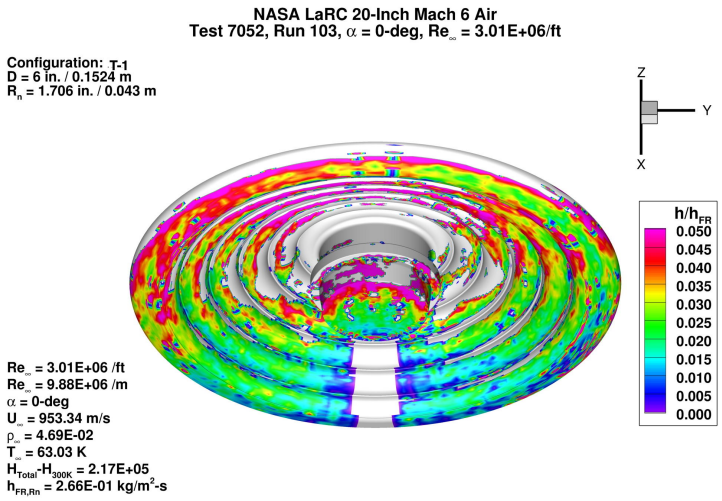


Figure 117. Test 7052, Run 103, $Re_\infty = 3.0\times10^6$/ft, $\alpha = 0$ deg, $\phi = 0$ deg.

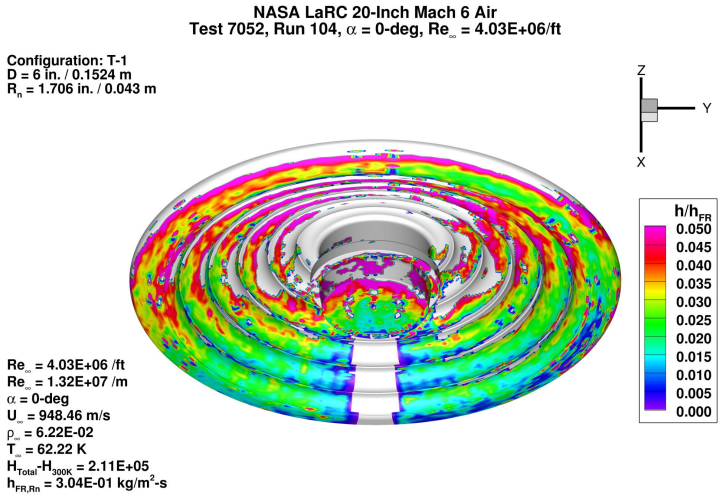


Figure 118. Test 7052, Run 104, $Re_\infty = 4.0\times10^6$/ft, $\alpha = 0$ deg, $\phi = 0$ deg.